IMAGING CASCADIA SLOW SLIP EVENTS WITH MODERN INTERFEROMETRIC SYNTHETIC APERTURE RADAR DATASETS

A DISSERTATION
SUBMITTED TO THE DEPARTMENT OF GEOPHYSICS
AND THE COMMITTEE ON GRADUATE STUDIES
OF STANFORD UNIVERSITY
IN PARTIAL FULFILLMENT OF THE REQUIREMENTS
FOR THE DEGREE OF
DOCTOR OF PHILOSOPHY

Yujie Zheng

October 2019

Abstract

The Cascadia subduction zone, famous for its potential to generate very large earthquakes, is one of the regions where slow slip events (SSEs) were first detected. While conventional earthquakes result from fast slip on the faults and take place in a few seconds or minutes, SSEs rupture much more slowly and can take place over weeks or even months. While these seismically silent events themselves are not dangerous, they can significantly alter their surrounding stress field, which in turn, influences the local seismic hazard potential. Although the discovery of SSEs is largely attributed to continuous Global Navigation Satellite System (GNSS) networks, GPS observations alone often lack the spatial resolution needed to model slow slip at depth. Interferometric synthetic aperture radar (InSAR), on the other hand, is an established geodetic technique that can provide dense surface measurements over large areas. However, the application of InSAR techniques to the study of SSEs is severely limited due to low signal to noise ratios (SNR). Since Cascadia has a vast forest cover due to abundant rainfall and mild climate, interferograms formed in this region also have large decorrelated areas. Furthermore, where measurement is possible, the relative small slow slip signal of < 1 cm is overprinted by noises such as atmospheric phase delay which can reach 2 cm standard deviation at large spatial scales, satellite orbit errors, and residual topographic correction errors. Therefore, it is nearly impossible to determine slow slip signals using only a few interferograms.

We present here the use of InSAR time-series techniques to measure deformation

associated with both slow slip events and inter-SSE velocity in the Cascadia region. Specifically, we address the statistical properties of different interferometric phase components in interferogram stacks and develop time-series approaches that take full advantage of the dense temporal sampling of modern InSAR datasets. We created more than 4500 interferograms with 303 scenes acquired across 96 different dates over the majority of Cascadia region using both Sentinel-1A and 1B data from June 2015 to May 2018. We focus on the 2015-2016 winter Central Cascadia slow slip event and produce two maps: one displays the average annual line-of-sight (LOS) velocity of the region during the three year observation window, and the other shows the LOS magnitude of the SSE surface deformation. The inter-SSE velocity map shows a 8 mm/year difference across the image. The observed inter-SSE velocity does not only reflect tectonic motion, but also any long-term deformation that took place during the observed time period. The observed SSE LOS deformation mostly reflect vertical movements of the surface resulting from the slow slip at depth. The range of SSE LOS deformation is around 1 cm across the studied area. Due to InSAR 's insensitivity to north-south motion, combined with large uncertainties of GPS vertical measurements, comparisons between GPS measurements and InSAR measurements are not particularly informative. Nonetheless, projected LOS GPS measurements also shows 1 cm range of SSE deformation with a similar uplift to subsidence deformation pattern. Direct comparisons between GPS and InSAR measurements show that they agree within their respective 1-σ uncertainty bounds – for InSAR measurements, these error bounds range from 2 mm to 10 mm. Slip distributions obtained from InSAR measurements show a comparable moment magnitude (Mw 6.6) to slip distributions obtained from GPS horizontal data (also Mw 6.6). However, slip distributions obtained from InSAR measurements are concentrated in an area one third the size of those in GPS solutions with a peak slip magnitude three times the peak slip from GPS measurements.

We have also developed software to form and analyze interferograms efficiently. With the anticipation of an ever-growing SAR archive, our effort in producing standardized and user-friendly InSAR products will help maximize InSAR's potential in helping the scientific community better understand our dynamic planet.

Acknowledgments

I immensely enjoyed my time in Stanford pursing my doctoral degree in Geophysics. First of all, I wish to thank my advisor, Prof. Howard Zebker, for his guidance, encouragement, advise and help during the past five years as I worked on the research described in this thesis. I learnt from Howard how to think scientifically, how to face setbacks, how to break down complex problems into small, manageable parts, and how to effectively write scientific articles. I also wish to thank Prof. Paul Segall for his insights in slow slip events modeling and he is also my second project advisor. I also thank the other members of my reading and oral thesis defense committees, Prof. Eric Dunham, Prof. Dusty Schroeder and Prof. Alex Konings, for providing constructive criticisms on this work.

Over the years I have benefited greatly from my interactions with past and current members of the radar remote sensing group including Lin Liu, Albert Chen, Jingyi Chen, Eileen Lin, Roger Michaelides, Stacy Huang, Emma Velterop.

I am grateful for amazing friendship and support from my wonderful friends in Stanford including Heath Rojas, Ying-Qi Wong, Ben Mullet, Alex Kendrick, Stephan Eismann, Tao Jia, Haoli Guo, Kai Zhang, David Nissimoff, Gongxun Liu and many others, who have made my time in Stanford deeply memorable and meaningful.

This work is supported by NASA Earth Science and Interior Grant NNX 17AE036.

Finally I thank my parents for their unwavering support and encouragement.

Contents

List of Tables

List of Figures

Chapter 1

Introduction

1.1 Problem Definition: Slow Slip Events in Cascadia

Earth's tectonic plates are in constant motion. The relative movements between adjacent plates build up stress in the Earth's crust and cause earthquakes. While conventional earthquakes exhibit fast slip on the faults and take place in a few seconds or minutes, slow slip events (SSEs) rupture much more slowly and can take place over days or even weeks. While these silent events themselves are not dangerous, they can significantly alter the surrounding stress field, which in turn, influences the local seismic hazard potential.

The Pacific Northwest (Fig. 1.1), home to populous cities such as Seattle and Vancouver, sits on top of the Cascadia subduction zone, which is one of the regions where deep-seated subduction zone SSEs were first detected (See Fig. 2.3). *Dragert et al.* (2001) reported that a cluster of seven GPS sites reversed their landward motion for a period of about 2 weeks in the fall of 1999 and explained this unexpected

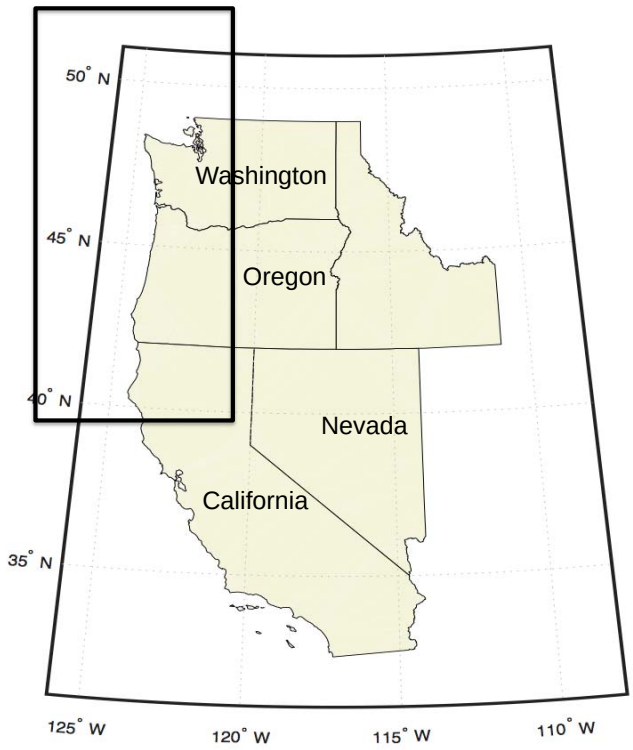

Figure 1.1: Map of the Cascadia subduction zone (black box). The Pacific Northwest area often refers to the region bounded by the Pacific Ocean to the west and by the Rocky Mountains to the east, primarily includes British Columbia, the states of Washington, Oregon and Northern California.

phenomenon later by an aseismic slip of $\sim$ 2 cm below the seismogenic zone. Further studies of the GPS network revealed that SSEs take place regularly in the Cascadia region with an average recurrence period of about 14 months in Washington, 24 months in Oregon and 10 months in Northern California (*Miller et al.*, 2002; *Dragert et al.*, 2004). Each SSE lasts for about 2-4 weeks, releasing strains equivalent to Mw 6.5-6.8 earthquakes (*Dragert et al.*, 2004). Given that the Cascadia subduction zone is capable of producing very big earthquakes – the last of which was a Mw 9.0 earthquake in 1700 – it is in the interests of the general public to understand the roles of SSEs in the earthquake cycle. To wit, are SSEs postponing or advancing the inevitable occurrence of the really big one? Will SSEs trigger big earthquakes?(e.g. *Kato et al.*, 2012; *Segall and Bradley*, 2012)

Although the discovery of SSEs is largely due to continuous GNSS networks, GPS observations alone lack the spatial resolution needed to model slow slip at depth. The large uncertainties in GPS vertical observations also mean that the use of GPS data for slow slip modeling is limited. Interferometric synthetic aperture radar (InSAR), on the other hand, is an established technique that can provide dense surface measurements sensitive mostly to vertical displacements in large areas. In addition, with the recent fleet of SAR satellites including Sentinel-1, ALOS-2, COSMO-SkyMed, and RADARSAT-2 (Fig.1.2), the temporal resolution of InSAR measurements has been significantly improved. However, the application of InSAR techniques to the study of SSEs is severely limited due to low signal to noise ratios (SNR). Nonetheless, several studies have demonstrated the capability of InSAR to monitor SSEs. For example, *Chen et al.* (2014) proposed a small baseline subset (SBAS) algorithm to extract both secular motion and transient ground deformation from noisy InSAR measurements and successfully identified the 2010 slow slip event in the south flank of the Kilauea volcano, Hawaii. *Bekaert et al.* (2016) combined geodetic observations from GNSS

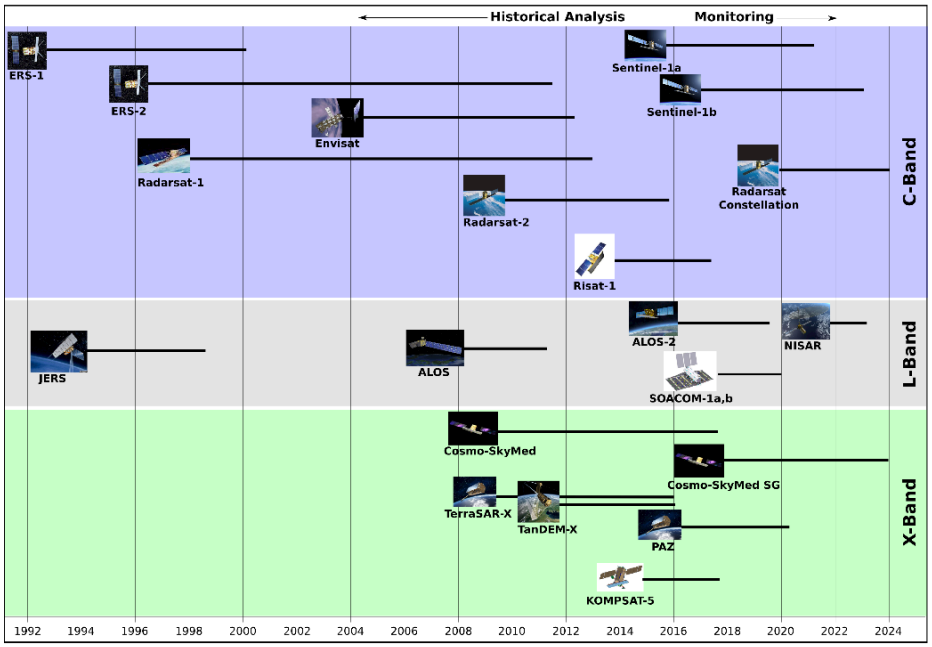

Figure 1.2: Historic and active Synthetic Aperture Radar satellites. Image from `https://www.unavco.org/instrumentation/geophysical/imaging/sar-satellites`

and InSAR to model the 2006 Guerrero SSE using a Network Inversion Filter (*Segall and Matthews*, 1997; *Miyazaki et al.*, 2006) and demonstrated that the use of InSAR data provided better constraints than using GPS data only.

However, InSAR applications in the Cascadia region have been limited because of poor measurement quality over this region. Combined with small surface displacements associated with Cascadia SSEs (< 1 cm), it is not possible to identify a SSE using a small number of interferograms. A large set of high-quality interferometric measurements is needed to enhance signal-to-noise ratio to make SSE detection by InSAR possible.

1.2 Approach: The Use of Modern SAR Datasets

Synthetic Aperture Radar (SAR) is a two dimensional radar imaging technique that produces coherent images of Earth's surface with meter level resolution over large spatial scales. Interferometric SAR takes advantage of the coherent nature of complex SAR images to measure topography, motion, or scattering property changes of the surface of the Earth.

In the past few years, three new InSAR satellites, Sentinel 1A/B and ALOS-2, became operational. This new generation of satellites provides the temporal sampling rate and spatial coverage needed to revolutionize InSAR's ability to reduce noise and capture small crustal deformation signals over large spatial areas. Fig. 1.2 shows the lifespan of recent SAR missions. It is obvious that with current and anticipated new SAR satellites becoming operational in the near future, we have access to a large set of modern high-quality SAR observations covering the entire globe every few days. In this work, we focus on the Sentinel-1 satellites.

Sentinel-1 is a constellation of two polar orbiting SAR satellites, operated by the European Space Agency, and provides day and night synthetic aperture radar images free of charge to users all over the world. Both satellites (1-A and 1-B) operate in the C-band (wavelength is 6 cm) and have an orbit repeat cycle of 12 days. Sentinel-1A was launched in April 2014 and Sentinel-1B was launched in June 2016. The short orbit repeat time combined with small orbital tube, i.e., small spatial baselines (within 150 meters), makes Sentinel-1 an ideal candidate for observing small amplitude signals in noisy environments.

Another important fact about Sentinel-1 is that it operates using the Terrain

Observation with Progressive Scans SAR (TOPSAR) imaging mode. TOPSAR acquisition provides large swath width, which results in short orbit repeat time. Fig. 1.3 compares Sentinel-1A coverage of the Pacific Northwest with that of the Japanese satellite ALOS-1. ALOS-1 operates with the more conventional stripmap imaging mode and has a swath width of 70 km (shown in blue). In contrast, Sentinel-1 has a swath with of 250 km (shown in gray). The black dots are recorded tremor locations of the 2016 February SSE in Oregon (tremors are seismic signals that are related to SSEs). As can be seen, to cover the spatial scale of one SSE, we need the large spatial coverage Sentinel-1 provides.

1.3 Contributions

There are two main focuses of this thesis. First, we focus on developing tools that help us best exploit modern InSAR datasets and push its limits in observing very small signals in very noisy environments. Second, we apply these processing and analyzing tools to study slow slip events in Central Cascadia, an area that is traditionally difficult for InSAR observations. We extract deformation signals associated with the 2015-2016 winter Central Cascadia slow slip event and use these measurements to learn about slip distributions at depth, in order to answer more fundamental questions about the underlying physical processes of the Cascadia subduction zone. Specifically, we have made the following contributions:

1. We have developed an efficient and user-friendly InSAR processing algorithm whereby we geocode and compensate for topography-related phases in Single-Look Complex SAR scenes. We subsequently developed software packages adopting this algorithm for ALOS-1 and COSMO-SkyMed satellites data processing.

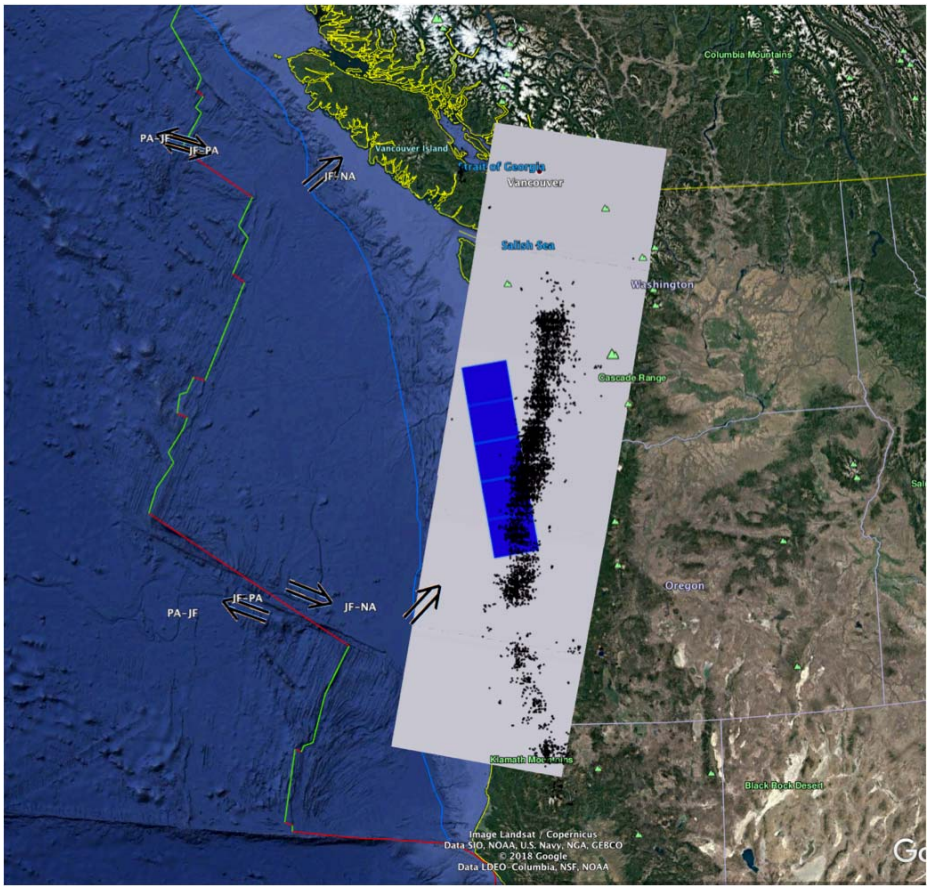

Figure 1.3: Comparison between Sentinel-1 swath width (gray rectangle), ALOS-1 swath width (blue rectangle) and the spatial coverage of tremors related to the 2015-2016 winter Central Cascadia slow slip event (black dots). It is clear that Sentinel-1 enjoys much greater spatial coverage and hence is more applicable to large spatial scale studies.

2. We have developed a Sentinel-1 software package adopting a variation of the Geocoded and Topography Corrected SAR algorithm. We geocode and topography correct Sentinel-1 scenes while co-registering all scenes to the same geographic area of interest. This workflow enables us to combine different SAR acquisitions with ease and without generating large number of intermediate files.

3. We have developed and validated a covariance model for decorrelation phase noise. Our model shows that incorporating redundant interferograms into time-series analysis can significantly reduce decorrelation noise for low correlation areas.

4. We have developed an algorithm to estimate the atmospheric noise covariance matrix from the interferogram stack. Using this algorithm, we can keep track of atmospheric noise propagation through the stack.

5. We have applied two different stacking strategies to interferograms formed over Central Cascadia, which are optimized for noise reduction, and produced the deformation map for the 2015-2016 winter Oregon slow slip event as well as the inter-SSE velocity map of the same area.

6. We have developed 2D and 3D slip models of the slow slip event and demonstrated that InSAR data provides more accurate estimates of the uppermost and lowermost points of the slip zone.

1.4 Thesis Roadmap

The remainder of this thesis is organized as follows:

We begin in Chapter 2 and Chapter 3 by introducing the basics about Cascadia SSEs and InSAR.

In Chapter 4 we present the concept of topography-corrected and geocoded SAR and demonstrate how it can be implemented in the frame of motion-compensation techniques, and in Sentinel-1 SAR products. This chapter is based on materials published in *IEEE Journal of Selected Topics in Applied Earth Observations and Remote Sensing* in 2017 (*Zheng and Zebker*, 2017).

In Chapter 5 we discuss noise reduction in interferogram stacks. Specifically, we present covariance matrices for atmospheric noise and decorrelation noise, and discuss how errors propagate in stacks and how to optimize noise reduction by choosing the best stacking strategy. This chapter is mostly based on materials currently under review in *Journal of Geophysical Research*.

In Chapter 6 we illustrate how we can extract slow slip deformation signals from large Sentinel-1 datasets by stacking. We also present 1-sigma uncertainty of the retrieved slow slip deformation and compare our results with GPS measurements.

In Chapter 7 we present 2D and 3D models of the 2015-2016 winter Central Cascadia slow slip event and show that by including InSAR data, we can better resolve slow slip at depth, especially the up-dip and down-dip limit of the SSE zone on the plate boundary. This chapter and Chapter 6 will be submitted to the *Journal of*

Geophysical Research.

Finally we provide some concluding remarks and discussions in Chapter 8.

Chapter 2

Cascadia Slow Slip Events: Background

2.1 Geologic Setting

Cascadia refers to the region where the relatively young oceanic Juan de Fuca, Gorda, and Explorer plates descend at a speed of approximately 4cm/year with respect to the stable Continental North American plate (Fig. 2.1). Geographically, Cascadia stretches about 700 miles from British Columbia to Northern California, and is bounded by the Pacific Ocean to the west and the Rocky Mountains on the east.

Tectonic loading of the locked seismogenic zone resulting from continuous motion of the converging plates can give rise to great earthquakes. Although the Cascadia subduction zone (CSZ) has not produced any big earthquakes in modern times, various studies have established that great earthquakes (M9.0 or greater) have regularly occurred in this region in the past, with a repeat interval of 400 to 600 years (*Atwater and Hemphill-Haley*, 1997; *Atwater*, 1987; *Clague*, 1997). The last known such megathrust earthquake took place in January, 1700. The estimated magnitude

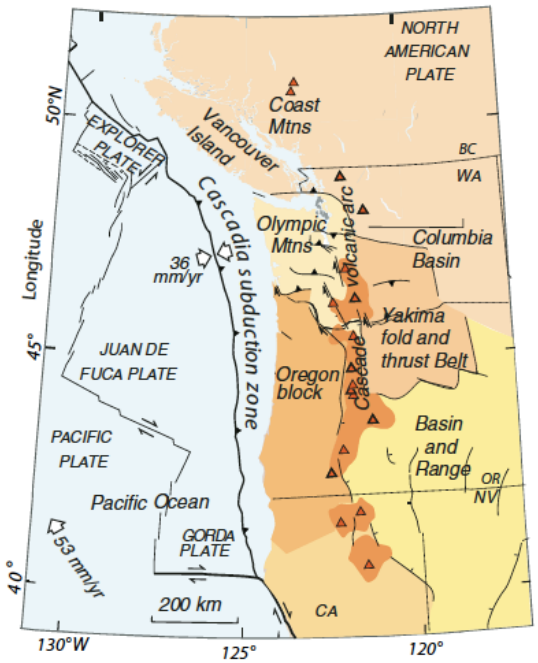

Figure 2.1: Schematic tectonic map of Cascadia. From *Gomberg et al.* (2010)

9 earthquake created a tsunami that rampaged across the Pacific and caused damage in coastal villages in Japan (*Satake et al.*, 1996). There is no doubt that the CSZ presents great seismic hazard. Understanding of the seismic mechanisms of the subduction zone, therefore, is critical for potential hazard analysis and preparation.

Fig. 2.2 illustrates a simple dislocation model for a subduction zone. As the denser oceanic plate subducts under the light overriding continental plate, a shallow portion of the fault is locked, and only at a deeper depth does the fault slide at the full plate convergence rate, V_{pl}. As a result, the accumulating elastic strain energy in the locked portion of the fault is released periodically in future earthquakes. Apart from the locked and creeping zones, a transitional zone is often adopted in models to make a smoother transition of slip velocity from zero to V_{pl} between the locked and the creeping portions of the fault. Slow slip events, which are the focus of this thesis,

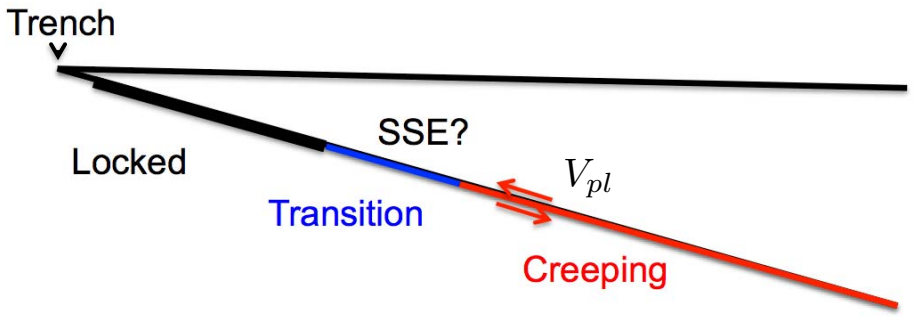

Figure 2.2: Illustration for a simple elastic dislocation model for subduction zone deformation.

are believed to mostly occur in the transitional zone of the fault.

Knowledge of the down-dip limit of the locking zone is critical for seismic hazard estimation because a deeper rupture implies greater seismic hazard for major populous cities such as Seattle and Portland. However, since no significant earthquakes have taken place in Cascadia in the past 300 years, there are no coseismic data to support direct assessment of the locked zone down-dip limit. Instead, geodetic studies have been focused on interseismic deformation (e.g. *Hyndman and Wang*, 1995; *Flück et al.*, 1997; *McCaffrey et al.*, 2007; *Burgette et al.*, 2009) and slow slip events (e.g. *Szeliga et al.*, 2008; *Wech and Bartlow*, 2014; *Michel et al.*, 2018). These studies suggest significant along-strike variations in the locked zone depth and width. The repeat interval of SSEs also vary latitudinally (*Brudzinski and Allen*, 2007). *Brudzinski and Allen* (2007) demonstrated that the recurrence interval for SSEs is about 14 months in Washington, 2 years in central Oregon, and 10 months in northern California.

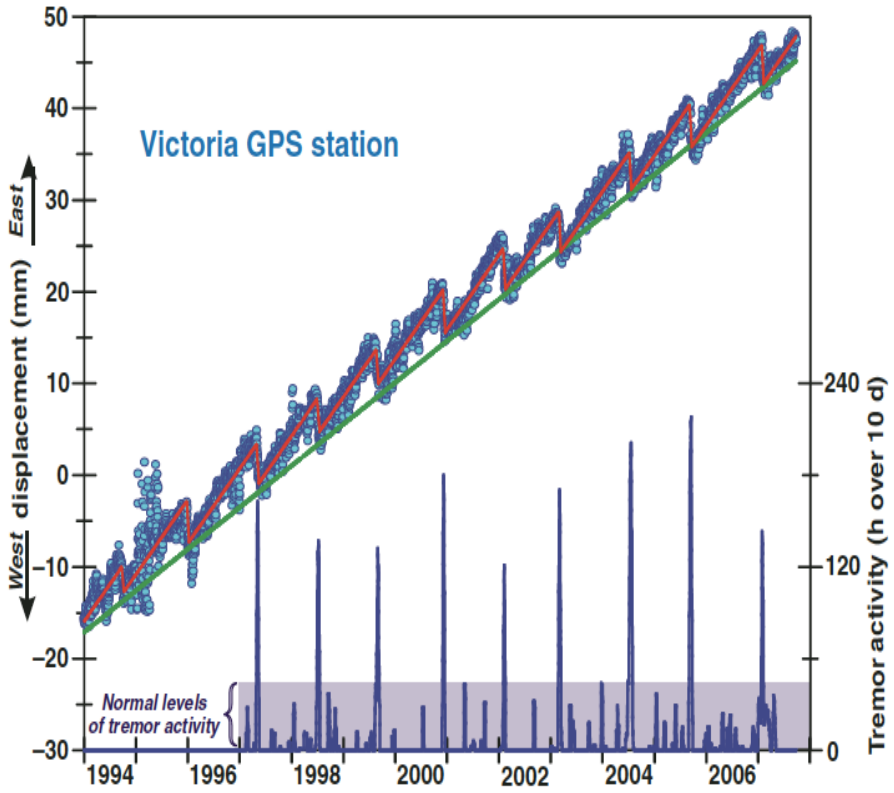

Figure 2.3: Comparisons of slip and tremor observed for the Victoria area (*Rogers and Dragert*, 2003). Blue dots are east component recorded by GPS site ALBH in Victoria island. While a long-term eastward motion is apparent (green line), reversals of motion every 13 to 16 month can be clearly identified. These regular reversals of motion correspond to slow-slip events, which correlate with peaks of tremor activities.

2.2 Slow Slip Events in Cascadia

Slow slip events are common to many subduction zones and they differ from fast earthquakes in that they occur periodically and have much slower slip speed. These events have been found in a variety of places such as Cascadia (*Dragert et al.*, 2001; *Miller et al.*, 2002; *Szeliga et al.*, 2008), in southwest Japan (*Hirose et al.*, 1999; *Miyazaki et al.*, 2006), in Mexico (*Kostoglodov et al.*, 2003; *Lowry et al.*, 2001), and also along the San Andreas fault (*Linde et al.*, 1996; *Murray and Segall*, 2005). Slow slip plays an important role in the earthquake cycle and the associated seismic hazard. Hence it is important to understand how and why slow slip occurs.

Slow slip events were first seen in Japan, and subsequently was first discovered in Cascadia via GPS measurements. Fig. 2.3 shows the eastward motion recorded by a GPS site on Victoria island between 1996 and 2003. While the GPS site exhibits a long-term eastward motion, regular reversals of motion can be clearly identified and are related to slow slip events. Recognition of the slow-slip phenomenon in Cascadia has revealed a zone at depths of approximately 25 to 40 km on the plate boundary where faults, or portions of faults, slip in ways intermediate between end-member behaviors of stick-slip and steady creep (*Dragert et al.*, 2001; *Miller et al.*, 2002). These aseismic events occur with surprising regularity along the length of Cascadia, and are always accompanied by tremor, hence also often known as Episodic Tremor and Slip (ETS). Typically a slow slip event in Cascadia lasts for one to five weeks and results in approximately 5 mm surface displacement.

Progress in understanding SSEs in Cascadia have led to additional understanding of the strength of coupling of the interface between the subducting Juan de Fuca plate and overlying North America plate. Since SSEs originate in the region between the

locked zone, which was estimated to be offshore at plate boundary depths of < 15 km (*Hyndman and Wang*, 1995), and the steady creeping zone below, analyses of SSEs suggest that the locked zone and the down dip rupture limit of future great earthquakes may extend 60 km farther inland (*Chapman and Melbourne*, 2009). Since there is no historical record of the last megathrust earthquake (Mw ~ 9) in Cascadia that happened in the year 1700, the constraint from SSEs can serve as a primary control for the determination of the down dip rupture limit for the Cascadia region.

Another significant practical implication from studies of SSEs is the connection between these benign slow slip phenomena and destructive earthquakes. Although SSEs themselves are not dangerous and accommodate $\sim 50\%$ of the relative plate motion on the plate boundary (*Chapman and Melbourne*, 2009), they can significantly perturb the stress field acting on the locked zone and surrounding faults. A number of authors have discussed the possibility of SSEs triggering or even evolving into large earthquakes (*Rubinstein et al.*, 2009; *Segall and Bradley*, 2012). Most geodetic observations of slow slip in Cascadia so far have been made using GPS techniques. Inversion of GPS data has limited resolution due to the low spatial density of GPS stations. InSAR and GPS are fully complementary in that InSAR provides high spatial resolution measurements with wide coverage. Therefore, the adoption of InSAR techniques has the potential of providing new insights in the exploration of slow slip phenomena in the Cascadia subduction zone.

2.3 InSAR in Cascadia

The InSAR technique combines interferometry and conventional Synthetic Aperture Radar (SAR) and observes the phase differences between two SAR images. The resulting interferometric phase is proportional to the change in range over time between

the radar instrument and the ground (*Massonnet and Feigl*, 1998; *Bürgmann et al.*, 2000). While the InSAR technique allows us to map mm-cm level deformation over wide areas with meter-level resolution, three factors limit the application of InSAR techniques in observing slow slip events in Cascadia:

- Small signal strength

  Slow slip signals measured by GPS typically have a peak displacement amplitude of $\sim$ 0.5cm – 1 cm, which will only account for 1/24 to 1/12 cycle of phase in L-band (24 cm wavelength) interferograms.

- Decorrelation

  If the imaged surface has rapidly changing scattering properties (e.g., the growth of vegetation will change the surface scattering property rapidly), then the radar signals will decorrelate and no meaningful measurements are possible.

- Atmospheric noise

  The spatiotemporal heterogeneity of water vapor contents in the lower atmosphere causes variance in time delays of the radar signal as it propagates through the atmosphere, which overprints on the desired deformation signals.

Since Cascadia has a vast forest cover due to abundant rainfall and mild climate, interferograms formed in this region have large decorrelated areas. Furthermore, where measurement is possible, the relatively small slow slip signal of about 1 cm is overprinted by signal due to the variability in the atmospheric phase delay which can reach 2 cm rms at large scales (*Zebker et al.*, 1997), plus satellite orbit errors and residual topographic correction errors. Therefore, it is almost impossible to determine slow slip signals using individual interferograms.

InSAR time series analysis, a class of techniques that extends conventional InSAR, has been developed to address these limitations. The most used algorithms include

stacking, persistent scatter InSAR, and small baseline InSAR. These algorithms work reasonably well in areas of interferograms with small to moderate decorrelation. Cascadia has always been a challenging region for the application of InSAR due to its heavy vegetation and as a result, there are few examples of InSAR studies over the region. In this dissertation, we focus on extending the limits of InSAR applicability in Cascadia region by extending or developing novel methodologies and techniques to retrieve small slow slip signals in low SNR measurements.

Chapter 3

InSAR: Background

This chapter presents the basics of Synthetic Aperture Radar (SAR) and Interferometric SAR (InSAR) processing.

3.1 SAR imaging

Synthetic Aperture Radar (SAR) refers to a signal processing method that creates an image of the Earth's surface using radar from a spaceborne or airborne platform. Spaceborne SAR was first introduced to Earth remote sensing with the 100-day NASA SEASAT mission in 1978 (*Cumming and Bennett*, 1979). Unlike optical data, SAR provides all-weather, day and night imaging capability and can produce meter-level resolution images covering areas on the order of tens of thousands of square kilometers. The launch of European Remote Sensing satellite ERS-1 in 1991 enabled SAR to continuously orbit the Earth and deliver images on a reliable and operational basis for applications such as mapping, oceanography, agriculture, forestry and so on. Since then, more satellite sensors devoted to remote sensing have been launched and the ever-growing SAR data availability and user interests have stimulated the development of many new applications. Interferometric SAR, the technology we focus on

in this thesis, is one of the most exciting developments.

3.1.1 Geometry

Fig. 3.1 depicts the imaging geometry of a spaceborne SAR system. As the satellite moves along its orbit at a height h with a velocity v, the radar instrument mounted on the satellite points a radar beam roughly perpendicular to the satellite motion towards the Earth and illuminates a swath on the ground. The transmitted radar echoes are phase encoded and reflect off scatterers in the illuminated swath and are recorded by the radar instrument mounted on the satellite at a later time. The time delay of the received echoes is proportional to the distance between the radar instrument and illuminated scatterers in the swath. The intensity of the received radar echoes are determined by the imaging geometry (radar echo incidence angle θ – the angle between the normal to the ground surface and the radar echo propagation direction, satellite height h, etc.) and the radar reflectivity of scatterers on the ground.

Unlike data collected by optical sensors, SAR data requires extensive two-dimensional phase-sensitive signal processing in order to form a focused image. One dimension is parallel to the radar beam, which we define as the range direction or the across-track direction. The other dimension is along the satellite motion direction, and is often referred to as the azimuth direction, or the along track direction. In the range direction, a pulse compression technique is used to concentrate reflected energy from scatterers located in range from the radar. In the azimuth direction, the difference in Doppler shift in the reflected energy from scatterers located at different azimuth locations is utilized to improve resolution to one-half of the antenna length. In the following section, we will briefly review key SAR processing steps. Detailed discussions can be found in *Curlander and McDonough* (1991) and *Cumming and Wong*

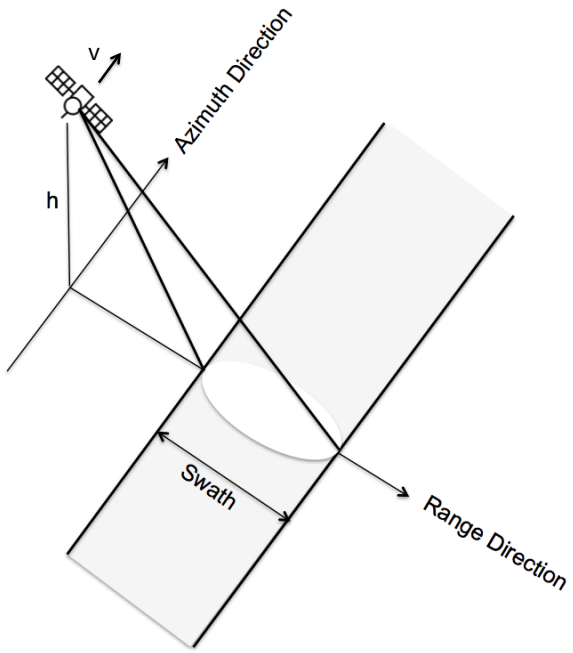

Figure 3.1: Illustration of the imaging geometry of a spaceborne SAR system. The radar antenna mounted on a satellite at height h sends out a signal that illuminates a swath on the ground. The azimuth direction is the satellite motion direction and the range direction is parallel to the radar beam.

(2005).

3.1.2 Range and Azimuth Compression

We can think of raw SAR data as a 2-D function of range and azimuth. It is convenient to consider SAR processing first in the range and then in the azimuth direction.

In the range direction, the radar antenna often sends out a linear frequency modulated (FM) pulse (often referred to as a chirp) given by

$$s_p(t) = rect(\frac{t}{T})exp\big(j(2\pi f_c t + \pi K t^2)\big) \tag{3.1}$$

where t is range time, T is pulse duration, f_c is carrier frequency and K is the FM rate of the pulse. Linear FM pulses have a constant amplitude in the time domain and provide a uniformly filled bandwidth in the frequency domain. What's more, linear FM signals arise naturally in the azimuth direction due to sensor motion. In reality, the transmitted signal is real-valued and quadrature demodulation is used to generate base-band and complex signals. The reflected energy from the illuminated swath is a convolution of the chirp s_p and the ground reflectivity g:

$$s_r = g * s_p \tag{3.2}$$

We can significantly enhance the radar performance in the range direction by optimally filtering (correlating) the received signal with a replica of s_p. Therefore, the impulse response in the time domain is approximately a sinc function for a large time-bandwidth product ($T \cdot BW = T \cdot KT = KT^2$):

$$s_{imp}(t) \approx Tsinc(KTt) \tag{3.3}$$

The range resolution δ_R, is given by

$$\delta_R = \frac{c}{2BW} = \frac{c}{2|K|T} \tag{3.4}$$

As aforementioned, the radar echo is also a chirp function in the azimuth direction. As the radar instrument moves forward, it transmits radar echoes at the pulse repetition frequency (PRF). Therefore, each target on the ground is illuminated by multiple radar pulses. The received signals have the same waveform, but are shifted in frequency due to the relative movement between the radar instrument and the illuminated scatterer in the swath, an effect that is in analogy with the well known "Doppler effect" in physics. Assuming a simple geometry as shown in Fig. 3.1 where

the radar antenna sends out radar pulses sideways with zero squint angle (i.e., the radar antenna does not look ahead nor look back), the phase history of an illuminated scatterer in the swath is approximately

$$\phi(t) = -\frac{4\pi}{\lambda}(r_0 + \frac{v^2 t^2}{2r_0^2}) \tag{3.5}$$

where λ is the wavelength corresponding to the central frequency f_c of the chirp pulses, r_0 is the distance between the radar instrument and the scatterer when they are at the closest approach, and v is the velocity of the radar instrument. Comparing (3.5) with (3.1), we can define the azimuth FM rate as

$$K_{az} = \frac{1}{2\pi}\frac{d^2\phi(t)}{dt^2} = -\frac{2v^2}{\lambda r_0} \tag{3.6}$$

The time that the scatterer is illuminated by the radar pulses is approximately

$$\tau_{az} = \frac{r_0\lambda}{vl} \tag{3.7}$$

where l is the length of the antenna. $r_0\lambda/l$ is approximately the beam-width in the azimuth direction and is also referred to as the "synthetic aperture length". Hence the bandwidth in the azimuth direction is

$$BW_{az} = |K_{az}| \cdot \tau_{az} = \frac{2v}{l}. \tag{3.8}$$

The azimuth resolution δ_{az}, is given by

$$\delta_{az} = \frac{v}{2BW_{az}} = \frac{l}{2}. \tag{3.9}$$

For a typical spaceborne SAR system, both the range and the azimuth resolution are on the order of a few meters.

3.2 InSAR

Interferometric SAR is a technique where two or more SAR images are combined to produce interferograms, which can be used to generate fine measurements of surface topography or crustal deformation over large areas with meter-level resolution (*Zebker et al.*, 1994; *Bamler and Hartl*, 1998; *Rosen et al.*, 1998; *Bürgmann et al.*, 2000, etc.).

3.2.1 Basics

A conventional SAR image is inherently two-dimensional. The InSAR technique combines interferometry and SAR to compute the phase differences between two complex-valued SAR measurements. Given two SAR measurements over the same resolution cell, $s_1 = a_1 e^{i\psi_1}$ and $s_2 = a_2 e^{i\psi_2}$, the interferometric measurement z_{12} is

$$z_{12} = s_1 \cdot s_2^* = a_1 a_2 e^{i(\psi_1 - \psi_2)} \tag{3.10}$$

Therefore, the phase ϕ_{12} of the complex interferometric measurement z_{12} is the phase difference between s_1 and s_2: $\phi_{12} = \psi_1 - \psi_2$, which is determined by the geometric path length difference between the two SAR antennas and the common image point. Depending on the configuration of the InSAR system, interferometric phases can be utilized to provide additional information on the third dimension. The most common interpretations for interferometric phase in Earth observations are topography mapping and crustal deformation.

Fig. 3.2 illustrates the imaging geometry of InSAR. The interferometric phase is proportional to the range difference: $\phi_{12} = \frac{4\pi}{\lambda}(r_1 - r_2)$ and can be related to the

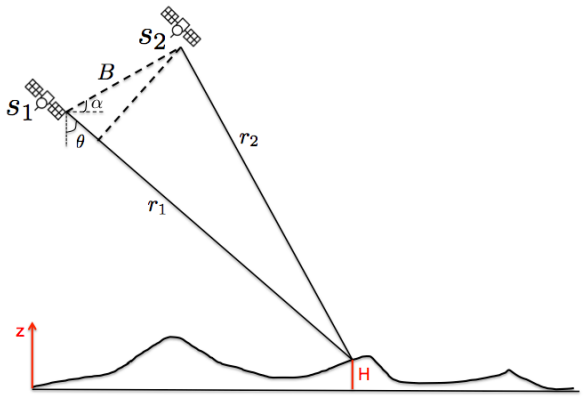

Figure 3.2: Illustration of the imaging geometry of a spaceborne SAR system. The interferometric phase ϕ_{12} between measurements collected by S1 and S2 is proportional to the range difference $r_1 - r_2$, and can be related to the topographic height H of the image point given the imaging geometry, which can be defined by the look angle θ, the baseline B, and the angle α which is the angle the baseline makes with respect to a horizontal plane.

topographic height H of the image point given knowledge of 1) the look angle θ, which is the angle between the line-of-sight direction and nadir, 2) the relative position of the two SAR antennas, which can be characterized by the baseline B, and 3) the angle α, the angle the baseline makes with respect to a horizontal plane. The performance of topographic mapping with InSAR relies on how accurately we can measure phase uncertainties, the baseline between the antennas as well as the distance between the antenna and the imaging point:

$$\delta z \approx \frac{r}{B} \cdot \delta r. \tag{3.11}$$

$$\delta r = \frac{\lambda}{4\pi} \delta\phi \tag{3.12}$$

As an example, with $r = 800$ km, $B = 1$ km, and $\delta r \approx 0.06$ cm, we have $\delta z = 0.5$ m. The first demonstration of using an InSAR system for topographic mapping was by *Graham* (1974). More sophisticated systems were later implemented with airborne systems (*Zebker and Goldstein*, 1986) and spaceborne platforms (*Goldstein et al.*, 1988).

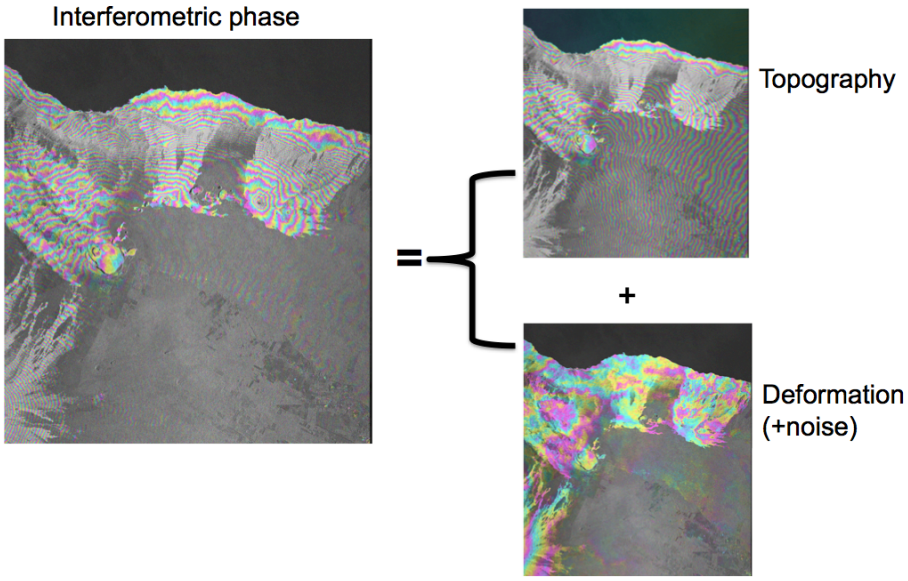

Figure 3.3: Decomposition of the Interferometric phase formed from two SAR acquisitions taken over the Kilauea volcano in Hawaii. Interferometric phase contains signals from 1) the local topography due to the spatial separation of the sensor locations and 2) any radar line-of-sight displacements of the imaged target occurring between the two SAR acquisitions.

InSAR systems designed for topography mapping (e.g. TanDEM-X) have both antennas image the surface simultaneously so that the imaged surface can be considered stationary. Alternatively, if we know the topography of the imaged area, and the surface is imaged by the interferometer at different times, we can measure motion of the surface between the two radar measurement times after removing phases related to topography. Motion mapping is perhaps the most relevant to the Earth science community, and has been extensively applied in studies as diverse as earthquake and volcano modeling, glacier mechanics, and hydrology.

Fig. 3.3 illustrates that by removing topographic fringes from interferometric phase measurements, we are left with deformation signals and other noise terms. After topography correction, the interferometric phase can be represented as the sum

of deformation and various noise terms:

$$\phi_{ij} = \phi_{def} + \phi_{\epsilon} + \phi_{atm} + \phi_{orb} + \phi_{n}. \tag{3.13}$$

where ϕ_{ϵ} is residual topographic phase after topography correction, ϕ_{atm} is atmospheric phase delay, ϕ_{orb} is introduced by orbital errors, ϕ_{n} represents all other uncorrelated noise sources.

ϕ_{atm} and ϕ_{decor} are the two main noise sources. Atmospheric noise is a result of the spatiotemporal heterogeneity of water vapor content in the lower atmosphere, causing variance in time delay of the radar signal as it propagates through the atmosphere (e.g. *Goldstein*, 1995; *Zebker et al.*, 1997; *Emardson et al.*, 2003). Since the revisit time of SAR satellites is on the order of days, atmospheric noise is essentially uncorrelated in time but correlated in space and is often modeled as a long-wavelength artifact in individual interferograms (*Hanssen*, 2001; *Emardson et al.*, 2003; *Lohman and Simons*, 2005; *Onn and Zebker*, 2006). Decorrelation, on the other hand, can be related to changes between radar measurements in surface scattering properties, imaging geometries and thermal noise among others (*Zebker and Villasenor*, 1992; *Just and Bamler*, 1994). The level of decorrelation is often quantified by the correlation coefficient ρ. The mechanisms of signal deorrelation have been well studied, and can mainly be attributed to changes of surface scattering properties during the observation time span, geometrical decorrelation, and system and other thermal noises (*Zebker and Villasenor*, 1992).

ϕ_{orb} represents phase ramps introduced by inaccurate orbit locations and can usually be removed by fitting planar or bi-linear models. Note that for modern SAR

satellites such as Sentinel-1, phase noise caused by orbital errors is rare. ϕ_ϵ is another common systematic noise source caused by inaccurate digital elevation models (DEM).

3.2.2 InSAR time-series techniques

InSAR time-series techniques are a class of methods that utilize a network of interferograms other than individual interferograms to obtain information about temporal evolution of surface deformation.

1. Stacking

Stacking is a simple yet effective method for dealing with poor quality InSAR measurements. By simply summing or stacking many interferograms, the signal to noise ratio of InSAR measurements improves because deformation signal reinforces while other phase components typically cancel out (*Simons and Rosen*, 2007; *Wright et al.*, 2001; *Zebker et al.*, 1994). In this thesis, we discuss the method of stacking in detail and how error propagates through interferometric stacks.

2. Persistent Scatterer Analysis

The SAR measurement of a ground resolution element is the coherent sum of contributions from all scatterers within the resolution cell. Relative movements of the scatterers as well as changes in viewing angles of the radar platform will result in a different summation and hence causes decorrelation in the interferograms. However, if a resolution cell is dominated by a single scatterer, i.e., the dominant scatterer returns significantly more energy than the other scatterers, the total returned signals are much more stable. These pixels are called persistent scatterers (PS). In this work, we did not adopt this method.

3. Small baseline SAR (SBAS)

The small baseline methods minimize decorrelation by only using interferograms formed with small spatial and temporal baseline. Spatial averaging is often used to further decrease decorrelation. Based on prior knowledge of the deformation signal, phase inversion methods such as least-squares (*Schmidt and Bürgmann*, 2003), singular value decomposition (*Berardino et al.*, 2002), or L-1 norm minimization (*Chen et al.*, 2014) can be used to obtain temporal evolution of phase values, hence time series of displacements.

Chapter 4

Efficient and User-friendly InSAR Processing

Despite its applicability to a diverse set of problems and the promising potential of modern SAR satellites, InSAR remains a challenging technique for non-specialists, which significantly limits its potential for widespread use. The need for familiarity with methods of radar processing, acquisition coordinate systems, and detailed metadata describing imaging geometry, satellite orbit state vectors, and instrumental configuration often limits studies by scientists who are mainly concerned with measurements of geophysical processes and their interpretation. Furthermore, with modern sensors now acquiring data at weekly intervals or faster, the number of radar interferograms available for analysis over any area of interest can be in the thousands, so even downloading the data over electronic networks remains a bottleneck.

Here we describe a method that enables delivery of data products that can be easily reduced to the desired observations and are less constrained by the sheer volume of data that must be transferred to an end user. Our approach addresses the limitations of specialized knowledge and data volume, delivering products that are

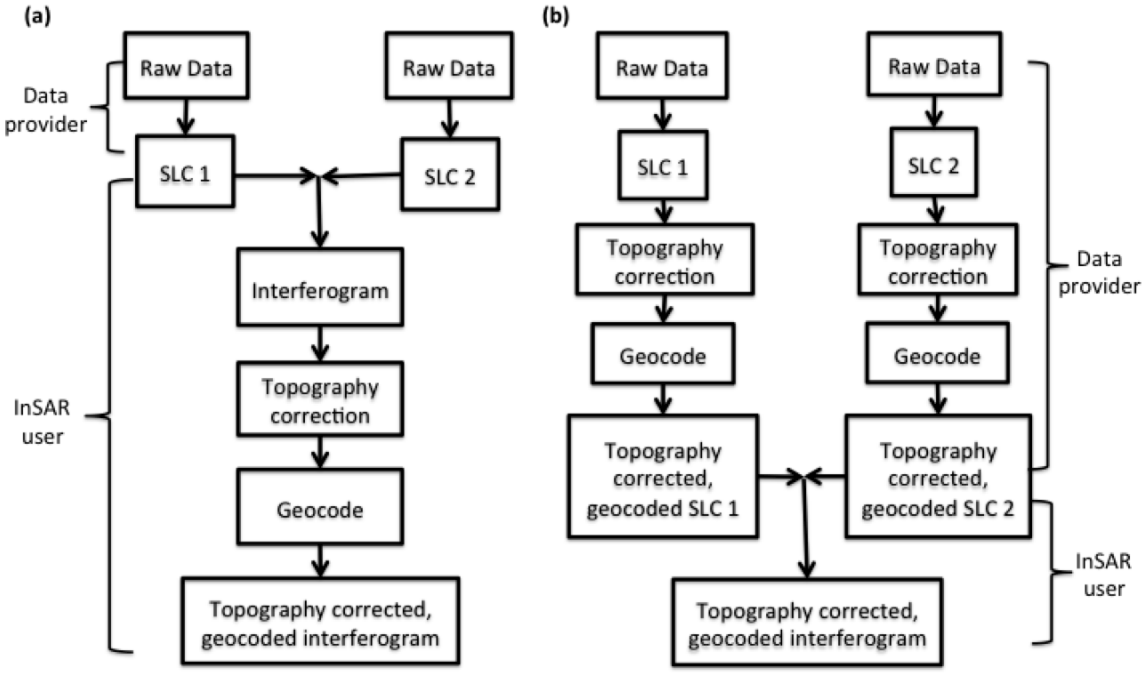

Figure 4.1: (a) Traditional InSAR processing workflow. (b) Proposed InSAR workflow

identical in accuracy to existing processors' capabilities but are easy to use.

In this chapter, we first discuss the concept of topography corrected and geocoded SAR and illustrate why it is useful. We then introduce its implementation in the frame of motion-compensation techniques, though the concept is general and can be easily integrated in other InSAR processing flows. Finally we present examples of topography corrected and geocoded Sentinel-1 SAR products.

4.1 Topography Corrected, Geocoded SAR

For many applications, we are primarily interested in mapping the surface deformation over time and therefore need to remove topography-related signals from interferograms. Fig. 4.1(a) shows a typical InSAR processing and product delivery flow. InSAR users first acquire SAR data in the form of either raw data or a single-look complex (SLC) image from data providers and then process the acquired data into topography corrected and geocoded interferograms, which can then be used in various geophysical applications. Even with sophisticated InSAR software such as ROI PAC (the Repeat Orbit Interferometry PACkage) or ISCE (InSAR Scientific Computing Environment), the additional InSAR processing needed to form the deformation history is not always an easy task. The complexity of InSAR processing can make a single successful run of the processing flow unlikely. More often than not, InSAR users have to stop the flow at various points to either modify parameters or fix errors. Consequently, InSAR data users, most of whom are not InSAR experts, are required to be considerably familiar with the detailed imaging geometry for each SAR acquisition, and also to be experienced in InSAR processing techniques. Here we show that an alternative InSAR processing approach moves the need for precise knowledge of imaging geometry and radar techniques upstream from the end-users to the data providers, so users need only be concerned with common GIS-style data analysis (Fig. 4.1 (b)). We facilitate this by correcting topography-related signals from each SLC image, and resampling the compensated SLC images into latitude-longitude coordinates for easy ingestion to image processing packages. Interferograms generated by simple cross-multiplication of pairs of these processed SLC images are thus automatically topography corrected and can be readily used for subsequent geophysical modeling. In this way, we separate InSAR processing from InSAR application, thus making the use of InSAR data easier for non-expert InSAR users.

The other major advantage of our alternative approach is that it greatly reduces the computational resources needed to compute deformation time series. For N SLC radar images, $N(N-1)/2$ interferograms can be formed and hence $N(N-1)/2$ topography correction computations are needed in the traditional processing approach. Common analyses widely used today for investigating temporal evolution of surface deformation, such as the small baseline subset (SBAS) (*Berardino et al.*, 2002) and persistent scatterer (PS) (*Ferretti et al.*, 2001; *Hooper et al.*, 2007), typically use as many SAR interferograms as possible. Each of these requires the detailed metadata described above plus the software and computer resources to compute the correction. In contrast, in our new approach the data provider applies the topography compensation rather than the end user, and further only N topography correction steps are needed. With more and more SAR data available nowadays and in the foreseeable future, our approach can significantly improve the efficiency of interferogram formation.

Many technical paths to compensate radar interferograms and SLC images for geometry and topography are possible, and we propose one such flow here. If applied properly, all of these will produce similarly accurate data sets. Our method has the advantage of delivering low volume and readily ingestible images, greatly increasing the number of persons who can feasibly use the observations. Here we demonstrate one such method and show how it can be applied to either raw radar data or to SLC products as now produced by many of the international constellation of radar satellites.

This is not the first time that the idea of correcting SLC images for topographic effects has been proposed. *Ferretti et al.* (2001) introduced zero-baseline steering in order to compensate slave SLC images with respect to a chosen master SLC image for

topographic effects, however the correction is applied to interferograms rather than the SLCs directly. (*Schmitt and Stilla*, 2014) used the absolute signal phase in a single SLC image as a function of topography to infer scatterer height in SAR tomography. We combine and extend the above ideas by first adopting motion-compensation techniques to propagate actual radar echoes to a virtual ideal orbit as suggested by *Zebker et al.* (2010), and then, with an external digital elevation model (DEM), compensating each SLC image for the residual topographic phase contribution. The advantage of using a common ideal orbit rather than a master orbit is that the imaging geometry equations are particularly simple and therefore topographic correction is efficient to implement. The motion compensation techniques can equally well be applied either to the generation of the SLC images, or to the zero-Doppler SLC products produced by many sensors today (e.g., Sentinel-1A/B, Radarsat-2, COSMO-SkyMed or ALOS-II). We present results from data acquired by the Italian COSMO-SkyMed satellites and the Japanese ALOS satellite to demonstrate the use of our method for preprocessed SLC images and raw data products, respectively. Since our method needs topography information for phase correction, its performance depends on the quality of the DEMs used. Thus the new processing method may not work well over areas where only poor-quality DEMs are available.

Because we have the precisely coregistered DEM along with each SLC product, we also geocode the SLCs prior to distribution. Each end-user is thus presented data in a well-understood latitude/longitude system rather than in a radar-specific and varying set of range/Doppler coordinates, relieving the user again of a task that requires a metadata analysis in order to generate useful observations.

4.2 Implementation

Our processing approach removes topography-related signals from individual SAR scenes. This makes interferogram formation not only simpler and possible by non-experts, but much more computationally efficient when large SLC stacks are analyzed.

4.2.1 Topographic Correction Review

Uncompensated interferograms contain topography-dependent phase terms (*Rosen et al.*, 1998). Fig. 4.2 shows the geometry of an InSAR system. The radar path length difference $\delta\rho$, which we observe as interferometric phase ϕ between the two SAR scenes, consists of two parts: ϕ_{topo} and ϕ_{disp}. The first part, ϕ_{topo}, is due to the difference in geometrical path length from each of two sensor locations to the imaging point and depends on the spatial baseline $\vec{B}$. The other part, ϕ_{disp}, is due to any surface displacement $\vec{D}$ that occurs between radar observations. For a narrowband signal in the far field of the antenna, the observed interferometric phase is (*Zebker and Goldstein*, 1986; *Rosen et al.*, 1996)

$$\phi = \phi_{topo} + \phi_{disp} = \frac{4\pi}{\lambda}(-\vec{u}\cdot\vec{B} + \vec{u}\cdot\vec{D}) \tag{4.1}$$

where $\vec{u}$ is a unit vector representing the radar look direction. For displacement mapping, we need to remove the topographic phase term $\phi_{topo} = \frac{4\pi}{\lambda}(-\vec{u}\cdot\vec{B})$.

We adopt coordinates defined by a virtual perfectly circular orbit above a non-rotating planet (*Zebker et al.*, 2010) for easy calculations $\vec{u}$ and $\vec{B}$. This coordinate system greatly simplifies the equations describing the imaging geometry. We then use a motion compensation approach to translate raw radar echoes from their actual

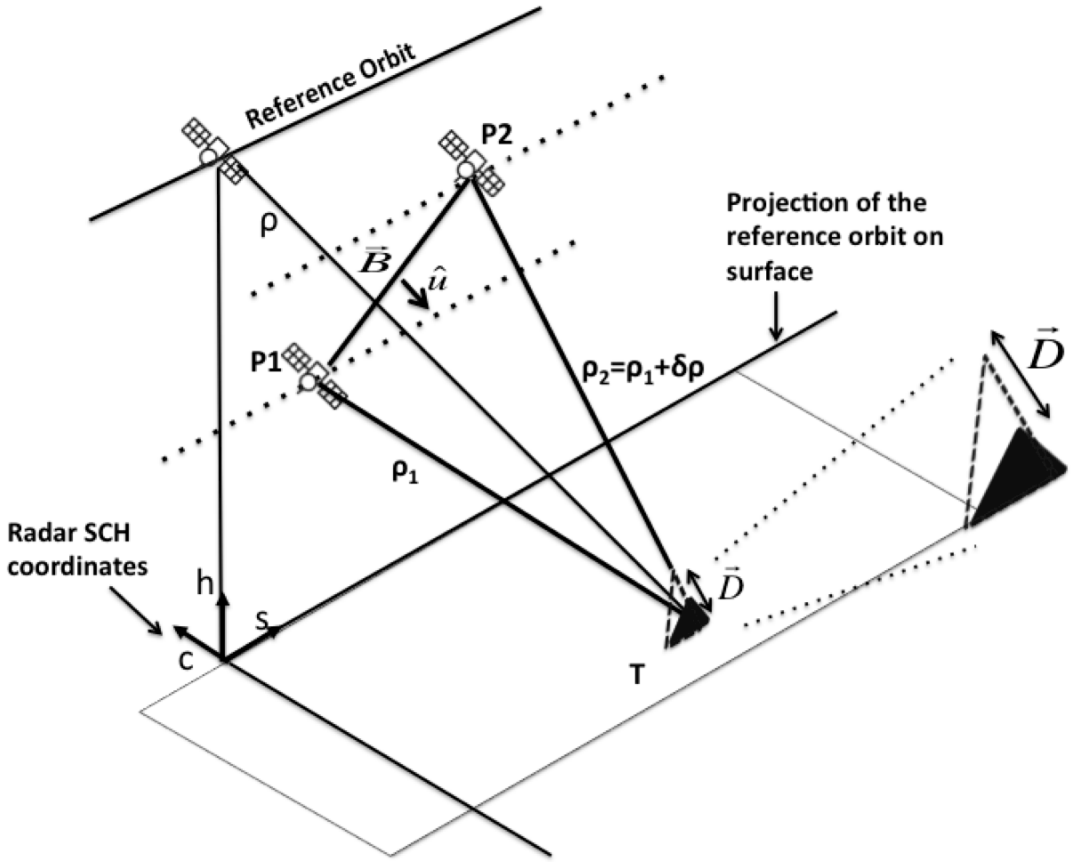

Figure 4.2: Radar imaging geometry and the SCH coordinate system. P1 and P2 represent two satellite locations at distinct SAR acquisition times. T is the imaged point on the ground, $\hat{u}$ is the unit radar LOS vector, and ρ_1 ,ρ_2 are the distance that radar signals travelled in the two acquisitions. The difference $\delta\rho$ between the two radar path lengths is related to 1) baseline $\vec{B}$ between the sensor locations P1 and P2 , and 2) any surface motion $\vec{D}$ of the target T between radar observations. The SCH coordinates are aligned with the reference orbit path. The curvature of the earth is considered in the study but not shown in this figure.

positions to what would be observed if the satellite were traveling in the ideal reference orbit (*Zebker et al.*, 2010). We then co-register the SLC images. Since motion compensation has already resampled all SLC images with respect to the reference orbit geometry, the co-registration step is very efficient.

Motion compensation essentially sets the effective InSAR baselines $\vec{B}$ to zero such that the topographic phase term is zero for points located on the surface. However, the topographic phase contribution is still present for any non-zero topography. It can be evaluated from (*Zebker et al.*, 2010)

$$\phi_{topo} = \frac{4\pi}{\lambda}(\vec{u}^{elev} - \vec{u}^{ref}) \cdot \vec{B} \tag{4.2}$$

where the multiple $\vec{u}$ are the unit vectors representing radar look directions from the sensor location to the pixel at actual elevation and on the zero-elevation reference sphere, respectively. We must calculate the remaining topographic phase term and remove it from the interferogram before interpreting the deformation signals.

4.2.2 Separation of Topographic Correction Term

We compensate the individual SLC images before interferogram formation, so that the computed interferogram does not include the topographic phase term from each SAR scene. To do so, we divide the baseline vector into two parts

$$\vec{B} = \vec{P}_1 - \vec{P}_2 \tag{4.3}$$

where $\vec{P}_{1,2}$ are the position vectors of the actual locations of the SAR sensors in the reference coordinate system. The difference in radar LOS vectors can be expressed

as

$$\vec{u}^{elev} - \vec{u}^{ref} = \frac{\vec{P} - \vec{T}^{elev}}{|\vec{P} - \vec{T}^{elev}|} - \frac{\vec{P} - \vec{T}^{ref}}{|\vec{P} - \vec{T}^{ref}|} \tag{4.4}$$

where $\vec{P} = \frac{1}{2}(\vec{P}_1 + \vec{P}_2)$, the midpoint between the two antenna locations. Since $|\vec{P} - \vec{T}^{elev}| \approx |\vec{P} - \vec{T}^{ref}| \approx \rho$, where ρ is the range from the reference sensor position to the imaged point we can approximate the above equation as

$$\vec{u}^{elev} - \vec{u}^{ref} = \frac{1}{\rho}(\vec{T}^{ref} - \vec{T}^{elev}) \tag{4.5}$$

The approximation is valid since all InSAR measurements are made far field. Because the target location $\vec{T}$ depends only on the reference geometry, the term $\vec{u}^{elev} - \vec{u}^{ref}$ is independent of individual sensor locations, and

$$\phi_{topo} = \phi_{topo}^{S_1} - \phi_{topo}^{S_2} \tag{4.6}$$

where

$$\phi_{topo}^{S_i} = \frac{4\pi}{\lambda}(\vec{u}^{elev} - \vec{u}^{ref}) \cdot \vec{P}_i, \qquad i = 1, 2 \tag{4.7}$$

This yields the topography-related phase for each individual SLC image, so we can generate topography-corrected SLC images that no longer contain a topography dependent phase signature. Interferograms formed by simple cross-multiplication do not require further baseline corrections.

It is worth noting that in principle we are able to separate the topographic correction phase into parts dependent only on each orbits imaging geometry as long as a common reference coordinate system is defined. Motion compensation is not a prerequisite to our approach, but it makes processing easily implemented and efficient by co-registering the SLCs to a common coordinate system.

4.2.3 Comparison with traditional methods

The biggest difference between our proposed processing approach and the traditional method is where we apply the topography correction in the InSAR processing flow (Fig. 4.1). Our method separates the topography correction term into parts that depend only on individual SLC images and hence moves topography correction step upstream from interferogram-level to SLC-level. By doing so, InSAR data users can avoid complicated InSAR processing and start straight from compensated SLC images that directly produce topography corrected and geocoded interferograms. Moreover, since topography correction steps are needed fewer times at the SLC-level than at the interferogram-level, the overall efficiency of InSAR processing is improved.

Our approach also moves geocoding step upstream from interferogram-level to SLC-level. Therefore we resample SLC images into latitude-longitude coordinates before forming interferograms. Since multi-looked interferograms are used for most geophysical applications, errors that may be introduced by the additional resampling step before interfering are insignificant. Even if single-look interferograms are required for some special applications, SLC images that are topography corrected but not geocoded can still be provided.

Our proposed approach in the end generates, in principle, interferograms with the same accuracy as produced by traditional methods – we only alter the sequence of processing steps. Therefore, interferograms generated using our approach are still subject to InSAR phase noise such as orbital ramps, atmospheric noise and decorrelation. However, correction of these noise terms is often either empirical or based on stochastic models and hence, less demanding for users knowledge of InSAR processing techniques and detailed InSAR imaging geometry.

The inclusion of motion compensation techniques in our approach makes InSAR processing faster and more accurate. Most importantly, motion compensation facilitates efficient image co-registration (*Zebker et al.*, 2010) as we seek to produce co-registered, geocoded and topography-corrected SLC images. Motion compensation techniques are also implemented in the existing InSAR software ISCE.

4.2.4 Examples

Here we present several images using our new processing method and data from both the Italian COSMO-SkyMed X-band satellites (Level 1 zero-Doppler SLC images) and the Japanese ALOS-1 L-band satellite (Level 0 raw data products). The focus of this section is to show the range of applicability of our approach for different data formats and to demonstrate how our new approach may be used for geophysical modeling by computing SBAS time-series analyses in both product format cases. We also conducted the same analysis using the traditional method and compare the results between our proposed processing workflow and the traditional flow.

COSMO-SkyMed dataset, Central Valley of California

We begin with data delivered in zero-Doppler SLC format. We processed 37 COSMO-SkyMed Level 1A products acquired from June 20, 2012 until May 25, 2014 over the city of Fresno in the Central Valley of California. Due to the ongoing drought in California, intensive pumping of groundwater has resulted in land subsidence that can be easily detected using InSAR (*Galloway and Hoffmann*, 2007; *Bell et al.*, 2008). We formed 62 topography corrected interferograms with baseline values smaller than 100 m – Fig. 4.3 shows their average phase. Location C exhibits an exceptionally

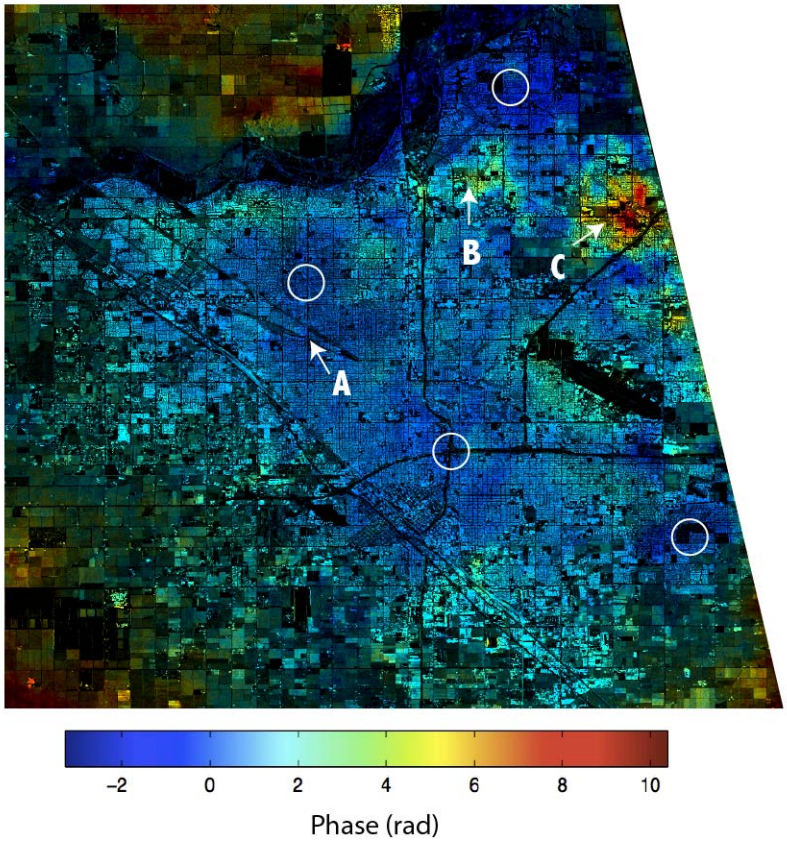

Figure 4.3: Interferogram stack over Fresno, California constructed from 62 topography corrected interferograms formed by 37 COSMO-SkyMed Level 1A products from June 20, 2012 to May 25, 2014. Deformation series at locations A, B, and C are shown in Fig. 4.5. The reference phase is an average of the areas marked by white circles where little deformation is apparent.

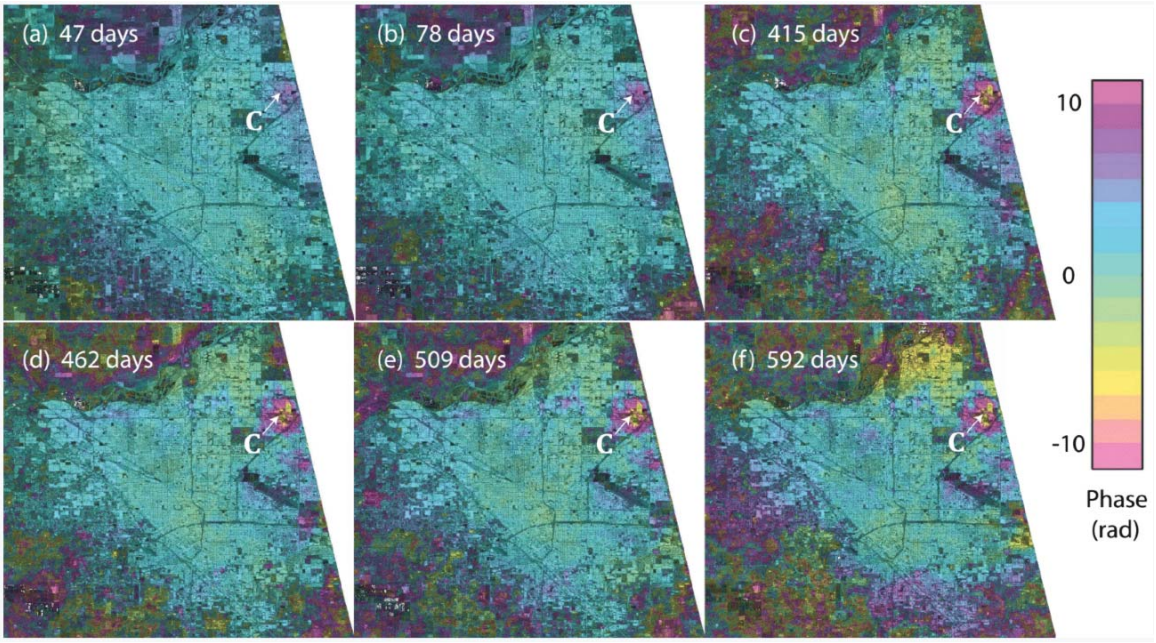

Figure 4.4: Unwrapped interferograms over Fresno, showing time-progressive fringes at location C. Interferograms show change between June 20, 2012, and (a) August 7, 2012, spanning 47 days, (b) September 8, 2012, 78 days, (c) August 10, 2013, 415 days, (d) September 27, 2013, 462 days, (e) November 14, 2013, 509, days, and (f) February 2, 2014, 592 days. All interferograms are corrected for orbital errors by deramping.

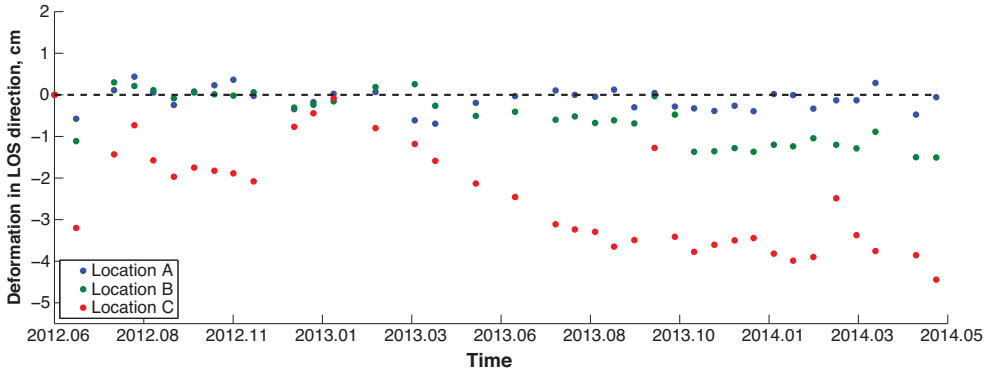

Figure 4.5: Displacement time series at locations A, B, and C (see Fig. 4.3). Location A remained stable during the observation time, while locations B and C subsided between 2013.01 and 2013.10 by $\sim$ 1 cm and $\sim$ 4 cm in radar LOS, respectively.

high phase value, indicating that the region may be sinking relative to its surrounding areas. A sequence of six interferograms generated with respect to one common SAR scene (Fig. 4.4) shows the deformation pattern grows with time. To further investigate the temporal evolution of the detected deformation, we used an SBAS approach (*Berardino et al.*, 2002) to generate displacement time series. As shown in Fig. 4.5, location A exhibits no apparent deformation during the observation time. Location C, in contrast, sinks almost 3 cm (in radar LOS direction) during the time period between January 2013 and October 2013. Location B also has subsided in the same time period of about 1 cm in radar LOS direction. We speculate that perhaps a well started to pump water near location C around January 2013 and caused the subsidence seen in this area.

ALOS dataset, Kilauea, Hawaii

Next, we compute a time series using raw radar data products. Dense spatial and temporal sampling has made InSAR an incredibly useful tool for volcano studies. We generated 66 topography-corrected interferograms from an ALOS Level 0 dataset comprising 25 acquisitions from May 28, 2006 to March 11, 2011, over the Kilauea region, Hawaii. The interferograms generated have a maximum baseline of 500 m and their average phase (Fig. 4.6) shows significant deformation in three areas: Kilauea caldera, Makaopuhi crater and Pu‘u‘ Ō‘ō. We used the SBAS approach to compute the temporal evolution of deformation in these regions (Fig. 4.7). We find that the Makaopuhi crater region uplifted significantly between 15 March 2007 and 8 August 2007. Around the same time, Kilauea caldera and Pu‘u‘ Ō‘ō started to subside. Temporally the observed deformation is associated with the 17 June 2007 Fathers Day intrusion/eruption at Kilauea. The summit caldera likely deflated as magma was transported from Kilauea caldera to the Makaopuhi crater region. It is posited

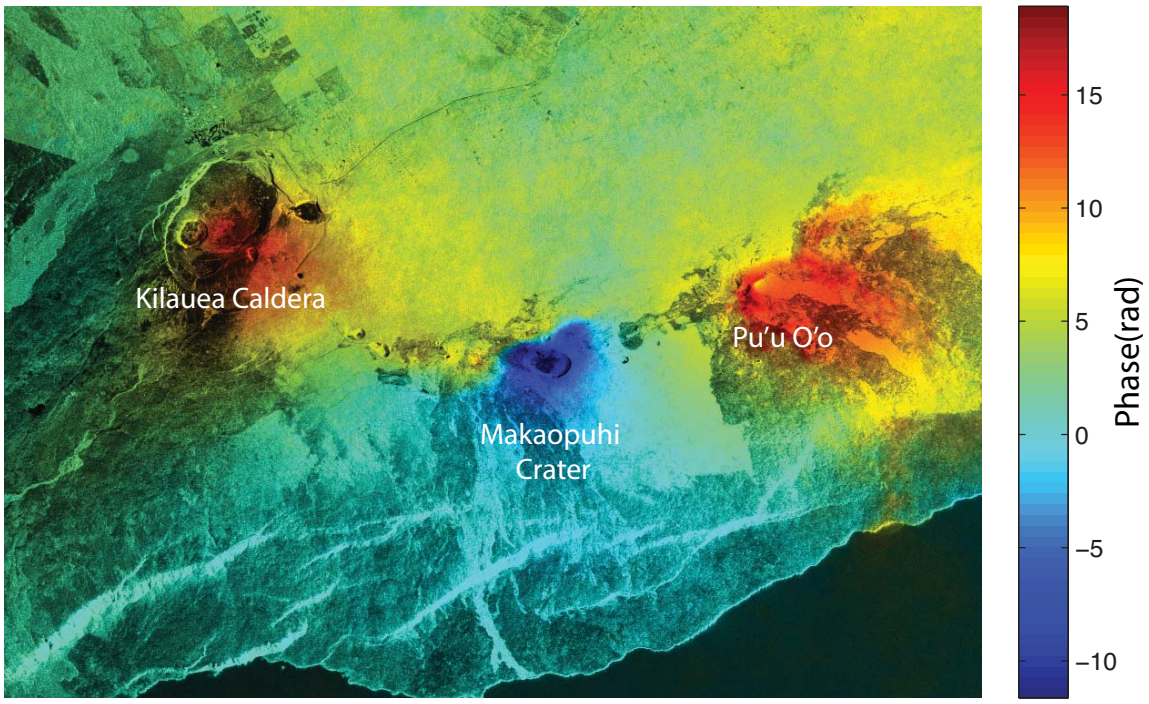

Figure 4.6: Interferogram stack of Kilauea, Hawaii, constructed by averaging 66 topography corrected interferograms created from 25 ALOS Level 0 products acquired from May 28, 2006 to March 11, 2011. Details of the deformation in Kilauea Caledera, Makaopuhi Crater and Pu‘u‘ Ō‘ō region are shown in Fig. 4.7

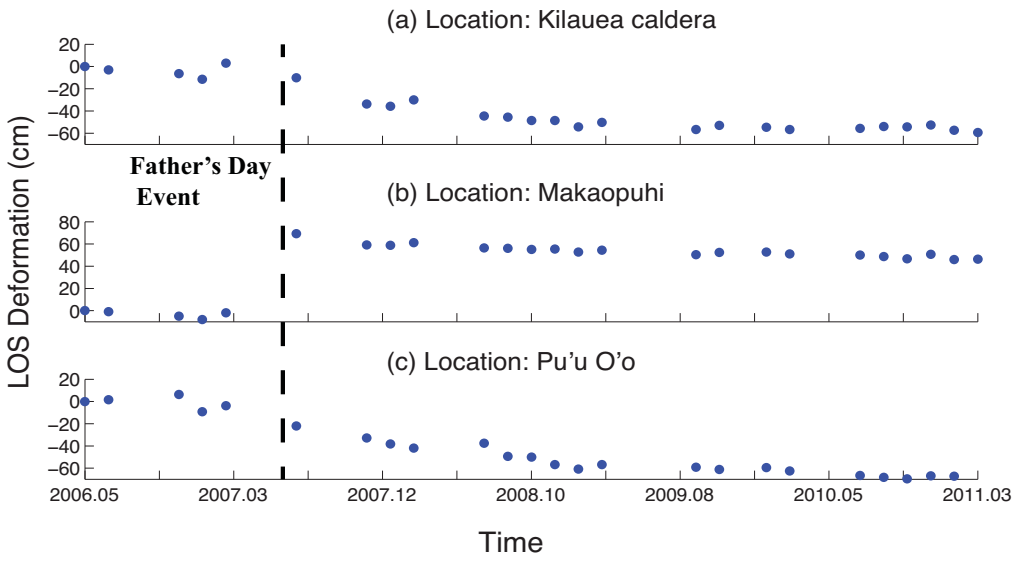

Figure 4.7: Displacement time series at Kilauea caldera, Makaopuhi Crater and Pu‘u‘ Ō‘ō. All three regions show active deformation from mid-2007 to early 2009 and have remained relatively stable afterwards. The June 2007 Father's Day event can be clearly identified as the abrupt rapid uplift in the Makaopuhi crater region with corresponding subsidence in both Kilauea caldera and Pu‘u‘ Ō‘ō region between observations points at March 2007 and July 2007.

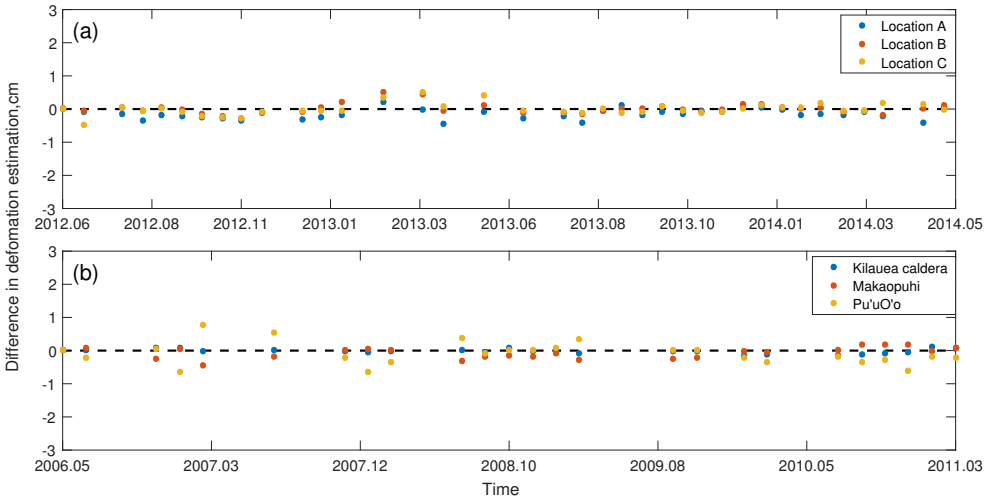

Figure 4.8: Difference in estimated displacement time series using the traditional workflow and the proposed workflow with (a) COSMO-SkyMed dataset and (b) ALOS dataset. The root-mean-square of differences in both cases are around 2 mm.

(*Poland et al.*, 2008) that Pu‘u‘ Ō‘ō’s magma supply was disrupted, causing that region to subside as well. The displacement time-series readily shows uplift in the Makaopuhi crater region (Fig.4.7 b). The similarity in deformation patterns between the Kilauea caldera and Pu‘u‘ Ō‘ō suggests a strong link between the summit magma system and volcanic activities near the Pu‘u‘ Ō‘ō region. Starting 21 July 2007, the lava eruption on the east flank of Pu‘u‘ Ō‘ō resulted in eastward deformation of the region. Kilauea caldera continued to deflate after July 2007 as well, most likely due to supplying magma to the fissure eruption site on the east flank of Pu‘u‘ Ō‘ō (*Poland et al.*, 2008). These events are observed as an approximately 50 cm LOS deformation in both Kilauea caldera and Pu‘u‘ Ō‘ō from July 2007 to January 2009, after which volcanic activity was less frequent and all three regions remained relatively stable.

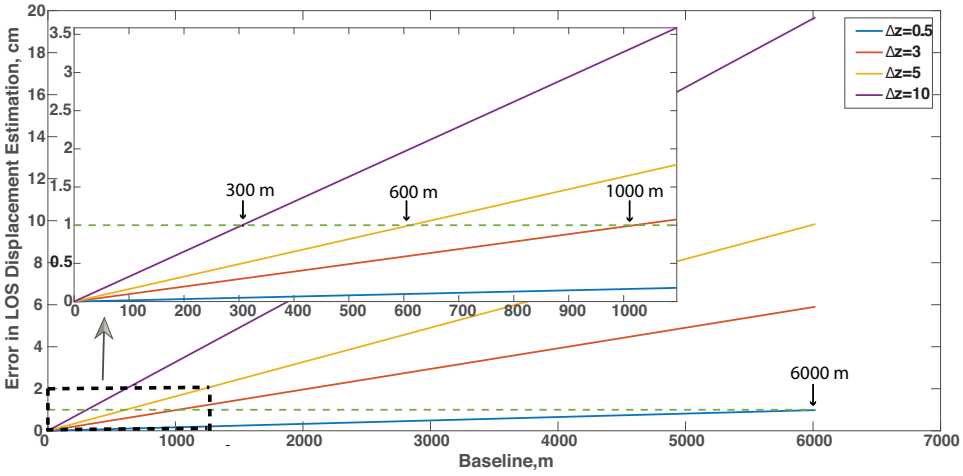

Figure 4.9: Effects of DEM error on estimation of surface displacement in LOS direction calculated using COSMO-SkyMed imaging geometry. The uncertainty in LOS deformation estimation grows linearly with both baseline and DEM errors. For example, if the DEM has a 10 m uncertainty, then the uncertainty in LOS deformation estimation will increase by 1 cm with every 300 m increase in baseline. Or, if a pair of SLC images has a 1000 m baseline, then the uncertainty of estimated deformation increases by 1 cm with every 3 m increase in DEM error.

Comparison with traditional flow

We conducted the same SBAS time-series analysis in both product format cases using the traditional method in order to assess the influence of reversing the order of resampling and interferometry. We find that there is no significant difference between these as the root-mean-square difference of deformation time-series between the two workflows is around 2 mm, as shown in Fig. 4.8.

4.3 Effects of an Imperfect DEM

Our approach relies on the availability of digital topography data, thus any errors in the DEM used will generate imperfections in the derived products. In this section, we quantify the relationship between DEM errors and interferometric phase. DEMs always contain errors and in most cases the resolution of the DEM does not match the resolution of radar images, requiring interpolation. Interpolating a DEM to match the fine resolution of radar images often works well, but this step may also introduce noise into the DEM. As a result, errors are introduced in the estimated topographic phase, and hence the interferograms. Starting with Eqn.[4.2] and Eqn. [4.5], and taking $\vec{T}^{ref} = 0$

$$\frac{\lambda}{4\pi}\phi_{topo} \approx \frac{\vec{T}^{elev} - \vec{T}^{ref}}{\rho} \cdot \vec{B} \approx \frac{\vec{T}_h^{elev} B_h + \sum_{i=s,c}(\vec{T}^{elev} - \vec{T}^{ref})B_i}{\rho} \tag{4.8}$$

where subscripts s, c, h stand for the SCH coordinate system axes used here. The SCH coordinate system is a special coordinate system that aligns with the radar geometry (*Zebker et al.*, 2010). The s and c coordinates are along-track and across-track ground coordinates respectively and the h coordinate measures the height of the point above the surface. Since the SCH coordinate system is not an orthogonal coordinate system, the vector subtraction in Eqn. [4.8] is not exact. However, since $\vec{T}^{elev}$ and

$\vec{T}^{ref}$ are very similar, a direct-subtraction approximation works reasonably well and is sufficient for the present analysis.

The noise in the DEM enters though the term $\vec{T}^{elev}$, the target position on the surface, which depends on both the imaging geometry and topography. Letting Δz be the error in the DEM, and $\Delta\vec{T}^{elev}$ the error in the position vector, then the corresponding error in the computed phase is:

$$\frac{\lambda}{4\pi}\Delta\phi_{topo} = \frac{1}{\rho}\sum_{i=s,c,h}\Delta\vec{T}_i^{elev}B_i \tag{4.9}$$

where

$$\begin{aligned}\Delta\vec{T}_s^{elev} &= 0\\ \Delta\vec{T}_c^{elev} &= \Delta z/tan(\theta)\\ \Delta\vec{T}_h^{elev} &= \Delta z;\end{aligned} \tag{4.10}$$

and θ is the incidence angle of the radar wave. Combining Eqn. [4.9] and Eqn. [4.10], we can write $\Delta\phi_{topo}$ in terms of Δz

$$\frac{\lambda}{4\pi}\Delta\phi_{topo} = \frac{\Delta z}{\rho}(\frac{B_c}{tan(\theta)} + B_h) \tag{4.11}$$

The baseline $B = \sqrt{B_s^2 + B_c^2 + B_h^2}$. Since B_s is typically much smaller than B_c and B_h, we can approximate B as

$$B = \begin{cases}\sqrt{2}B_c \approx \sqrt{2}B_h & B_c \approx B_h\\ B_c & B_c >> B_h\\ B_h & B_c << B_h\end{cases} \tag{4.12}$$

Combining Eqn. [4.11] and Eqn. [4.12], $\Delta\phi_{topo}$ as a function of DEM error Δz and the baseline B becomes

$$\frac{\lambda}{4\pi}\Delta\phi_{topo} = \begin{cases} \frac{1}{\sqrt{2}\rho}(\frac{1}{tan(\theta)}+1)B\Delta z & B_c \approx B_h \\ \frac{1}{\rho}\frac{1}{tan(\theta)}B\Delta z & B_c >> B_h \\ \frac{1}{\rho}B\Delta z & B_c << B_h \end{cases} \tag{4.13}$$

For spaceborne satellite geometries, the three conditions in eqn.(4.13) are all possible. Since the first, B_cB_h, typically yields the largest estimation errors, we use the following

$$\frac{\lambda}{4\pi}\Delta\phi_{topo} = \frac{1}{\sqrt{2}\rho}(\frac{1}{tan(\theta)}+1)B\Delta z) \tag{4.14}$$

to bound the uncertainty in interferometric phase introduced by DEM error.

Note that the right hand side of Eqn. [4.14] does not depend on wavelength, and the left hand side of Eqn. [4.14] is the uncertainty in estimated LOS surface deformation caused by DEM error. The deformation uncertainty is proportional to DEM error with a scale solely determined by imaging geometry – the larger the baseline B, the more sensitive the system is to DEM error. Fig. 4.9 illustrates the dependence of deformation uncertainty on both DEM error and baseline in the COSMO-SkyMed case. For our application to the Central Valley of California, we used SLC pairs with baseline smaller than 100 m. Since DEM error Δz is typically smaller than 3 m for flat areas like the Central Valley, the error introduced by DEM error in our derived surface deformation is less than 0.1 cm. As shown in Fig. 4.9, for SLC pairs with baselines smaller than 1000 m we obtain cm-level accurate surface displacement given no other significant error sources are present. In the Hawaii case, the DEM error is about 7 – 10 m and we used SLC pairs with baseline smaller than 500m. The ALOS satellite has a greater range and slightly larger look angle than COSMO-SkyMed

satellite, and as a result, a smaller multiplier on DEM error. In this case, the uncertainty level in our final estimation is about 1 cm. Since the observed deformation is about 50 – 70 cm, the effects of DEM error can be safely ignored. Both cases have shown that with some knowledge of the DEM error level in the study region, we can use Fig. 4.9 or Eqn. [4.14] to find an upper bound for baseline in order to choose SLC pair selections. For example, for the COSMO-SkyMed case, the maximum baseline we can use is about 600 m if the uncertainty caused by DEM error need be under 0.5 cm.

4.4 Implementation with Sentinel-1 Data

In this section, we show an example of how we implemented the idea of topography corrected and geocoded SAR on Sentinel-1 data over the Cascadia region. Because Sentinel-1 operates on the TOPSAR imaging mode, which requires extra precision on image co-registration, and because orbit data of Sentinel-1 is highly accurate, we choose to not implement motion compensation techniques but rather resample Sentinel-1 SLC images directly onto a latitude-longitude grid of a desired resolution and correct topography-related phase with an external DEM at the same time. This again shows that motion-compensation is not a prerequisite for the proposed workflow.

Fig. 4.10 illustrates an example of one such processed Sentinel-1 SAR amplitude image of the Cascadia region using the proposed workflow. To form the presented topography corrected and geocoded SAR image, we combined five consecutive frames. The combining process is easy because each frame has already been resampled onto the common latitude-longitude grid. With topography-corrected and geocoded SAR

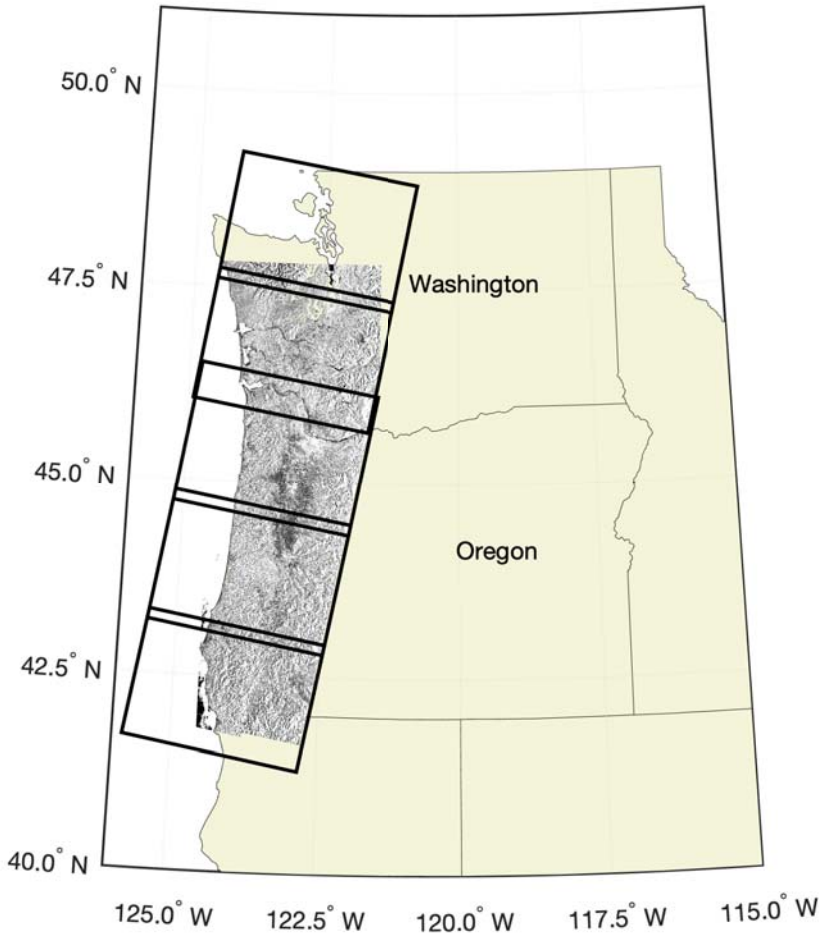

Figure 4.10: Example of processing Sentinel-1 data with the proposed workflow. We process five consecutive frames of Sentinel-1 scenes (rectangles) into one topography-corrected and geocoded SAR image, shown as a gray-scale amplitude image.

images in well defined latitude-longitude grid ready for use, further processing becomes much more efficient and friendlier than it would have been with thousands of interferograms in need of topography correction and geocoding.

4.5 Conclusions

In this chapter we have described a new InSAR processing approaches that generate products meeting the needs of a wider than traditional InSAR user community, are both efficient and robust, and are especially useful for time-series analysis that requires a large number of SAR acquisitions. These goals are reached by altering the data flow such that detailed and needed phase corrections are done by experts at the data provider level, relieving users of the need to attain a high degree level of specialization in InSAR proficiency and of the need for vast amounts of compute resources. We further quantify a major error source, phase errors due to imperfections in the digital elevation model of an area, showing that deformation artifacts grow linearly with DEM errors and InSAR baseline. For regions with poor DEMs, sufficiently accurate estimation of LOS deformation can yet be achieved with SLC pairs that have small baselines.

Current imaging radar satellites acquire SAR data for almost every point on Earth at least once every six days (*Hooper et al.*, 2012). Currently planned radar satellites, including the SAOCOM L-band system, Radarsat constellation, and the upcoming NASA-ISRO SAR mission will provide additional rich sources of high quality interferometric data. While the wide coverage of current and future SAR missions in both space and time will open up the possibility of using InSAR for near real-time monitoring, the high rates and large volumes of data still pose challenges to existing

InSAR processing algorithms. The work presented here will significantly improve the efficiency of interferogram formation when analyzing a large stack of SAR acquisitions.

In addition to separating InSAR product processing from many InSAR applications – the former requires knowledge of detailed SAR acquisition geometries and complicated InSAR processing techniques, and the latter is mostly about geophysical modeling – enhanced computational efficiency results from our new processing approach. The separated InSAR processing approach delivers compensated SLC images that simply need to be cross-multiplied to yield products that can be readily used in the geophysical modeling. If InSAR data users can acquire these compensated SLC products from data providers, the use of InSAR data for geophysical applications can become much simpler and easier than it is today.

Chapter 5

Noise Reduction in Interferogram Stacks

The ability of InSAR to observe small signals is often limited by atmospheric noise and decorrelation. With the quantity and quality of data modern InSAR networks offer, it is now possible to reduce noise sufficiently to observe very small ($\sim mm$) signals in noisy environments. In order to quantify uncertainties associated with the retrieved signals, a temporal noise covariance model must keep track of both atmospheric noise propagation and decorrelation noise propagation in time-series techniques such as stacking or Small BAseline Subset (SBAS) method (*Berardino et al.*, 2002). Atmospheric noise is correlated between interferograms with common acquisition dates (*Zebker et al.*, 1997) and by stacking independent interferograms (i.e., interferograms that do not share common acquisition dates), atmospheric noise can be most effectively reduced (*Emardson et al.*, 2003). Decorrelation noise, on the other hand, has been largely ignored in the noise covariance models. In the simple mathematical framework developed by *Hanssen* (2001) to describe common noise sources in InSAR, decorrelation noise is modeled as an independent noise term, uncorrelated between any interferograms. *Agram and Simons* (2015) show that decorrelation noise can be

temporally correlated and propose a covariance model to account for the contribution of decorrelation noise to overall noise covariance. However, to the best of our knowledge, neither of these decorrelation covariance models has been tested against real data.

In this chapter, we discuss how stochastic noise such as atmospheric noise and decorrelation noise propagate through interferogram stacks. We first briefly introduce different stacking strategies. We then introduce the covariance model for atmospheric noise. The form of atmospheric noise covariance model is relatively well understood (*Zebker et al.*, 1997; *Emardson et al.*, 2003). Here we present a practical way to estimate the atmospheric noise covariance matrix for interferogram stacks. We then present a new covariance model for decorrelation noise based on surface scattering properties and validate our model against real data collected in both low coherence and mid-to-high coherence areas. Our proposed decorrelation covariance model suggests that decorrelation noise is indeed correlated between interferograms, but the degree of correlation is overestimated by the model developed in *Agram and Simons* (2015) for rapidly decorrelating surfaces. We show that while independent interferogram stacking is effective in terms of atmospheric noise mitigation, a significant reduction in decorrelation noise can be achieved by including redundant interferograms in a stack. Finally, We discuss how different stacking strategies impact noise reduction. In particular, we show that for rapidly decorrelating surfaces such as the Cascadia region, including redundant interferograms in stacks reduces phase variance by more than 80%.

5.1 Stacking: Different Strategies

Stacking refers to the process whereby multiple interferograms are averaged to mitigate temporally uncorrelated or weakly-correlated noise. To achieve different goals, there are different stacking strategies. For example, to solve for a constant deformation rate, such as inter-SSE velocity, weighted stacking is often adopted to account for varying signal strength in different interferograms. On the other hand, if a constant signal strength is expected in every interferogram, then an equal weight should be applied to all interferograms.

In this chapter, we discuss both independent interferogram stacking and redundant interferogram stacking (referred to as independent and redundant stacking in the rest of the chapter) as they prove to make a difference in terms of decorrelation noise reduction. Fig. 5.1 illustrates these two stacking strategies. Assume that we have four consecutive radar measurements s_1, s_2, s_3, and s_4 over the same target x and between the measurement times of s_2 and s_3, the target x went through deformation. An independent stack over the deformation period yields

$$\phi_{ind} = \frac{1}{2}(\phi_{13} + \phi_{24}) \tag{5.1}$$

where ϕ_{ij} represents the unwrapped phase of the interferometric measurement $s_i s_j^*$. By convention, we have $i < j$ in this thesis. ϕ_{14} and ϕ_{23} are not used in Eqn. [5.1] as they are "redundant interferograms" formed using the same set of radar measurements. A redundant stack, as we define here, includes all available interferograms where each radar measurement is used the same number of times:

$$\phi_{red} = \frac{1}{4}(\phi_{13} + \phi_{24} + \phi_{14} + \phi_{23}) \tag{5.2}$$

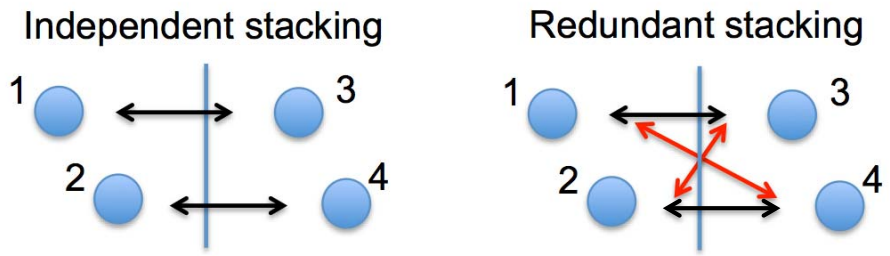

Figure 5.1: Independent and redundant interferogram stacking. Each number represents one image acquisition, and these acquisitions are arranged left and right in each panel according to acquisition time. Left, an independent stack consists of interferograms that do not share any common acquisition dates. Right, a redundant stack consists of all available interferograms where each acquisition date appears the same number of times.

5.2 Atmospheric Noise Reduction by Stacking

Atmospheric noise is a result of the spatiotemporal heterogeneity of water vapor content in the lower atmosphere causing variance in time delays of the radar signal as it propagates through the atmosphere (*Goldstein*, 1995; *Zebker et al.*, 1997; *Emardson et al.*, 2003).

Assuming that the average variance of atmospheric delay at acquisition time i with respect to a reference point is σ_i^2, which depends on the distance and height difference between the target x and some reference point, the covariance of ϕ_{ij}^{atm} and ϕ_{kl}^{atm} is (*Emardson et al.*, 2003; *Onn and Zebker*, 2006)

$$cov(\phi_{ij}^{atm}, \phi_{kl}^{atm}) = \sigma_i^2(\delta_{ik} + \delta_{il}) + {\sigma_j}^2(\delta_{jk} + \delta_{jl}) \tag{5.3}$$

where $\delta_{ij} = 1$, if $i = j$, and $\delta_{ij} = 0$ if otherwise.

5.2.1 Atmospheric Noise Covariance Matrix Estimation

In order to estimate the covariance matrix, we need to first estimate the atmospheric variance σ_i^2 associated with radar measurements at time t_i. In practice, direct estimation of σ_i from radar measurements is not straightforward without other facilitating data sources (e.g., GPS data, meteorologic data). On the other hand, statistical properties of atmospheric noise in the interferometric measurements ϕ_{ij}^{atm} have been studied extensively (e.g. *Emardson et al.*, 2003; *Onn and Zebker*, 2006; *Treuhaft and Lanyi*, 1987). *Emardson et al.* (2003) shows that the standard deviation of interferometric atmospheric noise exhibits a power-law relation with length:

$$\sigma_{ij}^{atm} = \sigma(\phi_{ij}^{atm,x} - \phi_{ij}^{atm,y}) = c_{ij} L^{\alpha_{ij}} \tag{5.4}$$

Here we use σ_{ij}^{atm} to denote interferometric atmospheric noise as apposed to atmospheric noise at acquisition time i σ_i. Typically in Eqn. [5.4], σ_{ij} is in mm and L is the distance between pixel x and pixel y and is in km. The value of α determines the power-law behavior and is expected to be largely site-invariant. We expect Eqn. 5.4 to be valid for distances between 10 km and 800 km. *Emardson et al.* (2003) reports a value of α to be around 0.5 based on GPS data collected in Southern California. The value of c, on the other hand, is expected to vary site to site because it describes the variability of water vapor content in the lower troposphere.

We can estimate the parameters α_{ij} and c_{ij} for every interferogram in the stack. Fig. 5.2 demonstrates an example of such power-law behavior exhibited by atmospheric noise in interferometric measurements collected between Oct 7, 2016 and Oct

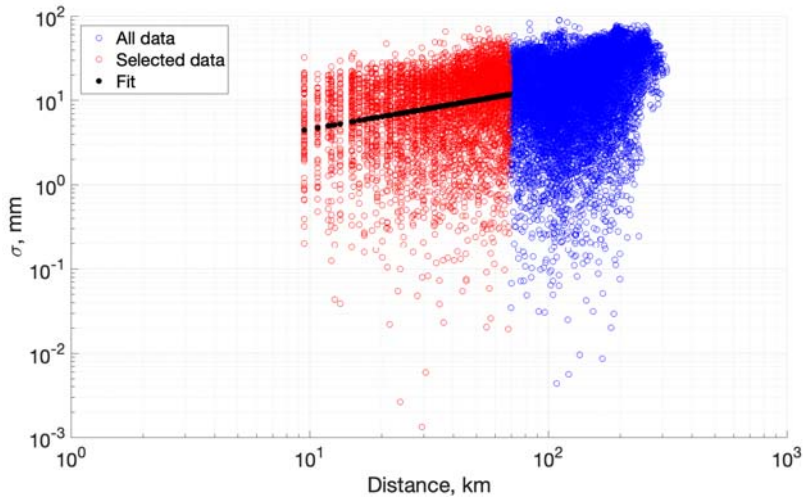

Figure 5.2: Atmospheric standard deviation σ as a function of distance estimated from the interferometric measurements between Oct 7, 2016 and Oct 8, 2017. Both blue and red circles represent estimated atmospheric standard deviation in mm extracted from the interferometric measurements. The red circles are selected data points used for parameter estimation. The black circles show the fit to the data. The final estimated function is $\sigma = 1.5 * L^{0.5}$.

8, 2017 over Cascadia. We extracted the atmospheric variance from interferometric measurements by computing the square of phase differences at different length scales. To minimize the impact of decorrelation, only pixels with correlation above 0.3 were used in the computation. Because there are many fewer data points with long distance separation than short distance separation, we only use data points that are separated by a distance less than roughly half the image size to solve for the desired parameters. We find $\alpha = 0.5$ and $c = 1.5$ for this interferogram. In general, we find α ranging from 0.39 to 0.69 in Cascadia, consistent with the value of 0.5 reported by *Emardson et al.* (2003). We find c mostly varies from 0.51 to 1.85, as opposed to the value of 2.5 reported in *Emardson et al.* (2003) for Southern California.

With c_{ij} and α_{ij} estimated for every interferogram, we can calculate, for every pixel, an interferometric atmospheric standard deviation with respect to a reference

pixel: $\sigma_{(i,j)} = \sigma(\phi_{ij}^{atm} - \phi_{ij}^{atm,r}) = c_{ij}L^{\alpha_{ij}}$. Interferometric atmospheric variances ${\sigma_{ij}^{atm}}^2$ are the sum of atmospheric variances at acquisition times i and j:

$$ {\sigma_{ij}^{atm}}^2 = \sigma_i^2 + \sigma_j^2. \tag{5.5} $$

We can rewrite the relation in the following matrix representation:

$$ \boldsymbol{B\sigma^2} = \boldsymbol{\sigma_I^2} \tag{5.6} $$

where $\boldsymbol{\sigma_I^2}$ represents a list of interferometric variance at pixel x in different interferograms, $\boldsymbol{\sigma^2}$ represents the list of atmospheric noise variance associated with radar measurements at different acquisition times. $\boldsymbol{B}$ is an incidence matrix that links the atmospheric noise variance in different acquisitions to the interferometric measurements. For example, with $\boldsymbol{\sigma^2} = [\sigma_1^2, \sigma_2^2, \sigma_3^2]$, $\boldsymbol{\sigma_I^2} = [{\sigma_{12}^{atm}}^2, {\sigma_{13}^{atm}}^2]$,

$$ B = \begin{bmatrix} 1 & 1 & 0 \\ 1 & 0 & 1 \end{bmatrix}. \tag{5.7} $$

After obtaining an estimate of $\boldsymbol{\sigma^2}$ by inverting Eqn. [5.6] with non-negativity constraints, we can form the covariance matrix of atmospheric noise using Eqn. [5.4]. Note this method is only valid when the power-law behavior of interferometric atmospheric noise is valid, namely, the maximum distance of the analyzed datasets is 800 km.

5.2.2 Independent vs Redundant Stacking

Assume that we have four interferometric measurements as illustrated in Fig. 5.1. The covariance matrices for $\Phi_{ind}^{atm} = [\phi_{13}^{atm}, \phi_{24}^{atm}]$ and $\Phi_{red}^{atm} = [\phi_{13}^{atm}, \phi_{24}^{atm}, \phi_{14}^{atm}, \phi_{23}^{atm}]$

can be constructed as follows:

$$COV_{\Phi_{ind}^{atm}} = \begin{bmatrix} \sigma_1^2 + \sigma_3^2 & 0 \\ 0 & \sigma_2^2 + \sigma_4^2 \end{bmatrix} \tag{5.8}$$

$$COV_{\Phi_{red}^{atm}} = \begin{bmatrix} \sigma_1^2 + \sigma_3^2 & 0 & \sigma_1^2 & \sigma_3^2 \\ 0 & \sigma_2^2 + \sigma_4^2 & \sigma_4^2 & \sigma_2^2 \\ \sigma_1^2 & \sigma_4^2 & \sigma_1^2 + \sigma_4^2 & 0 \\ \sigma_3^2 & \sigma_2^2 & 0 & \sigma_2^2 + \sigma_3^2 \end{bmatrix} \tag{5.9}$$

It can be easily shown that $\sigma^2(\phi_{ind}^{atm}) = \sigma^2(\phi_{red}^{atm}) = (\sigma_1^2 + \sigma_2^2 + \sigma_3^2 + \sigma_4^2)/4$. Therefore, both independent and redundant stacking statistically reduce the variance associated with atmospheric noise by a factor equal to the number of radar measurements.

5.2.3 Weighted vs Non-Weighted Stacking

Weighted stacking effectively changes each element of the covariance matrix from

$$cov(\phi_{ij}^{atm}, \phi_{kl}^{atm})$$

to

$$w_{ij} w_{kl}\, cov(\phi_{ij}^{atm}, \phi_{kl}^{atm}).$$

Therefore, when reducing atmospheric noise, or in fact, any stochastic noise component that can be described with a covariance matrix, it is important to keep in mind that data with higher weights will have greater variance and covariance in the noise covariance matrix as well. Sometimes, it may be strategic to discard these data even though this may mean losing independent measurements.

5.3 Decorrelation Noise Reduction by Stacking

Decorrelation is one of the main limiting factors for InSAR observations. The mechanisms of signal deorrelation have been well studied, and can mainly be attributed to changes of surface scattering properties during the observation time span, geometrical decorrelation, and system and other thermal noises (*Zebker and Villasenor*, 1992).

A covariance model for decorrelation noise is often ignored because (1) conventional InSAR time-series techniques such as Persistent Scattering (*Ferretti et al.*, 2001; *Hooper et al.*, 2004) and Small BAseline Subset (*Berardino et al.*, 2002) techniques typically only deal with observations with relatively high coherence and (2) extensive spatial filtering before analysis often permits sufficient reduction of decorrelation noise for mid-to-high coherence areas. However, with modern large InSAR datasets and the desire to resolve small amplitude signals in low coherence areas, a covariance model for decorrelation noise is needed to account for associated uncertainties in time-series analyses. A covariance model for decorrelation noise can also help us determine best time-series practice to reduce decorrelation noise.

As stated above, *Hanssen* (2001) models decorrelation as a fully independent noise term in each interferogram in a network. Letting σ_{ij}^2 denote the variance associated with ϕ_{ij}^{decor}, the covariance of ϕ_{ij}^{decor} and ϕ_{kl}^{decor} given by *Hanssen* (2001) is

$$cov(\phi_{ij}^{decor}, \phi_{kl}^{decor}) = \sigma_{ij}^2 \delta_{ik} \delta_{jl} \tag{5.10}$$

where $\delta_{ij} = 1$, if $i = j$, and $\delta_{ij} = 0$ if otherwise. Therefore, the covariance matrix given by *Hanssen* (2001) only has diagonal components, which are simply the variance associated with ϕ_{ij}^{decor}.

In contrast, *Agram and Simons* (2015) argue that decorrelation noise is correlated in time. Therefore, interferograms that share a common time interval can have nonzero correlations between their respective decorrelation noise terms. Their proposed method to obtain the covariance matrix starts with a pseudocovariance matrix $\tilde{\Omega}_{ifg}$ that is derived from a SAR coherence matrix Ω_{sar} and the InSAR incidence matrix A (Definition of A can be found in *Berardino et al.* (2002)): $\tilde{\Omega}_{ifg} = \frac{1}{2} A \Omega_{sar} A^T$. The pseudocovariance of ϕ_{ij}^{decor} and ϕ_{kl}^{decor} is then expressed as

$$\widetilde{cov}(\phi_{ij}^{decor}, \phi_{kl}^{decor}) = \frac{\rho_{ik} + \rho_{jl} - \rho_{il} - \rho_{jk}}{2} \tag{5.11}$$

where ρ_{ij} is the correlation coefficient between radar measurements s_i and s_j. The pseudocovariance is then used to approximate the true covariance of of ϕ_{ij}^{decor} and ϕ_{kl}^{decor}:

$$cov(\phi_{ij}^{decor}, \phi_{kl}^{decor}) = \frac{\sigma_{ij}}{\sqrt{1-\rho_{ij}}} \cdot \widetilde{cov}(\phi_{ij}^{decor}, \phi_{kl}^{decor}) \cdot \frac{\sigma_{kl}}{\sqrt{1-\rho_{kl}}} \tag{5.12}$$

where the scaling factor $\sigma_{ij}/\sqrt{1-\rho_{ij}}$ implies that $cov(\phi_{ij}^{decor}, \phi_{ij}^{decor}) = var(\phi_{ij}^{decor}) = \sigma_{ij}^2$. Therefore, the covariance matrix given by *Agram and Simons* (2015) not only has diagonal components, but also has nonzero off-diagonal components. We note that this scaling is not quite right, see section 5.3.1 below.

The models of *Hanssen* (2001) and *Agram and Simons* (2015) differ in whether or not decorrelation noise is itself correlated between interferograms. Hence, the two models give different predictions for the reduction of decorrelation noise by redundant and independent interferogram stacking. For example, suppose we have an interferogram network consisting of interferograms with similar correlation and noise level. *Hanssen* (2001) predicts that redundant interferogram stacking reduces decorrelation more effectively than independent interferogram stacking; *Agram and Simons* (2015), on the other hand, predict the same performance from either of the two stacking

strategies. For ease of discussion, hereinafter we refer to the covariance model suggested by *Hanssen* (2001) as the "Hanssen model" and the covariance model suggested by *Agram and Simons* (2015) as the "Agram-Simons model".

As we will demonstrate in the following section, neither of these models fit actual data well. We propose a decorrelation noise covariance model based on scattering properties of the surface. We argue that while decorrelation noise is correlated between interferograms rather than being independent as proposed by *Hanssen* (2001), the extent of the correlation is not precisely captured by *Agram and Simons* (2015). We show that redundant stacking reduces decorrelation noise more effectively than independent stacking, especially in low coherence areas such as the Cascadia region.

5.3.1 A New Decorrelation Covariance Model

In this section, we present a covariance model for decorrelation phase noise. Let us first take a look at how the correlation coefficient ρ varies with time t. We can write $\rho(t)$ as the sum of two parts:

$$\rho(t) = \rho_\infty + (1 - \rho_\infty)e^{-\frac{t}{\tau}} \tag{5.13}$$

The second term of Eqn. [5.13] represents the classic exponential decay model assuming random Gaussian motion among scatterers (*Zebker and Villasenor*, 1992). The first term of Eqn. [5.13] acknowledges the contribution from persistent scatterers. When $t \to 0$, $\rho \to 1$, and when $t \to \infty$, $\rho \to \rho_\infty$. τ represents the characteristic decorrelation time and varies with wavelength and surface scattering properties. Fig. 5.3 plots of observed correlation of pixels for different interferogram time spans, shows how ρ, at C band as observed by Sentinel-1, decreases with time in two areas – the

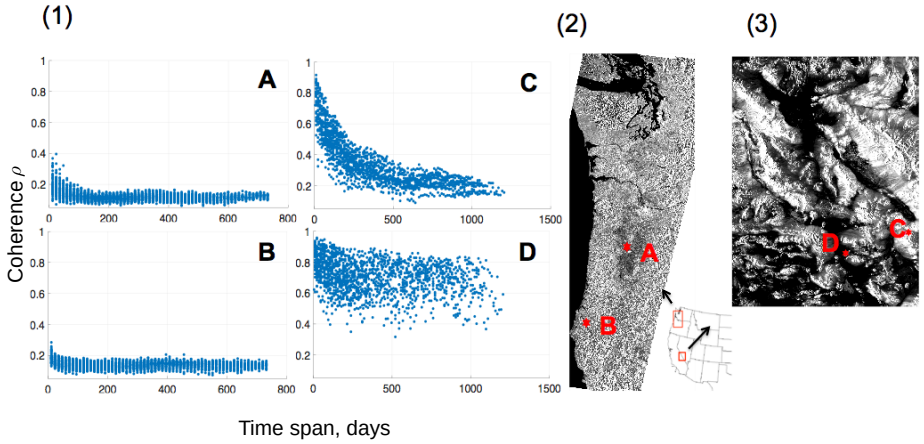

Figure 5.3: Examples of temporal variations of correlation in the Cascadia and the Death Valley regions. (1) Scatter plots of correlation vs time in locations A, B, C and D. (2) A and B are located in heavily vegetated Cascadia region, (3) C and D are located in the desert of Death Valley. A and B both exhibit a characteristic decorrelation time of roughly 30 days and an asymptotic coherence ρ_∞ of 0.1. C and D, on the other hand, show much longer decorrelation time of approximately 400 days and 200 days and higher asymptotic coherence ρ_∞ of 0.2 and 0.6, respectively.

heavily vegetated Cascadia region, and the desert Death Valley area. It is apparent that for heavily vegetated areas, the characteristic decorrelation time τ is about 30 to 40 days, much shorter than the desert areas, for which τ can be as long as a few years. The Death Valley data also exhibit larger contributions from persistent scatterers: ρ_∞ in the two locations shown in the death valley are 0.2 and 0.6, respectively, much higher than $\rho_\infty \approx 0.1$ in the two locations shown in the Cascadia region.

Next, consider a series of radar signals $s_1, s_2, ...s_n$ acquired at different time observing the same target. We adopt the style of analysis presented in *Zebker and Villasenor* (1992):

$$s_i = (\sqrt{\rho_\infty}C + \sqrt{1-\rho_\infty}D_i)e^{i\psi_i} \tag{5.14}$$

where ψ_i represents propagation phases (e.g., deformation signal, atmospheric delay) at time t_i, C represents a persistent scatterer that remains coherent, and D_i represents

distributed scatterers at time t_i that decorrelate gradually over time. For the sake of simplicity and without loss of generality, we make $C = 1$, $E[D_i] = 0$ and $E[|D_i|^2] = 1$, so that the expected intensity of s_i is unity. We model the distributed scatterers D_i as complex Gaussian random variables. D_i's can be represented as

$$D_i = \rho^d_{i-1,i} D_{i-1} + \sqrt{1 - {\rho^d_{i-1,i}}^2}\, n_i \tag{5.15}$$

where n_i is a complex Gaussian random variable with an expected intensity of unity, and that is uncorrelated with D's and n_j as long as $i \neq j$.

With Eqn. [5.15], we can derive that

$$D_i {D_j}^* = \rho^d_{ij} + R_{ij} \tag{5.16}$$

$$E[D_i {D_j}^*] = \rho^d_{ij} \tag{5.17}$$

$$\rho^d_{ij}\rho^d_{jk} = \rho^d_{ik} \tag{5.18}$$

$$E(|D_i|^2 |D_j|^2) = 1 + {\rho^d_{ij}}^2 \tag{5.19}$$

where ρ^d_{ij} describes the correlation between distributed scatterers D at times t_i and t_j and is often modeled as a decaying exponential function of time. R_{ij} describes the remaining part of $D_i {D_j}^*$ and has an expected value of zero. Let z_{ij} represent the interferometric measurement between signals s_i and s_j:

$$z_{ij} = s_i {s_j}^* = \left(\rho_\infty + (1-\rho_\infty) D_i {D_j}^* + \sqrt{\rho_\infty(1-\rho_\infty)}(D_i + {D_j}^*)\right) e^{i(\psi_i - \psi_j)}. \tag{5.20}$$

The correlation ρ_{ij} between signals s_i and s_j is

$$\rho_{ij} = \frac{\left|E[z_{ij}]\right|}{\sqrt{E[|s_i|^2]E[|s_j|^2]}} = \rho_\infty + (1-\rho_\infty)\rho^d_{ij}. \tag{5.21}$$

With an exponential decay model $\rho_{ij}^{d} = exp\big(-|t_i - t_j|/\tau\big)$, Eqn. [5.21] is consistent with Eqn. [5.13]. Substituting Eqn.[5.16] and [5.21] into [5.20],

$$z_{ij} = \Bigg(\rho_{ij} + (1-\rho_\infty)R_{ij} + \sqrt{\rho_\infty(1-\rho_\infty)}(D_i + {D_j}^*)\Bigg)e^{i(\psi_i - \psi_j)} \tag{5.22}$$

The first term of Eqn. [5.22] represents coherent signals between time t_i and t_j, which is the expected value of z_{ij}, the second and third terms are associated with decorrelation noise during this time period:

$$z_{ij} - E[z_{ij}] = \Bigg((1-\rho_\infty)R_{ij} + \sqrt{\rho_\infty(1-\rho_\infty)}(D_i + {D_j}^*)\Bigg)e^{i(\psi_i - \psi_j)} \tag{5.23}$$

where $z_{ij} - E[z_{ij}]$ represents the zero-mean decorrelation noise component in the interferometric measurement z_{ij}. Making use of Eqn. [5.16] to Eqn. [5.19], the covariance of the decorrelation noise components in z_{ij} and z_{kl} is then

$$\begin{aligned}
&cov\,(z_{ij} - E[z_{ij}], z_{kl} - E[z_{kl}]) \qquad (5.24)\\
&\quad = E\big[(z_{ij} - E[z_{ij}])(z_{kl} - E[z_{kl}])^*\big]\\
&\quad = E\Bigg\{(1-\rho_\infty)^2 R_{ij}R_{kl}^* + \rho_\infty(1-\rho_\infty)(D_iD_k^* + D_iD_l + D_j^*D_k^* + D_j^*D_l) +\\
&\qquad\quad (1-\rho_\infty)\sqrt{\rho_\infty(1-\rho_\infty)}\big(R_{ij}(D_k^* + D_l) + R_{kl}^*(D_i + D_j^*)\big)\Bigg\}e^{i(\psi_i - \psi_j - \psi_k + \psi_l)}\\
&\quad = \Bigg((1-\rho_\infty)^2 E(R_{ij}R_{kl}^*) + \rho_\infty(1-\rho_\infty)(\rho_{ik}^d + \rho_{jl}^d)\Bigg)e^{i(\psi_i - \psi_j - \psi_k + \psi_l)}\\
&\quad = \Bigg((1-\rho_\infty)^2 \rho_{ik}^d\rho_{jl}^d + \rho_\infty(1-\rho_\infty)(\rho_{ik}^d + \rho_{jl}^d)\Bigg)e^{i(\psi_i - \psi_j - \psi_k + \psi_l)}\\
&\quad = (\rho_{ik}\rho_{jl} - \rho_\infty^2)e^{i(\psi_i - \psi_j - \psi_k + \psi_l)}
\end{aligned}$$

Similar to the definition of the correlation coefficient ρ between radar measurements, we define γ as the correlation coefficient between interferometric measurements:

$$\gamma(z_{ij}, z_{kl}) = \frac{\left|cov\ (z_{ij}, z_{kl})\right|}{\sqrt{E\left[|z_{ij} - E[z_{ij}]|^2\right] E\left[|z_{kl} - E[z_{kl}]|^2\right]}} \tag{5.25}$$

$$= \frac{\rho_{ik}\rho_{jl} - {\rho_\infty}^2}{1 - {\rho_\infty}^2} \tag{5.26}$$

γ ranges from 0 to 1.

To obtain the covariance between decorrelation phase $\phi_{ij}^{decor}, \phi_{kl}^{decor}$, we need $\gamma(\phi_{ij}^{decor}, \phi_{kl}^{decor})$

$$\gamma(\phi_{ij}^{decor}, \phi_{kl}^{decor}) = \frac{cov\ (\phi_{ij}^{decor}, \phi_{kl}^{decor})}{\sqrt{E|\phi_{ij}^{decor}|^2 |E|\phi_{kl}^{decor}|^2}} \tag{5.27}$$

$$= \frac{cov\ (\phi_{ij}^{decor}, \phi_{kl}^{decor})}{\sigma_{ij}\sigma_{kl}} \tag{5.28}$$

where σ_{ij} is the standard deviation of decorrelation phase noise ϕ_{ij}^{decor}. We find via numerical simulation that the relation between $\gamma(\phi_{ij}^{decor}, \phi_{kl}^{decor})$ and $\gamma(z_{ij}, z_{kl})$ exhibits a power-law behavior

$$1 - \gamma(\phi_{ij}^{decor}, \phi_{kl}^{decor}) \approx \left[1 - \gamma(z_{ij}, z_{kl})\right]^{\frac{1}{2}} \tag{5.29}$$

Note the difference here with the assumption in the Agram-Simons model that correlations between phases are equal to correlations between their respective complex

signals. Combining Eqn. [5.26], [5.28] and [5.29], we have

$$cov\left(\phi_{ij}^{decor}, \phi_{kl}^{decor}\right) = \sigma_{ij} \cdot \left[1 - (1 - \gamma(z_{ij}, z_{kl}))^{\frac{1}{2}}\right] \cdot \sigma_{kl} \tag{5.30}$$

$$= \left(1 - \sqrt{\frac{1 - \rho_{ik}\rho_{jl}}{1 - \rho_{\infty}^{2}}}\right) \sigma_{ij}\sigma_{kl} \tag{5.31}$$

Note that since we need ρ_{ij} in the proposed covariance model (Eqn.[5.31]), this model is only practically applicable to multi-looked interferograms of which good estimates of correlation coefficients can be obtained. Since returns from different pixels are generally uncorrelated or only weakly correlated, the decorrelation covariance matrix shown in Eqn. [5.31] holds for multi-looked interferograms.

5.3.2 Comparison Between Existing and the Proposed Decorrelation Covariance Models

So far we have described both the existing (Eqn. [5.10] and [5.12]) and the proposed (Eqn. [5.31]) decorrelation covariance models. In this section, we illustrate their differences by testing these models on surfaces with varying decorrelation rates. Specifically, we compare their respective performance prediction in terms of decorrelation noise reduction after both independent and redundant stacking. For ease of discussion, hereinafter we refer to the covariance model suggested by *Hanssen* (2001) as the "Hanssen model" and the covariance model suggested by *Agram and Simons* (2015) as the "Agram-Simons model".

Assume that we have $2M$ consecutive radar measurements acquired over the same target x. M measurements were acquired before the target x went through deformation, and M measurements were acquired afterwards. Using the independent and

redundant stacking strategies illustrated in Fig. 5.1, we can form an independent stack consisting of M interferometric measurements and a redundant stack consisting of M^2 interferometric measurements. For every interferometric measurement in the stack, there is an associated correlation coefficient ρ_{ij} and an associated phase noise $\sigma^2(\phi_{ij})$. ρ_{ij} is computed using Eqn. [5.13] with the asymptotic correlation ρ_∞ set to 0.1. The phase variance $\sigma^2(\phi_{ij})$ is computed using the Cramer-Rao bound relation $\sigma^2(\phi_{ij}) = \frac{1-\rho_{ij}^2}{2\rho_{ij}^2}$ (*Rodriguez and Martin*, 1992). Assuming no atmospheric noise is present, $\sigma^2(\phi_{ij})$ is hence equivalent to uncertainties associated with decorrelation noise $\sigma^2(\phi_{ij}^{decor})$.

Next we examine the associated uncertainties with ϕ_{ind}^{decor} and ϕ_{red}^{decor} with covariance models given in Eqn. [5.10], [5.12] and [5.31]. Consider two end-member cases: (1) $\tau \to 0$, so that every interferogram has a correlation coefficient $\rho_{ij} \to \rho_\infty$, and (2) $\tau \to \infty$, so that every interferogram has a correlation coefficient $\rho_{ij} \to 1$. We use $\bar{\sigma}_1^2$ and $\bar{\sigma}_2^2$ to represent the average phase noise in the stack for each case: $\bar{\sigma}_1^2 \approx \frac{1-\rho_\infty^2}{2\rho_\infty^2} > \bar{\sigma}_2^2 \approx 0$. The results are listed in Table. 5.1.

Table 5.1: Predicted Uncertainties After Stacking

Models	Stacking Strategy	Case 1: $\tau \to 0$	Case 2: $\tau \to \infty$
Hanssen	Independent	$\bar{\sigma}_1^2/M$	$\bar{\sigma}_2^2/M$
	Redundant	$\bar{\sigma}_1^2/M^2$	$\bar{\sigma}_2^2/M^2$
Agram-Simons	Independent	$\bar{\sigma}_1^2/M$	$(\frac{2}{3} + \frac{1}{3M^2})\bar{\sigma}_2^2$
	Redundant	$\bar{\sigma}_1^2/M$	$(\frac{2}{3} + \frac{1}{3M^2})\bar{\sigma}_2^2$
Proposed	Independent	$\bar{\sigma}_1^2/M$	$\bar{\sigma}_2^2$
	Redundant	$(\frac{1}{M} - \frac{M-1}{M^2}(\frac{2}{\sqrt{1+\rho_\infty}} - 1))\bar{\sigma}_1^2$	$\bar{\sigma}_2^2$

In both cases, the Hanssen Model predicts that redundant stacking produces smaller variance than independent stacking while the Agram-Simons model suggests

that redundant stacking yields the same results with independent stacking. In addition, the Agram-Simons model predicts higher phase variances than those predicted from the Hanssen model. This is because that the Agram-Simons model takes into account correlation between decorrelation components in interferometric measurements.

In the first case where the surface rapidly decorrelates, the proposed model predicts that redundant stacking yields smaller noise – with $\rho_\infty = 0.1$, redundant stacking reduces noise by about 90% over independent stacking. In the second case where almost no decorrelation takes place, the proposed model suggests that there is no reduction in noise by either stacking strategy, as all measurements are perfectly correlated. Therefore, with a long enough characteristic decorrelation time τ, we can infer that the proposed model suggests little to no difference between redundant stacking and independent stacking.

Fig. 5.4 depicts the predictions of $\sigma^2(\phi_{ind}^{decor})$ and $\sigma^2(\phi_{red}^{decor})$ from both the existing and the proposed models for surfaces with varying decorrelation rates (τ ranges from 1 to 500 days). M is set to 45, with each radar measurement taken 12 days apart. ρ_∞ is set to 0.1. As expected, the Hanssen model (green lines) predicts larger phase noise by independent stacking regardless of surface decorrelation rates; the Agram-Simons model (blue lines) predicts zero or small differences between the independent stack and the redundant stack with either rapidly or very slowly decorrelating surfaces; and the proposed model (red lines) predicts significant higher noise reduction from redundant stacking with rapidly decorrelating surfaces and similar noise reduction performances from either stacking strategy with slowly decorrelating surfaces. Additionally, we observe that:

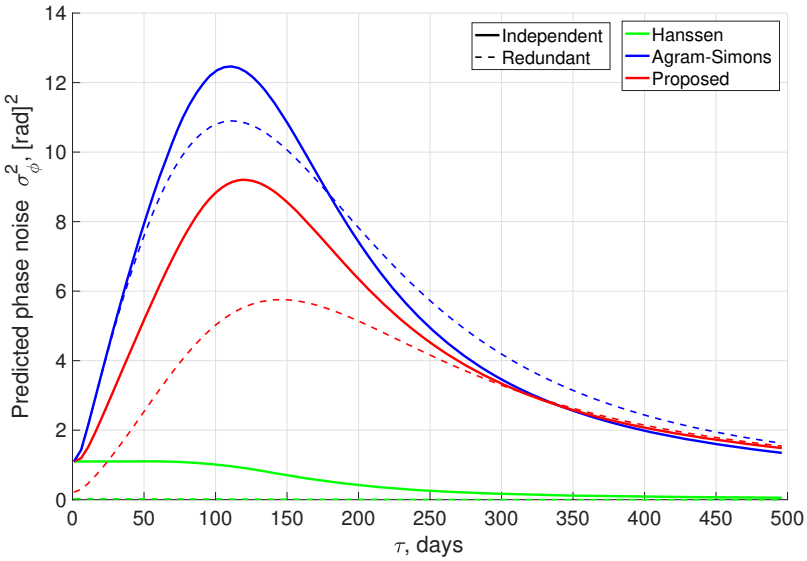

Figure 5.4: Predicted uncertainty associated with decorrelation noise after independent stacking and redundant stacking from decorrelation covariance models suggested by *Hanssen* (2001), *Agram and Simons* (2015) and the proposed model.

1. The Agram-Simons model predicts the highest phase noise (i.e., the least reduction in decorrelation noise) for both independent and redundant stacking. This means that the Agram-Simons model suggests high correlation between decorrelation noise components. In contrast, the Hanssen model, which assumes independence between decorrelation noise components, predicts the lowest uncertainty. Predictions from the proposed model fall between predictions from the other two models, suggesting that the proposed model assumes a weak correlation between decorrelation noise components (within the range of τ plotted in Fig.5.4).

2. Predictions from the proposed model and the Agram-Simons model show a peak around $\tau \approx 120$ days while predictions from the Hanssen model shows a steady decrease with increasing τ. Two factors influence the predicted phase variance: a) the average phase noise level in interferograms and b) the degree of correlation between

decorrelation noise components. The higher the average phase noise, the higher the predicted phase variance; the higher the degree of correlation between decorrelation noise terms, the higher the predicted phase variance. When τ is small, correlation between decorrelation noise terms is negligible in all three models, and when τ is large, the average phase noise level is low. Therefore the predicted phase variances from the proposed model and the Agram-Simons model are low at both ends of τ but high in the middle. Since there is no correlation in the Hanssen model, the predicted phase variance decreases monotonically with τ.

5.3.3 Validation With Real Data

In this section, we compare and assess all three decorrelation covariance models – the Hanssen model, the Agram-Simons model, and the proposed model – with Sentinel-1 data collected in both the Cascadia region and the Death Valley region.

The Cascadia region is heavily vegetated and hence shows fast decorrelation. The Death Valley region, on the other hand, is a desert and hence shows slow decorrelation (Fig. 5.3). For each region, we formed an independent interferogram stack and a redundant interferogram stack. The Cascadia region has an independent stack consisting of 40 interferograms and a redundant stack consisting of 1600 interferograms. The Death Valley region has an independent stack consisting of 28 interferograms and a redundant stack consisting of 784 interferograms. By averaging the respective stacks, we obtained ϕ_{ind} and ϕ_{red} for both regions.

Comparisons between phase variances associated with ϕ_{ind} and ϕ_{red} are shown in Fig. 5.5. We obtained $\sigma^2(\phi_{ind}^{decor})$ and $\sigma^2(\phi_{red}^{decor})$ at evenly distributed grid points by

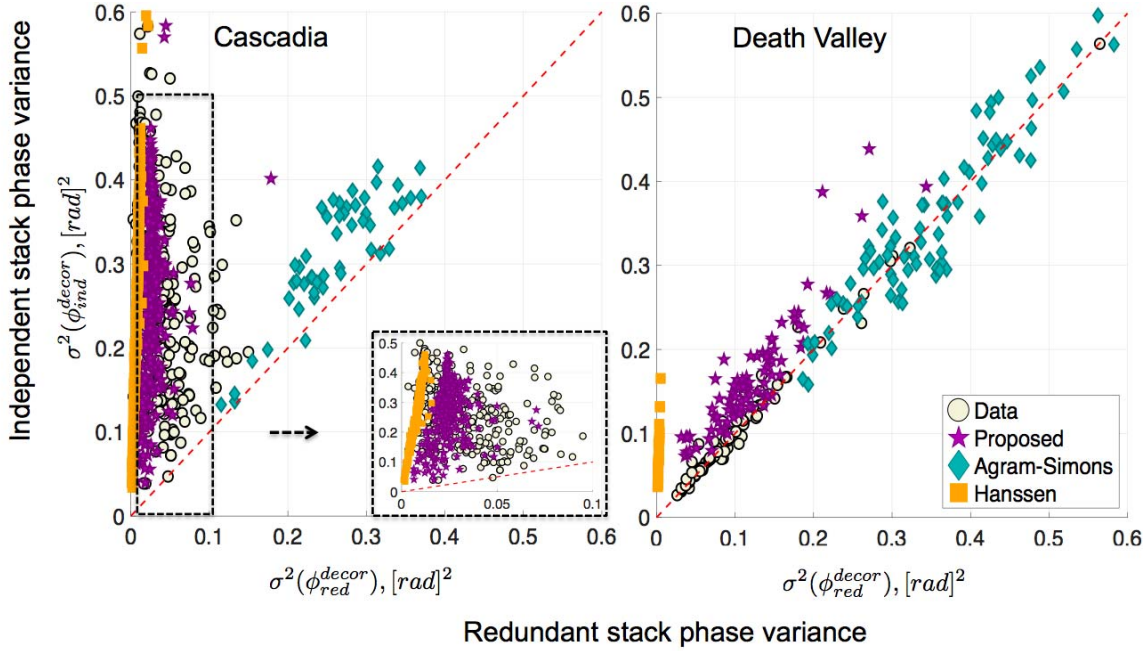

Figure 5.5: Phase variance after independent stacking vs phase variance after redundant stacking in (left) the Cascadia region and (right) the Death Valley region. Data (circles) show that for the Cascadia region, redundant stacking produces smaller phase variances and for the Death Valley region, similar phase variances compared to the independent stack. Predictions from the proposed model (stars) match the data best in both cases while the Hanssen model (squares) underestimates and the Agram-Simons model (diamonds) overestimates phase variance in both cases.

Table 5.2: Average Prediction Error. We define prediction errors as the distances (unit: $[rad]^2$) from the average position of data points (beige circles) and the average positions of their corresponding prediction points (purple stars, orange squares or cyan diamonds) in Fig. 5.5.

Models	Cascadia	Death Valley
Hanssen	0.030	0.108
Agram-Simons	0.274	0.365
Proposed	0.017	0.066

calculating phase variances inside 50 pixel by 50 pixel boxes (1500 meter by 1500 meter in area) centered at each location, assuming atmospheric noise is negligible inside the box. For the Cascadia region, the redundant stack yields smaller uncertainties than the independent stack (Fig. 5.5, left, beige circles), confirming predictions from the proposed model and suggesting that for rapidly decorrelating areas, redundant interferograms should be used in addition to independent interferograms to best reduce decorrelation. For the Death Valley region where the characteristic decorrelation time τ is on the order of years, independent and redundant stacking produce similar results (Fig. 5.5, right, beige circles), consistent with predictions from the proposed model.

With ρ_{ij} and the associated phase noise σ_{ij}^2 for each grid point in every interferogram in the stack, we can predict phase variances associated with ϕ_{ind} and ϕ_{red} using these three decorrelation covariance models. The predictions are shown in Fig. 5.5 and Table. 5.2. Predictions from the proposed model (purple stars) match best with actual observations (beige circles) while predictions from the Hanssen model (orange squares) mostly underestimates, and the Agram-Simons model (cyan diamonds) mostly overestimates phase variances of the stacks. The Hanssen model shows comparable average errors with the proposed model but it fails to capture the difference between the Cascadia region (rapidly decorrelating surfaces) and the Death Valley

region (slowly decorrelating surfaces), as it predicts that redundant stacking always produces smaller phase noise. The Agram-Simons model also fails to capture the difference between the Cascadia region and the Death Valley region, because it predicts the same phase noise after redundant stacking and independent stacking in both regions.

Finally, we use an example to illustrate the significant reduction in decorrelation noise by including redundant interferograms in the stack for rapidly decorrelating areas . Fig. 5.6 depicts stacking results over a slow slip event that occurred in February 2016 in the Cascadia region. Slow slip events are usually hard to capture in the Cascadia region with InSAR due to extremely low signal to noise ratios. Atmospheric noise and decorrelation are the two main limitation factors. With 10 Sentinel-1 SAR acquisitions before the slow slip event and 10 Sentinel-1 SAR acquisitions after, we formed an independent interferogram stack consisting of 10 interferograms and a redundant stack consisting of 100 interferograms. It is apparent that the result from using redundant stacking yields a much cleaner deformation pattern. Fig. 5.7 compares phase measurements along four profile lines between independent stacking and redundant stacking. Again, it is clear that while both stacking strategies produce measurements of the same expected signal, redundant stacking produces measurements with much smaller phase variance (about 80% less). With the same number of independent acquisitions, atmospheric noise is reduced to the same extent after either independent stacking or redundant stacking. Therefore, the significant reduction in phase noise reflects reduced decorrelation noise in the redundant stack.

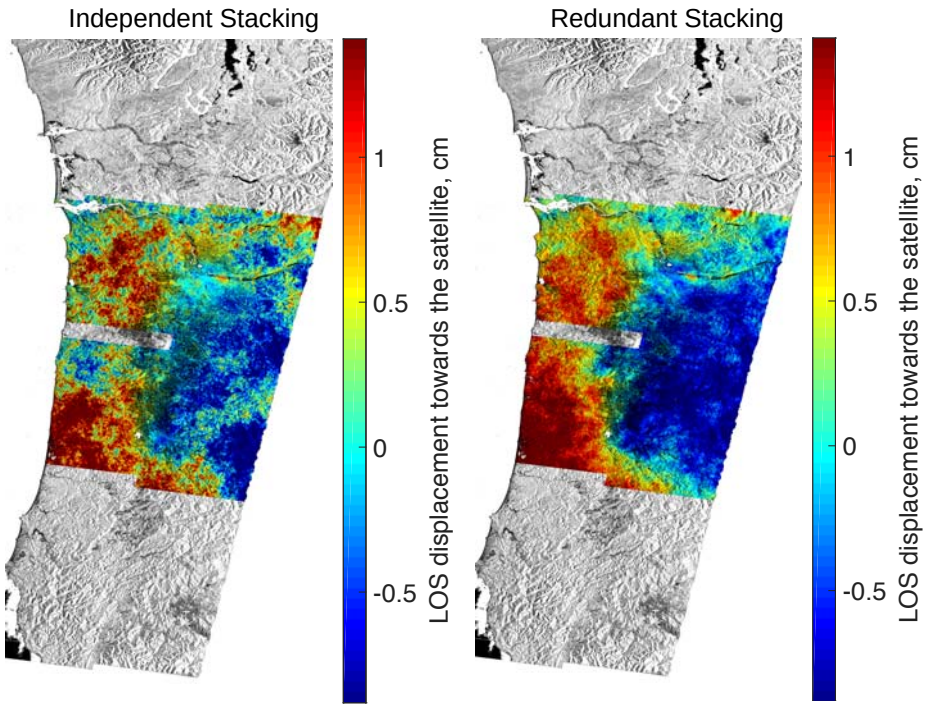

Figure 5.6: Results from (left) independent and (right) redundant stacking over the February 2016 slow slip event in the Cascadia region. The result from redundant stacking suffers from less decorrelation noise than the result from independent stacking. Areas with less coverage than 20 acquisitions are masked. Phase measurements are converted to radar line-of-sight (LOS) measurements.

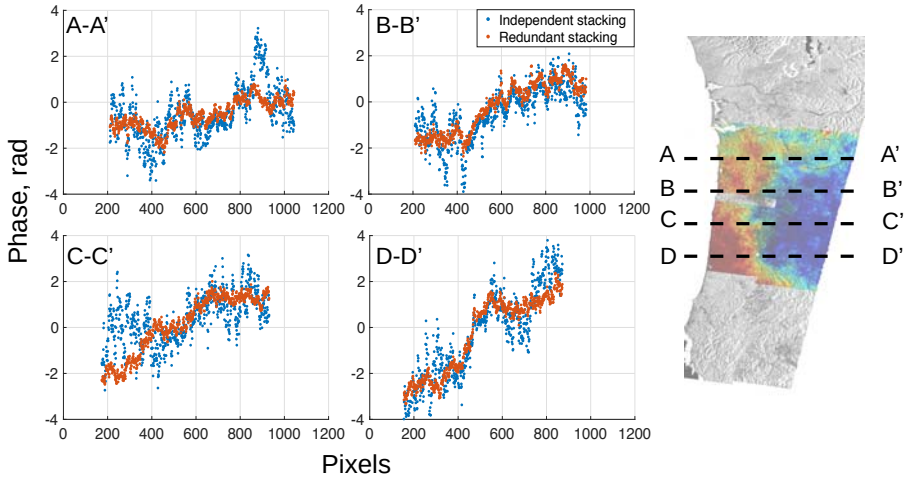

Figure 5.7: Comparisons between independent and redundant stacking results over profile lines A-A', B-B', C-C' and D-D'. Redundant stacking (red dots) produces similar mean measurements as with independent stacking (blue dots), but with much smaller phase variances.

5.4 Discussions and Conclusions

In this chapter we have described the atmospheric noise covariance model and showed how to estimate the atmospheric noise covariance matrix in practice. We have described our proposed decorrelation covariance model and compared the proposed model with two existing models – the Hanssen model and the Agram-Simons model. We have also validated our proposed decorrelation covariance model using real data in two regions with different scattering properties.

In this section, we have shown that different stacking strategies can have significant impact on noise reduction. Specifically, we compared independent stacking and redundant stacking, as well as weighted and non-weighted stacking.

We have shown that, for weighted stacking, interferograms with more weight contribute more to the overall residual noise in the stack. We have also shown that,

contrary to some conventional assumptions, "redundant" interferograms are not "redundant". For rapidly decorrelating surfaces, decorrelation noise components are either not at all, or only weakly correlated between interferograms, with or without common acquisitions. Therefore, incorporating redundant interferograms into InSAR time-series analyses can help further reduce decorrelation noise.

With the atmospheric noise covariance model as well as the proposed decorrelation covariance model, we can better quantify uncertainties in InSAR time-series analyses. As we head into an era with an ever-growing SAR archive, understanding and quantifying uncertainties associated with atmospheric noise and decorrelation noise is an important step towards building a rigorous and comprehensive noise covariance model, which is of critical importance for the InSAR community to better assessed uncertainties with the InSAR measurements, and extended the InSAR application from mid-to-high correlation areas to low-correlation areas.

Chapter 6

Imaging Cascadia slow slip using InSAR

In this chapter, we present our use of InSAR to observe Cascadia slow slip events. In particular, we show an example where we retrieve SSE-related deformation from a 2015-2016 winter Oregon slow slip event.

6.1 Data

We found 303 Sentinel-1A and B scenes acquired over the Cascadia region between June 2015 and May 2018 (Copernicus Sentinel data 2015-2018, retrieved from ASF DAAC 7 May 2018, processed by ESA, `https://www.asf.alaska.edu`). Adopting the method described in Chapter 4, we processed and combined these scenes into 96 geocoded and topography-corrected scenes. Fig. 6.1 shows the spatial coverage of these combined SAR scenes – the area between $43°N$ and $46°N$ (Central Cascadia) enjoys the most coverage and only a small area around the Columbia river is covered by every scene (96 scenes in total). Since copious data coverage is essential in reducing interferometric measurements errors, we limit our study area to Central Cascadia

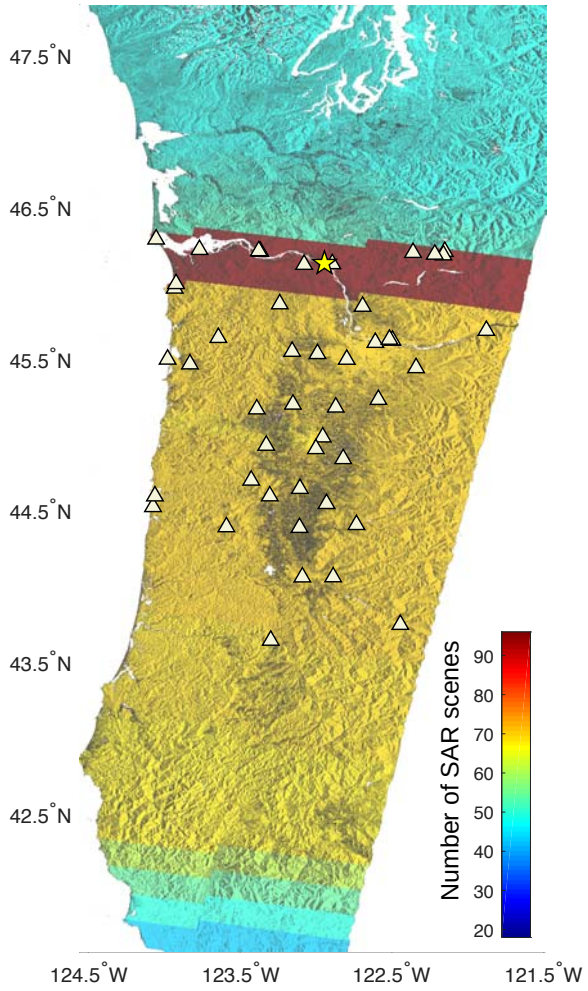

Figure 6.1: Sentinel data coverage map overlaid on the amplitude image of the study area. Only a small area around the Columbia River is covered by every SAR scene (96 in total). Central Cascadia enjoys the more coverage than Southern and Northern Cascadia. A total of 45 GPS stations are used in this study and their locations are marked as triangles. The reference point chosen is marked as a star.

where at least 70 scenes were acquired. We then proceeded to form interferograms using these topography corrected and geocoded SLCs and unwrap interferograms using a statistical minimum cost-flow phase unwrapping algorithm (*Chen and Zebker*, 2001).

Table 6.1: Slow Slip Events in Cascadia between 2015 and 2018

Slow Slip Events	Starting time	Ending time	Location
2015-2016 winter	Jan-20-2016	Mar-01-2016	Central Cascadia
2016-2017 winter	Feb-18-2017	Apr-06-2017	Northern Cascadia
2017-2018 winter	Dec-05-2018	Jan-07-2018	Central Cascadia

We use the Pacific Northwest Seismic Network (PNSN) tremor catalogue (`http://pnsn.org/tremor`) to identify start and end dates for slow slip events during the study period. We find that three SSEs took place between June 2015 and May 2018 (See Table 6.1), with the first and the third occurring mainly in Oregon, and the second in Washington. Considering data coverage in space and time, we focus on the first SSE, which occurred in winter 2015-2016 in Central Cascadia. This event has also been identified by *Michel et al.* (2018) as Event 54 in their SSE catalog. Fig. 6.2 shows the respective time spans of the two Oregon SSEs as well as Sentinel-1 scene acquisition dates. Since the 2016-2017 winter Washington SSE is not well covered by our data, we choose to omit this event.

We also use daily sampled GPS position time series provided by the Pacific Northwest Geodetic Array, Central Washington University (`http://geodesy.cwu.edu`, last access August 2019), to compare with InSAR measurements. The locations of GPS stations used in this thesis are shown in Fig.6.1.

Fig. 6.3 presents two unwrapped interferograms that span the 2016 winter Oregon

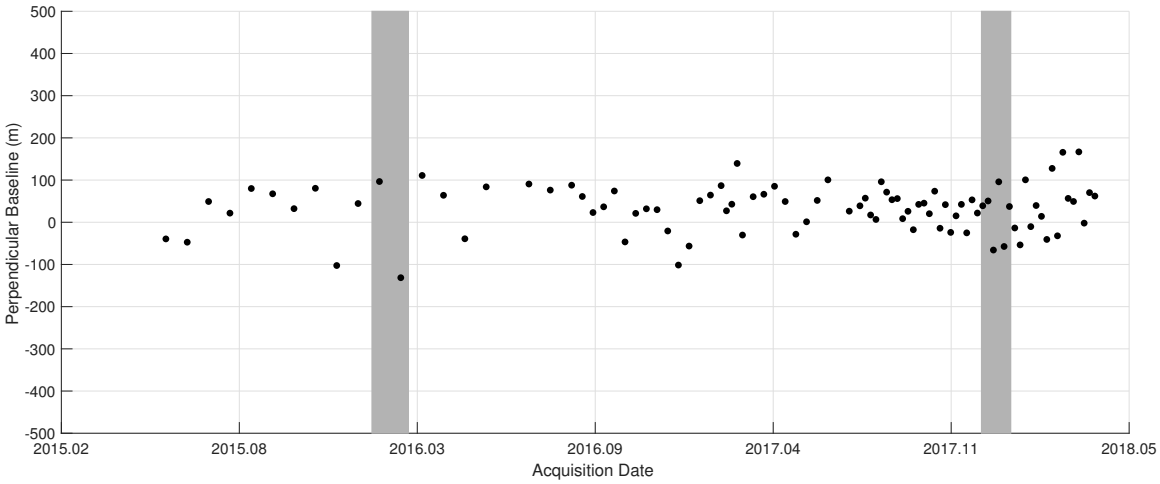

Figure 6.2: Acquisition times and relative positions of the Sentinel-1A and 1B orbits between June 2015 and May 2018. The gray areas indicate the time spans of two Oregon SSEs that took place during this period. We omit the Washington event as it is not covered well by our data.

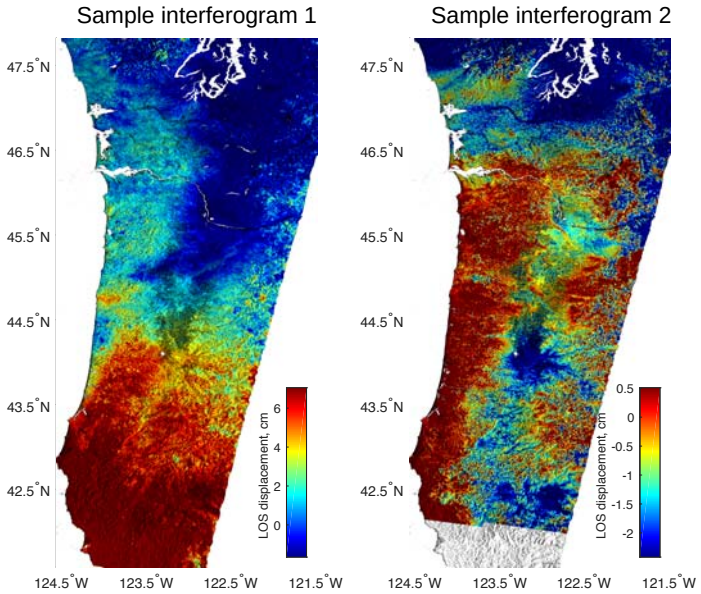

Figure 6.3: (Left) A sample interferogram formed with scenes acquired on 29 Jan 2016 and 22 February 2016. (Right) A sample interferogram formed with scenes acquired on 5 Jan 2016 and 17 March 2016. Both interferometric measurements are dominated by atmospheric signals rather than actual SSE deformation.

slow slip event. Even though these two samples have relatively short temporal time span (24 days and 72 days) and hence enjoy relatively high correlation, we note that both interferometric measurements are dominated by atmospheric signals rather than the actual SSE deformation. In the next few sections, we discuss in detail how stacking can be applied to retrieve surface deformation signals related to the slow slip event. We also present uncertainties associated with measurements using temporal noise covariance matrices presented in Chapter 5.

6.2 Method: Stacking

Stacking is a simple yet effective method that reinforces temporally coherent signals such as deformation while mitigating temporally uncorrelated or weakly-correlated signals such as atmospheric and decorrelation noise.

The unwrapped interferometric phase u_{ij} between the i^{th} and the j^{th} SAR measurement that spans the slow slip event can be decomposed as the sum of various terms:

$$u_{ij} = d + vT_{ij} + p_{ij} + \epsilon_{ij}^{atm} + \epsilon_{ij}^{decor} + \epsilon_{ij}^{n} + c_{ij} \tag{6.1}$$

where d is deformation associated with the slow slip event, and v represents inter-SSE velocity. Note that v here is different than interseismic velocity as the latter is defined over a much longer timescale. In a short timescale such as the three year window of this study, signals other than tectonic loading (for example, hydrological) can complicate estimation of interseismic velocities. Therefore, the inter-SSE velocity v should be interpreted as an assumed linear line-of-sight inter-SSE velocity that best describes the general deformation trend of the study area between June 2015 and May 2018. T_{ij} represents the time interval between acquisition of the i^{th} and j^{th} SAR scene, p_{ij} represents the elastic response of the Earth's crust to seasonal

hydrological loading effect (*Farrell*, 1972; *Fu et al.*, 2015), ϵ_{ij}^{atm} is atmospheric noise, ϵ_{ij}^{decor} is decorrelation noise, and ϵ_{ij}^{n} represents all other noise sources such as residual DEM error and thermal noise, c_{ij} is a constant that results from the relative nature of InSAR measurements and is generally different in every interferogram. Due to the presence of c_{ij} and non-uniform spatial coverage of the SAR scenes (Fig. 6.1), and hence non-uniform spatial coverage of interferometric measurements, we use a reference pixel u_{ij}^{r} to re-calibrate the zero-phase reference of every interferogram:

$$\begin{aligned} u_{ij} - u_{ij}^{r} =& d - d^{r} + (v - v^{r})T_{ij} + p_{ij} - p_{ij}^{r} + \\ & \epsilon_{ij}^{atm} - \epsilon_{ij}^{atm,r} + \epsilon_{ij}^{decor} - \epsilon_{ij}^{decor,r} + \epsilon_{ij}^{n} - \epsilon_{ij}^{n,r} \end{aligned} \tag{6.2}$$

Similarly, for an interferometric measurement that does not span any slow slip events, we have

$$\begin{aligned} u_{ij} - u_{ij}^{r} =& (v - v^{r})T_{ij} + p_{ij} - p_{ij}^{r} + \\ & \epsilon_{ij}^{atm} - \epsilon_{ij}^{atm,r} + \epsilon_{ij}^{decor} - \epsilon_{ij}^{decor,r} + \epsilon_{ij}^{n} - \epsilon_{ij}^{n,r} \end{aligned} \tag{6.3}$$

The location of the reference point we chose is marked in Fig. 6.1.

Averaging interferometric measurements that span the SSE yields:

$$\begin{aligned} \frac{1}{N}\sum\left(u_{ij} - u_{ij}^{r}\right) =& d - d^{r} + \frac{\sum T_{ij}}{N}(v - v^{r}) + \frac{1}{N}\sum\left(p_{ij} - p_{ij}^{r}\right) \\ & \frac{1}{N}\left[\sum\left(\epsilon_{ij}^{atm} - \epsilon_{ij}^{atm,r}\right) + \sum\left(\epsilon_{ij}^{decor} - \epsilon_{ij}^{decor,r}\right) + \sum\left(\epsilon_{ij}^{n} - \epsilon_{ij}^{n,r}\right)\right] \end{aligned} \tag{6.4}$$

where N is the number of interferograms that covers a given pixel in the stack. We show in the following sections that by stacking, we can reduce InSAR noise

uncertainties to sub-cm level. Similarly, averaging interferograms that do not span any SSEs can lead to an estimation of the inter-SSE velocity v:

$$\frac{\sum\left(u_{ij}-u_{ij}^{r}\right)}{\sum T_{ij}} = v - v^{r} + \frac{\sum\left(p_{ij}-p_{ij}^{r}\right)}{\sum T_{ij}} \\ \frac{1}{\sum T_{ij}}\left[\sum\left(\epsilon_{ij}^{atm}-\epsilon_{ij}^{atm,r}\right)+\sum\left(\epsilon_{ij}^{decor}-\epsilon_{ij}^{decor,r}\right)+\sum\left(\epsilon_{ij}^{n}-\epsilon_{ij}^{n,r}\right)\right] \tag{6.5}$$

6.2.1 Choosing the Best Stacking Strategies

There are 580 interferograms that span the SSE and 1888 interferograms that do not span any SSEs. However, including every possible interferogram in the stack is not necessarily the optimal stacking strategy in terms of noise reduction, as we have discussed in Chapter 5. It is necessary to first analyze the strength and the statistics of various noise sources that are present in our measurements.

Apart from the desired slow slip deformation d and inter-SSE velocity v, Eqns. [6.4] and [6.5] also contain contributions from seasonal signals caused primarily by hydrological loading, atmospheric noise, decorrelation noise, and other noise sources such as DEM error and thermal noise.

Seasonal Signals

Fu et al. (2015) report an average seasonal range of about 1 cm vertical displacement in mountainous areas such as the Cascadia range and Olympic mountains. To assess the strength of seasonal signals that may be present in our measurements, we analyzed GPS vertical measurements in the study area. Fig. 6.4 presents raw GPS vertical measurements and modeled vertical displacements. We model the time-series as the

sum of linear, annual, and semi-annual components:

$$\begin{aligned} f(t) =& vt + d \cdot H(t - t_{sse}) + \\ & a_1 + a_2 sin(2\pi t) + a_3 cos(2\pi t) + a_4 sin(4\pi t) + a_5 cos(4\pi t) \end{aligned} \tag{6.6}$$

where $H(t)$ represents the Heaviside function and a_i are coefficients for the periodic terms. From Fig. 6.4 we can see that all stations exhibit seasonal oscillations. In addition, we observe that: (1) peaks and troughs of the seasonal signal are generally aligned at every GPS station (with the exception of station WDBN), with the peak occurring around October (the end of summer) and the trough occurring around April (the end of winter); (2) different stations exhibit different seasonal range in deformation – seasonal range is defined as the difference in position between peak and trough displacements; and (3) most stations exhibit a long-term (relatively speaking) trend of subsidence that could possibly be related to the long-lasting drought Oregon endured between 2011 and 2017 (`https://www.drought.gov/drought/states/oregon`). Given that InSAR measurements are mostly sensitive to vertical deformation, this observed subsidence is likely reflected in the inter-SSE velocity v derived from InSAR measurements along with tectonic loading from the subducting Juan de Fuca plate.

Next we examine the difference in seasonal range in deformation among GPS stations. Similar to the findings in *Fu et al.* (2015), we find that mountainous regions exhibit higher seasonal ranges – up to 1.2 cm when projected to LOS direction than the 0.75 cm seasonal range in LOS deformation found in stations located in valley and basin areas (Fig. 6.5). Because the stations exhibit general alignments of peaks and troughs of seasonal signals and that InSAR measurements are inherently relative, only spatial variation of seasonal ranges will be present in the final InSAR stack. This

means that there is at most 1-2 mm change across the image in the averaged SSE stacks and up to 5 mm between the valleys and mountainous areas (Eqn. [6.4]). However, since the inter-SSE velocity stack (Eqn. [6.5]) is weighted inversely by time span, seasonal signals in these short time-span interferometric measurements are amplified compared to the longer temporal baseline pairs. Therefore, for the inter-SSE velocity stack, we choose to only include pairs that are acquired at similar times of the year, which decreases the number of interferograms in the inter-SSE stack from 1888 to 241.

Atmospheric noise

Atmospheric noise consists of two main parts: (1) phase delays due to pressure change with time, and (2) phase delays due to variability of water vapor content in the troposphere (*Zebker et al.*, 1997). The former correlates with elevation and the latter is commonly modeled as a stochastic variable with assumed zero mean. We find a correlation between phase measurements and elevation of about 10^{-4} rad/m, which is equivalent to 5 mm line-of-sight distance change for every 1000 m change in elevation. We can compute and remove these elevation-related phase noises from the stack. The second part of the atmospheric noise cannot be corrected in a deterministic way. Instead, we adopt the stochastic model described in Chapter 5 to estimate the atmospheric noise covariance matrix and to keep track of atmospheric noise propagation. With the covariance matrix, we can compute the residual atmospheric variance in any given interferometric stack.

For a non-weighted stack such as the SSE stack described in Eqn. [6.4], atmospheric noise variance reduction is readily determined by the structure of the covariance matrix. Generally, a trade-off between the number of independent radar measurements and an uniform use of radar measurements is needed in order to achieve

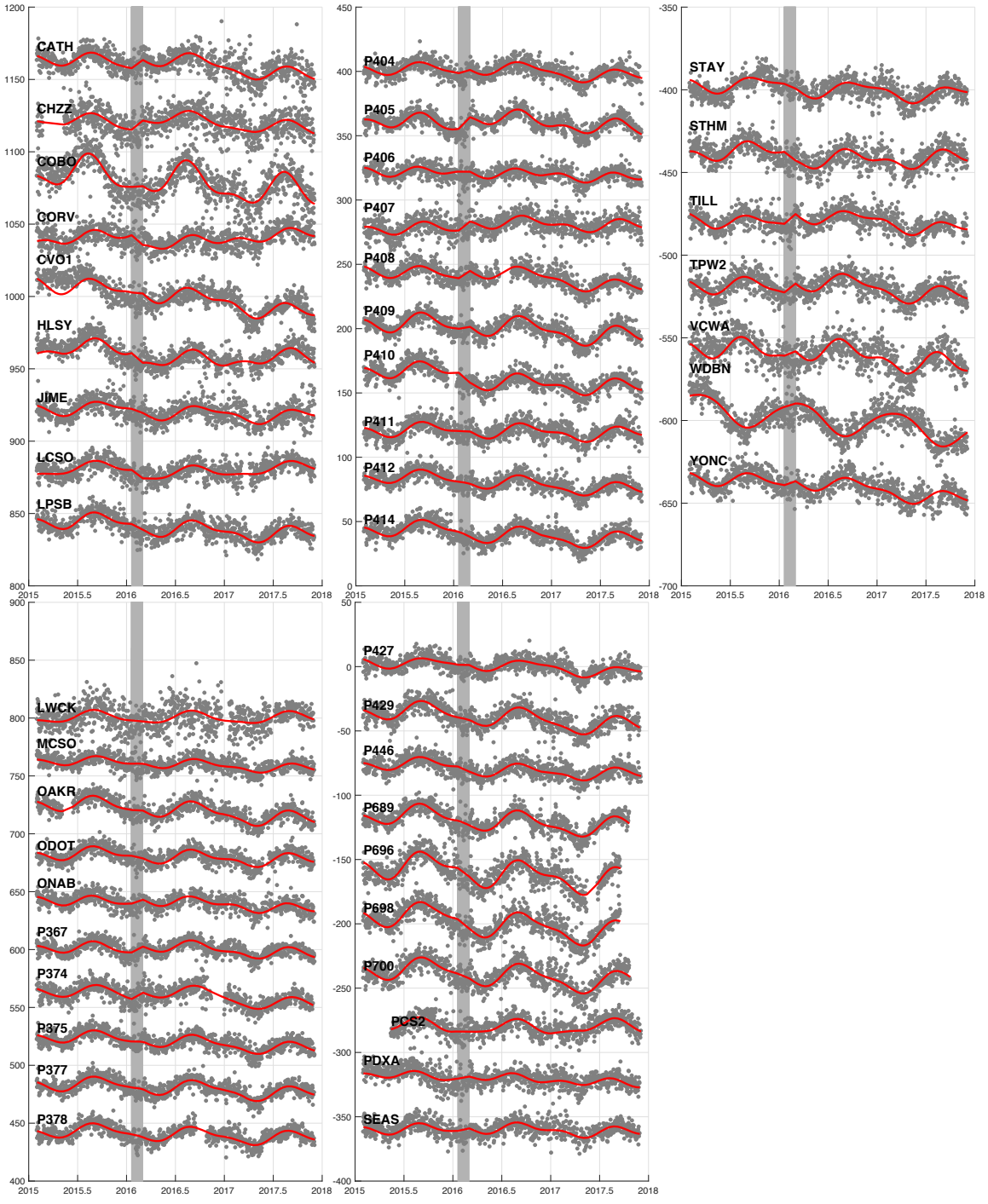

Figure 6.4: GPS vertical measurements(unit: mm). Raw data are shown as grey dots. Red lines are modeled vertical displacements with linear, annual and semi-annual components. The SSE period is marked by a dark gray column.

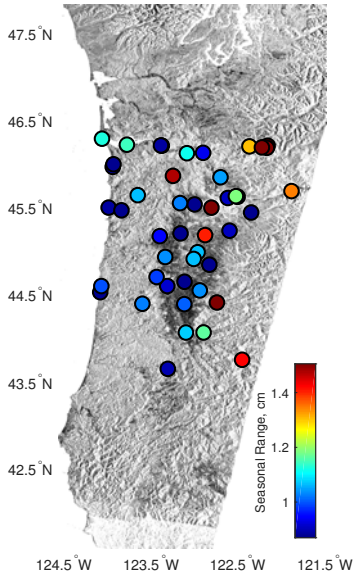

Figure 6.5: GPS measurements seasonal range in LOS deformation. Seasonal range is defined as the total variation in deformation annually. Most stations exhibit around 0.75 to 1 cm seasonal range. A few stations in the mountainous regions show higher seasonal range.

best reduction of atmospheric noise: (1) the more independent number of radar measurements, the better reduction in atmospheric noise and (2) the more uniform use of radar measurements, the better reduction in atmospheric noise. In our case, we have 10 acquisitions before the SSE and 58 after. If we use only the first 20 acquisitions, we can guarantee a uniform use of the acquisitions – each acquisition is used 10 times when redundant interferogram stacking is applied, at a cost of not making use of the other 48 independent measurements. On the other hand, if we make use of all 58 interferograms, each of the first 10 acquisitions is used 58 times whilst each of the other 58 acquisitions is only used 10 times. Taking into account the spatial coverage of the SAR scenes, we choose to use 31 acquisitions (10 acquisitions before the SSE and the first 21 acquisitions after the SSE). For acquisitions after the SSE, we choose the first 21 rather than the last 21 because they have shorter temporal spans. Shorter temporal spans interferograms (1) have a smaller contribution from inter-SSE velocity

and (2) usually have better correlation.

For a weighted stack such as the inter-SSE stack described in Eqn. [6.5], the weights applied make a great impact on the residual noise in the stack. Since atmospheric noises in short temporal span interferometric pairs are weighted much more heavily than long temporal pairs, we choose to use pairs that have at least 300 day temporal span. This further decreases the number of interferograms in the inter-SSE stack from 241 to 87.

Decorrelation noise

As previously discussed in Chapter 5, we find that redundant stacking reduces decorrelation noise more efficiently than independent stacking in rapidly decorrelating surfaces such as Cascadia (e.g. Fig. 5.6 and 5.7). Therefore, for both stacks, once we selected the SAR acquisitions to be used, we make use of all possible pairs that meet our requirement.

Other noise terms

Other noise terms include DEM error, orbital ramps, co-registration errors and thermal noise. All these errors sources are negligible with modern SAR satellites such as Sentinel-1 except for potential DEM error. In Section 4, we estimate DEM error in a single interferometric measurement (Eqn. [4.14]). With range $\rho \approx 750$ km, incidence angle $\theta \approx 30°$, and spatial baseline $B \approx 100$ m, we find that every 10 meters of DEM error results in 2 mm error in a single pair of interferometric measurements. Given that DEM errors are typically under 5 meter for flat areas and under 10 meters for mountain regions, residual noise in the stack caused by DEM error is negligible

compared to atmospheric and decorrelation noise, and hence does not influence our choice of stacking strategies.

6.2.2 Extracting SSE Deformation and Associated Uncertainties

In summary, to best reduce noise, we form the SSE stack with 210 interferograms that span the SSE and the inter-SSE stack with 87 interferograms that do not span the SSE and have temporal baselines of 365 ± 20 days. Fig. 6.6 presents results of both stacks. The expected seasonal deformation signal is minimum in both stacks, therefore omitting the seasonal deformation term $p(t)$ in Eqn.[6.4] and Eqn. [6.5], we now have two stacks that contain primarily the desired deformation signals. Combining Eqns. [6.4] and [6.5], we can remove inter-SSE deformation from the SSE stack and extract deformation associated with the SSE.

Fig. 6.7 presents the extracted SSE line-of-sight deformation map and its associated uncertainty (standard deviation). We find that atmospheric noise is the dominant residual error source, accounting for on average 90% of the total uncertainty. The lowest uncertainties are around areas where the reference pixel is located. This is because that atmospheric noise variance is lower closer to the reference pixel than from farther away (see Eqn. [5.4]). Since the maximum distance from the reference point, 300 km, is much smaller than the critical value of 800 km, above which the power-law behavior of atmospheric noise is no longer observed, our estimation of atmospheric noise uncertainties based on the power-law behavior of atmospheric noise (previously presented in Chapter 5) is valid.

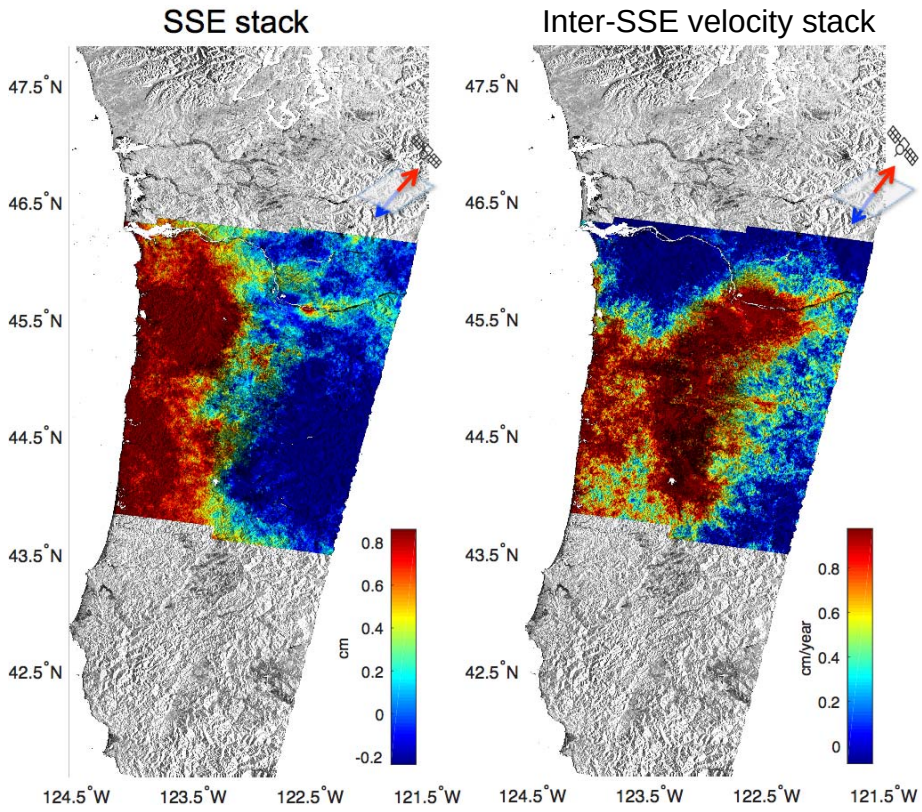

Figure 6.6: Left: SSE stack results from averaging 210 interferograms that span the 2015-2017 winter Oregon slow slip event. Right: Inter-SSE velocity stack results from averaging 87 interferograms with a temporal span of one year. Both measurements reflect projected deformation onto the line-of-sight (LOS) direction (unit vector pointing from the ground to the satellite: $\vec{v} = (v_E, v_N, v_U) = (0.59, -0.11, 0.79)$)

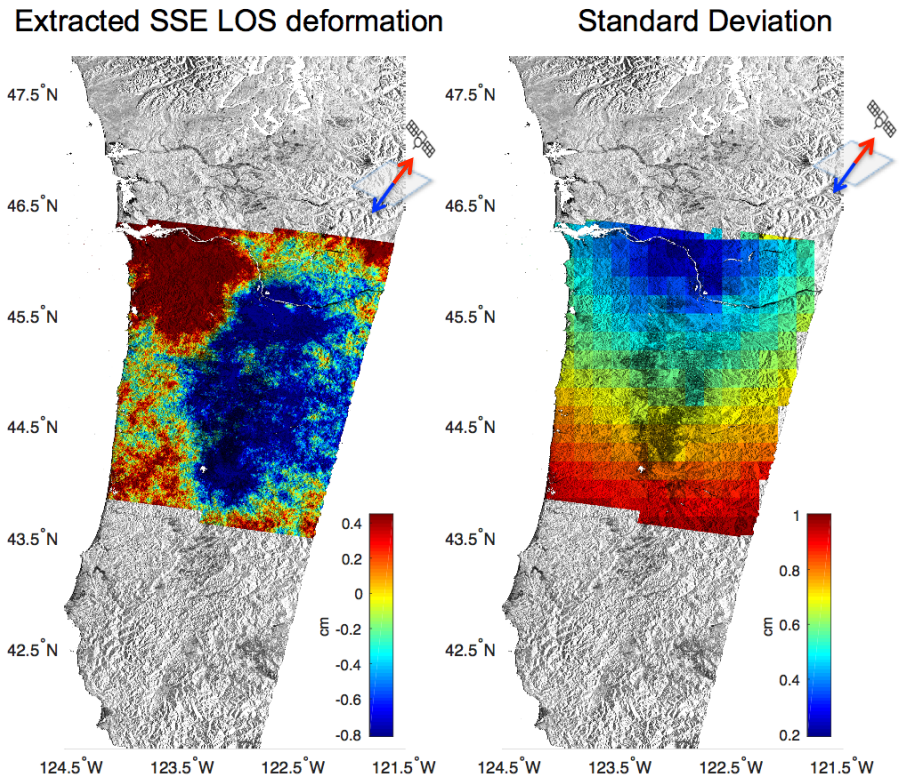

Figure 6.7: (Left) Extracted line-of-sight (LOS) deformation of the slow slip event and (Right) associated uncertainties. The range of extracted SSE LOS deformation is about 1 cm. The uncertainties are dominated by atmospheric noise, which accounts for 90% of total uncertainty and decorrelation noise accounts for the rest 10%. Uncertainties are lowest around the region where the reference point locates and increase with increasing distance from the reference point.

We note that choosing multiple reference points that are relatively far from each other can usually further reduce atmospheric noise and results in a more uniformly distributed uncertainty map. However, our choice of the reference point is restricted to the Columbia river area – the only area that is covered by every SAR scene. Nonetheless, almost the entire area achieves sub-cm level accuracy, with roughly half of the areas achieving less than 5 mm uncertainty.

6.3 Comparison With GPS Measurements

In this section we compare our extracted SSE deformation map (Fig. 6.7) with GPS measurements. By fitting GPS position time-series to a model that is composed of linear, transient, and periodic components (Eqn. [6.6]), we can extract both SSE deformation and inter-SSE velocities. Fig. 6.8 shows such an example. Note that GPS vertical measurements are much noisier than GPS horizontal measurements. Fig. 6.9 presents the extracted SSE displacements from GPS measurements. We observe that:

(1) Extracted GPS horizontal displacements have smaller uncertainties than vertical displacements. This is because GPS vertical measurements are usually much more noisy than horizontal measurements.

(2) A significant portion of horizontal motion is in the North-South direction. However, radar measurements are insensitive to motion in the North-South direction. This means that InSAR measurements of the SSE event are dominated by projections of the vertical deformation.

(3) Though projected GPS line-of-sight measurements mostly reflect the extracted vertical displacements, and hence carry a lot of uncertainty, both the range of signals

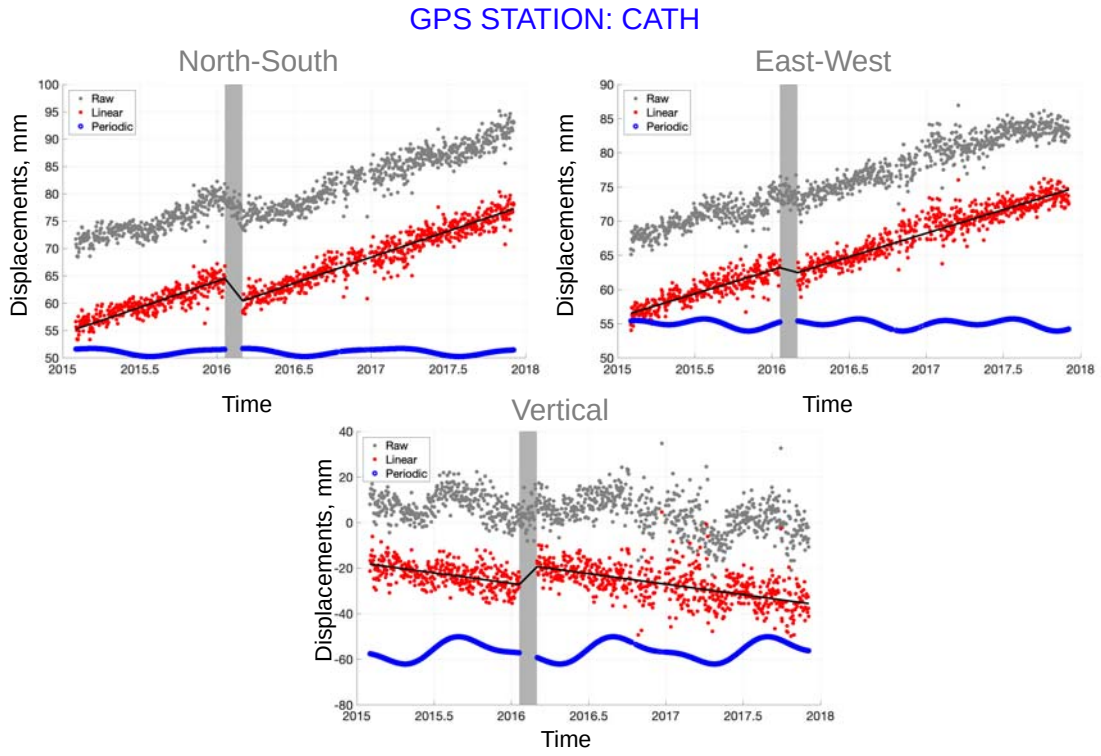

Figure 6.8: An example of three component GPS data processing at Station CATH. Gray dots are raw GPS measurements. Red dots represent modeled linear and transient signals. Blue dots are modeled annual and semi-annual components.

($\approx$ 1 cm) and the pattern of the deformation agrees well with the extracted SSE deformation from InSAR measurements.

Fig. 6.10 shows comparisons between InSAR derived SSE deformation and GPS derived SSE deformation projected to line-of-sight direction. InSAR measurements in general agree with GPS measurements and their differences are within one standard deviation of their respective measurements. The profile lines demonstrate the superiority of InSAR measurement spatial sampling rate, as it is obvious that GPS measurements are too sparse to sample SSE deformation transition from peak uplift to peak subsidence.

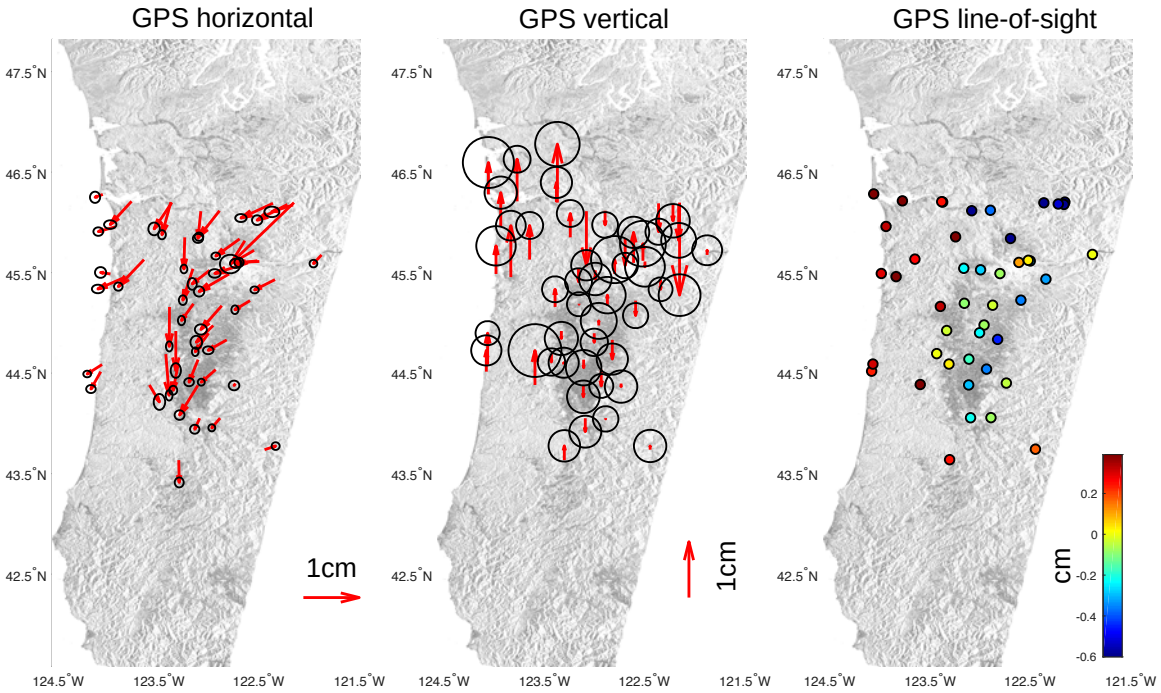

Figure 6.9: GPS measurements of the 2015-2016 winter Oregon slow slip event. (Left) Extracted GPS horizontal displacements and uncertainties. (Middle) Extracted GPS vertical displacements and uncertainties. (Right) Projected GPS measurements of the SSE onto line-of-sight direction.

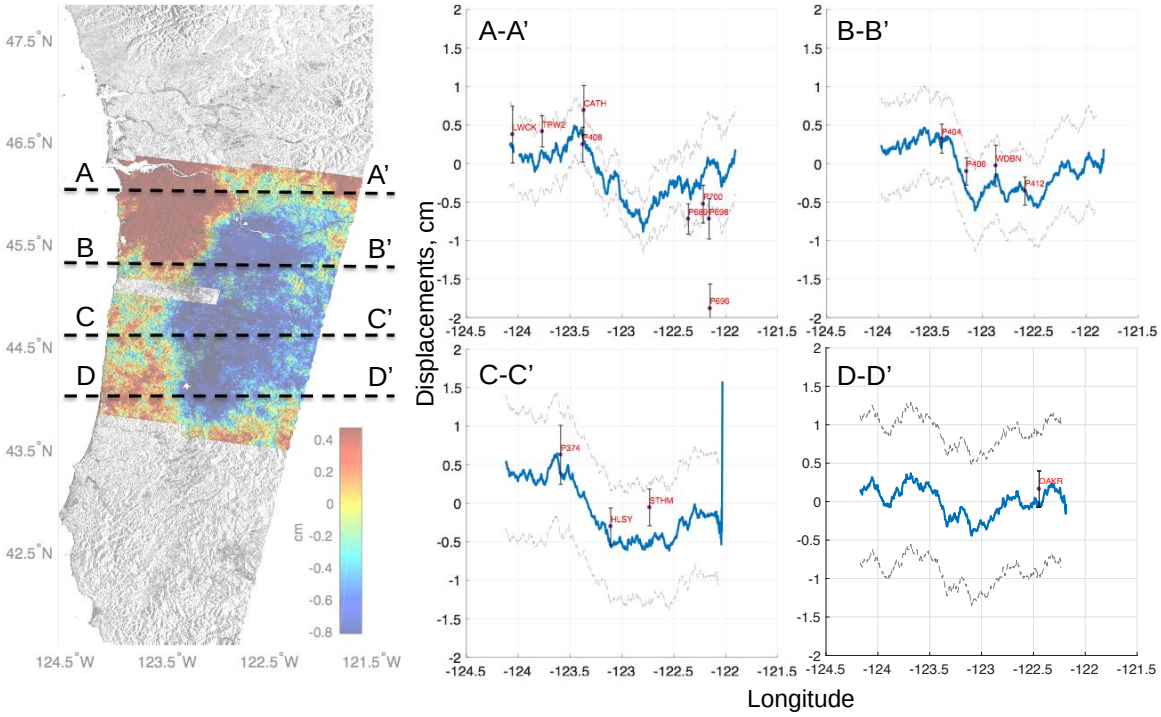

Figure 6.10: Comparison between InSAR derived slow slip event deformation and GPS derived three component SSE deformation projected onto radar line-of-sight direction. Both measurements exhibit a similar range of deformation of ~ 1 cm. The blue lines are profiles of InSAR measurements shifted to zero-means. The gray lines show the standard deviation of the InSAR derived SSE deformation. GPS measurements are shown as red dots with error bars.

6.4 Conclusions

In this chapter we provided InSAR measurements of surface deformation related to the winter 2015-2016 Central Cascadia slow slip event and uncertainties in InSAR measurements after stacking.

We created two stacks, one composed of 210 interferograms that span the winter 2015-2016 slow slip event and the other composed of 87 interferograms that do not span any slow slip events. From the latter stack, we derived the inter-SSE velocity of the region and subtracted the inter-SSE velocity contribution from the SSE stack in order to retrieve surface deformation caused by the slow slip event. We find that the winter 2015-2016 slow slip event gives rises to about 1cm surface deformation in radar line-of-sight direction, consistent with preliminary GPS observations of the same slow slip event. Error analysis showed that atmospheric noise is the dominant noise source as decorrelation noise has been effectively reduced by redundant stacking.

In the next chapter, we will show how the dense spatial sampling and the vertical sensitivity of InSAR measurements lead to more accurate locations of slow slip patches on the plate boundary.

Chapter 7

Modeling Slow Slip Events in Cascadia

In this chapter, we demonstrate what new information InSAR data can contribute to SSE modeling. We first present a two-dimensional model to demonstrate what factors of slip distribution control the pattern of surface deformation projected to radar line-of-sight direction. We then present results using the extracted SSE deformation from InSAR measurements and a three-dimensional fault geometry model as determined by *McCrory et al.* (2012).

7.1 Modeling: Two-Dimensional

Fig. 7.1 presents a simplified 2D geometric model of the Central Cascadia region. We prescribe 2 cm up-dip slip between depths of 30 km and 40 km and use 2D edge dislocation models (*Segall*, 2010) to map slip at depth to displacements on the surface.

Fig. 7.2 illustrates horizontal and vertical surface displacements generated by 2

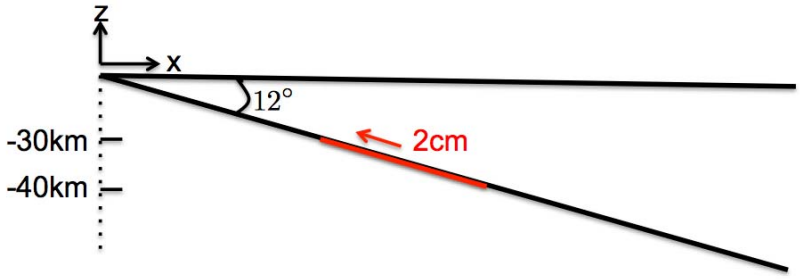

Figure 7.1: 2D geometry of the Cascadia subduction zone plate boundary. A uniform 2 cm up-dip slip is assumed between 30 km to 40 km depth.

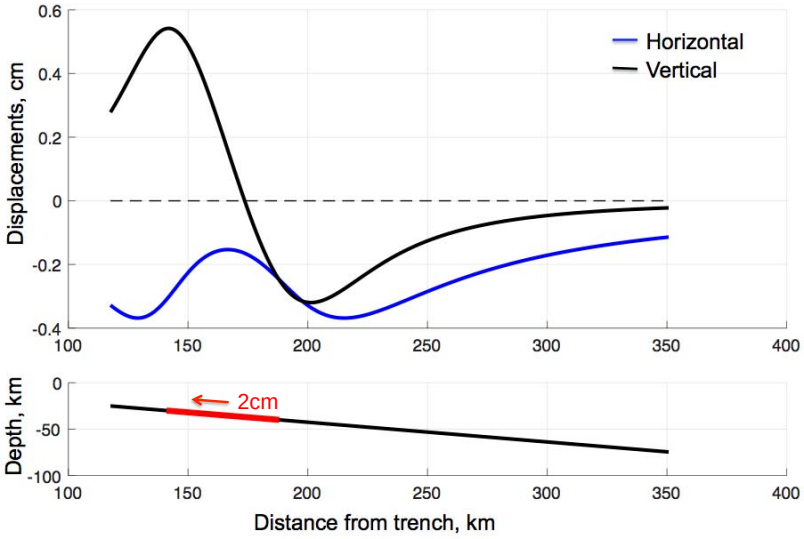

Figure 7.2: Simulated surface vertical (black) and horizontal (blue) displacements caused by a uniform 2 cm slow slip between depth 30 km and 40 km using a 2D edge-dislocation model.

cm uniform up-dip slip between 30 km and 40 km depth. We note that:

(1) Up-dip slip at depth generates more vertical deformation on the surface than horizontal deformation. While the maximum horizontal and vertical displacements are of comparable magnitude (in this example, ~ 0.5 cm for vertical displacements and ~ 0.4 cm for horizontal displacements), the range of vertical displacements (~ 1 cm) is three times as big as the range of horizontal displacements (~ 0.3 cm). Projecting onto radar line-of-sight direction, contributions from horizontal displacements account for 20% of the InSAR observations of the SSE, while vertical displacements account for 80% of observed InSAR measurements.

(2) The locations of the peak and the trough of vertical displacements correlate well with the locations of the up-dip and down-dip limit of the SSE zone. In particular, the peak of vertical displacements locates almost directly on top of the up-dip limit of the SSE zone. Therefore, InSAR measurements are very sensitive to the locations of the SSE zones at depth.

(3) The range of vertical displacements correlates linearly with slip. More slip at the depth means larger displacements range on the surface.

Therefore, given the correlation between the up-dip and down-dip limits of the SSE and the peak and trough of vertical measurements, as well as the linear relation between the magnitude of slip and the range of surface deformation, we can locate SSE zones at depth and estimate the amount of slip with 2D profiles of InSAR measurements using a simple uniform slip 2D model (Fig. 7.1). Fig. 7.3 shows that at latitude $45°N$, InSAR measurements suggest a SSE zone between 35.9 km and 52.6 km depth and a slip magnitude of 3.5 cm.

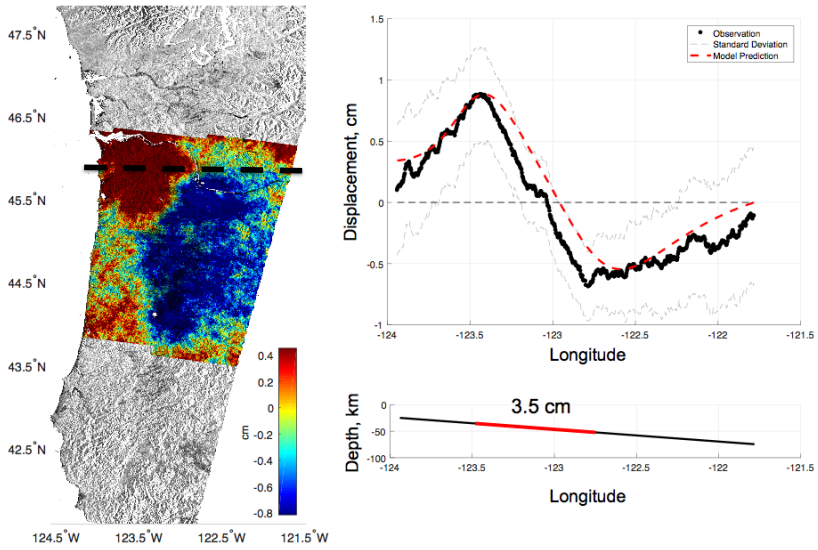

Figure 7.3: An example of locating SSE slip at depth using a 2D InSAR profile. (Left) InSAR derived surface deformation associated with the slow slip event. (Right, top) Observed (black) and predicted (red) SSE deformation along the dashed line marked on the (Left). Gray dashed lines are the 1-σ uncertainty bounds of the measurements. (Right, bottom) Plate boundary profile with the solved SSE slip zone marked as thick red lines. The up-dip and down-dip limit of the SSE slip zone is between 35.9 km and 52.6 km depth.

By analyzing profile lines at different latitude, we can acquire variations in SSE zone locations latitudinally. Fig. 7.4 demonstrate that for the 2015-2016 winter Central Cascadia slow slip event, the up-dip limit of the SSE zone migrates to shallower depth with decreasing latitude.

7.2 Modeling: Three-Dimensional

In this section, we compute a static solution for the derived SSE deformation from InSAR measurements. We adopt the fault geometry determined by *McCrory et al.* (2012) with a total number of 718 triangular sub-faults between latitude 43.5° and 46.5°. The sub-faults have a characteristic length of 12 km. We computed Green functions that map slip on these sub-faults to the surface using the dislocation model

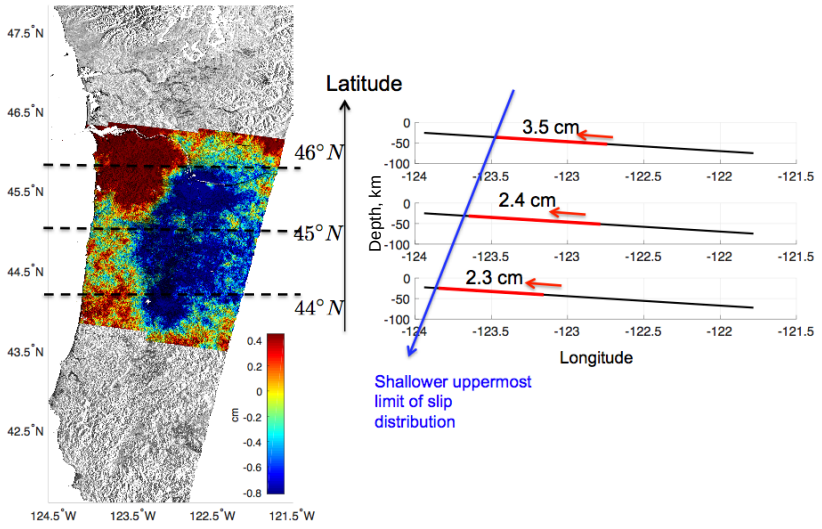

Figure 7.4: Locations of SSE slip zones vary latitudinally. (Left) Locations of the three profiles analyzed are marked as thick dashed lines. (Right) InSAR measurements derived SSE slip zone locations (thick red lines) at latitude $44°N$, $45°N$ and $46°N$. The uppermost limit of the SSE slip zone becomes shallower with decreasing latitude.

described in *Maerten et al.* (2005). To avoid over-fitting, we minimize the second-derivative of the fault slip (Laplacian smoothing).

To make our data size more manageable, we first down-sample the derived SSE deformation map (Fig. 6.7) by averaging adjacent measurements. In this way, we decreased our data samples from to 697,150 to 1,561. Fig. 7.5 shows the reduced data and their uncertainties.

Though GPS data (see Fig. 6.9) suggest a strong presence of north-south strike-slip, we choose to only include dip-slip in the SSE model. We use this approach because north-south strike-slip generates primarily north-south surface deformation, which radar measurements are insensitive to. Fig. 7.6 and Fig. 7.7 present slip distribution derived from unweighted and weighted InSAR data, respectively. The weights applied for the latter are computed using the standard deviation of InSAR data (Fig.

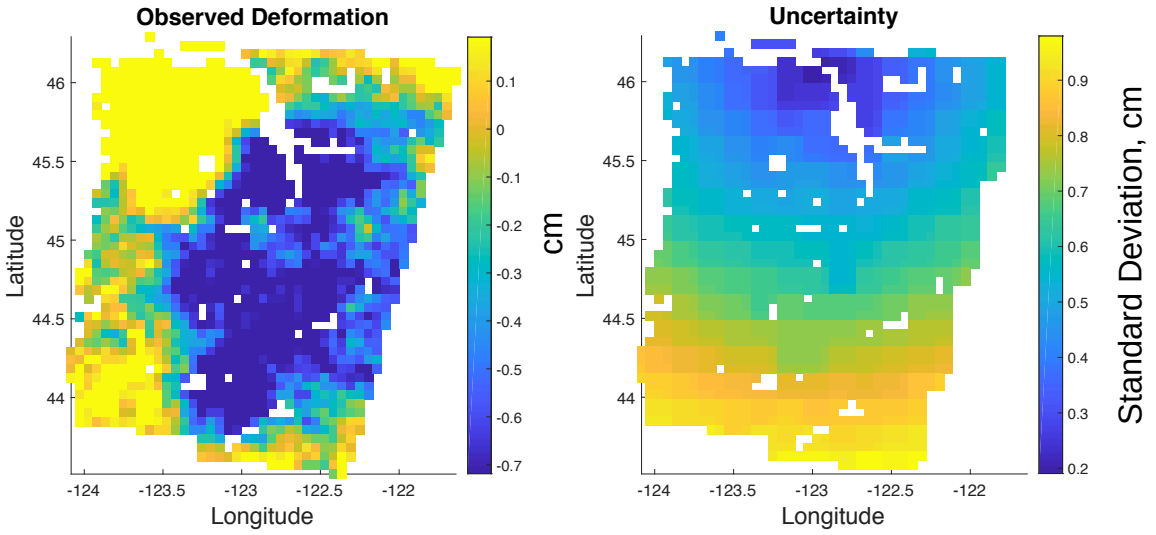

Figure 7.5: Reduced InSAR data for SSE modeling. We decreased the number of data samples from 697,150 to 1,561 by spatial averaging. (Left) InSAR derived SSE deformation map after data reduction. (Right) Standard deviation of InSAR observations.

7.5, right). Both inversion results show two major slipping patches of the fault: one mainly between $45°N$ and $46°N$ and one mainly between $45°N$ and $46°N$. Inversion results using the weighted InSAR measurements (Fig. 7.7) show more concentrated slip areas with larger slip amplitudes. We estimate that slip on the northern patch is equivalent to a Mw 6.6 earthquake and slip on the southern patch is equivalent to a Mw 6.7 earthquake.

The implied deformation pattern of the solved slip distribution at depth resembles the observed deformation pattern on the surface. As we have shown in the 2D model, the up-dip and down-dip limit of the SSE zone correlate well with the locations of the peak uplift and peak subsidence of the surface. Since InSAR measurements of the SSE deformation are dominated by vertical deformation signals, it is not surprising to observe a similar pattern in both the modeled surface expression of solved slip distribution at depth and surface deformation.

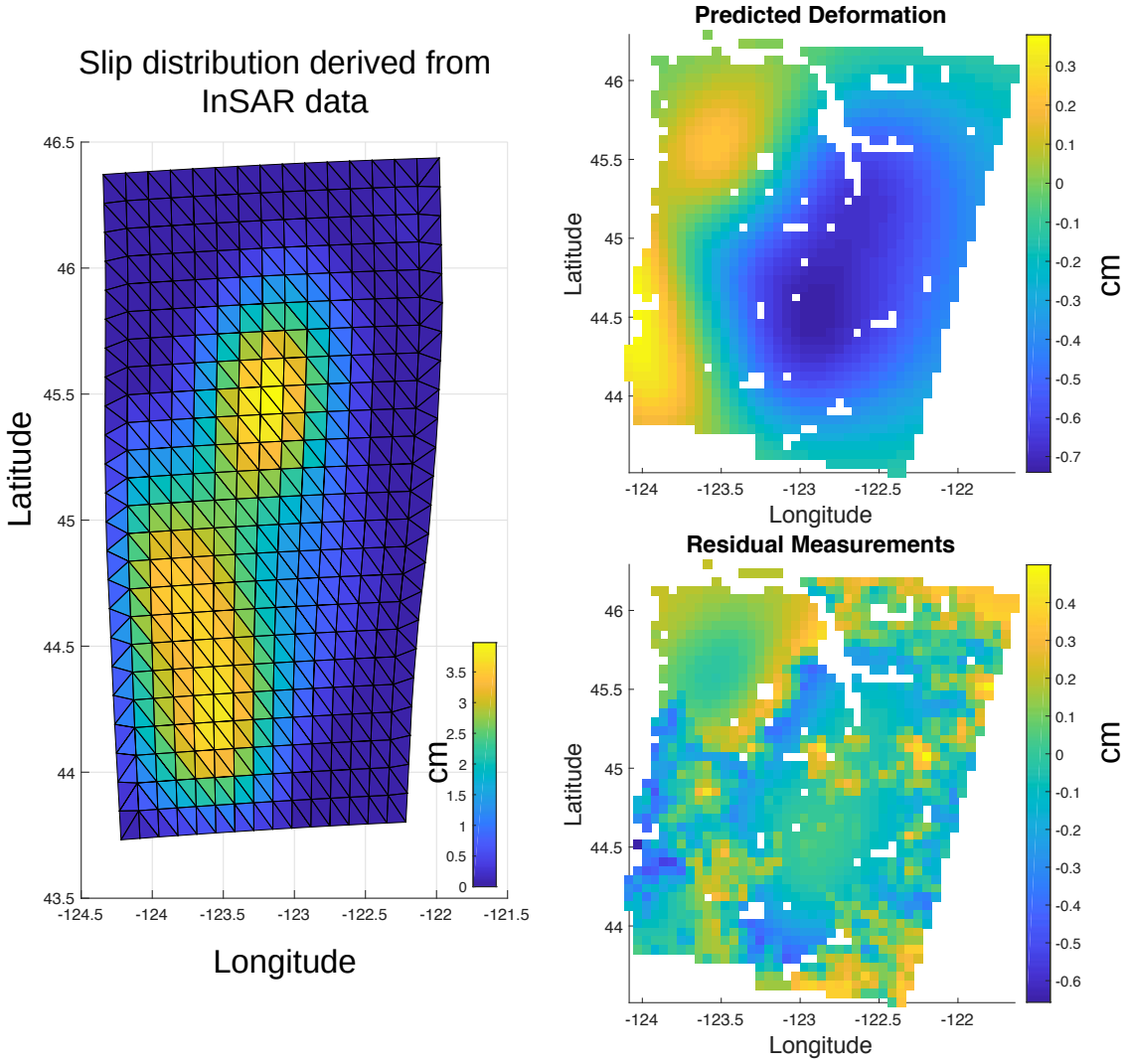

Figure 7.6: Inversion results with no weights applied. (Left) Slip distribution derived from InSAR data. (Right, top) Predicted LOS surface deformation. (Right, bottom) Residual InSAR observations. Two distinct slip patches can be identified: one above 45° and one below. Slip on the northern patch is equivalent to a Mw 6.6 earthquake. Slip on the southern patch is equivalent to a Mw 6.7 earthquake.

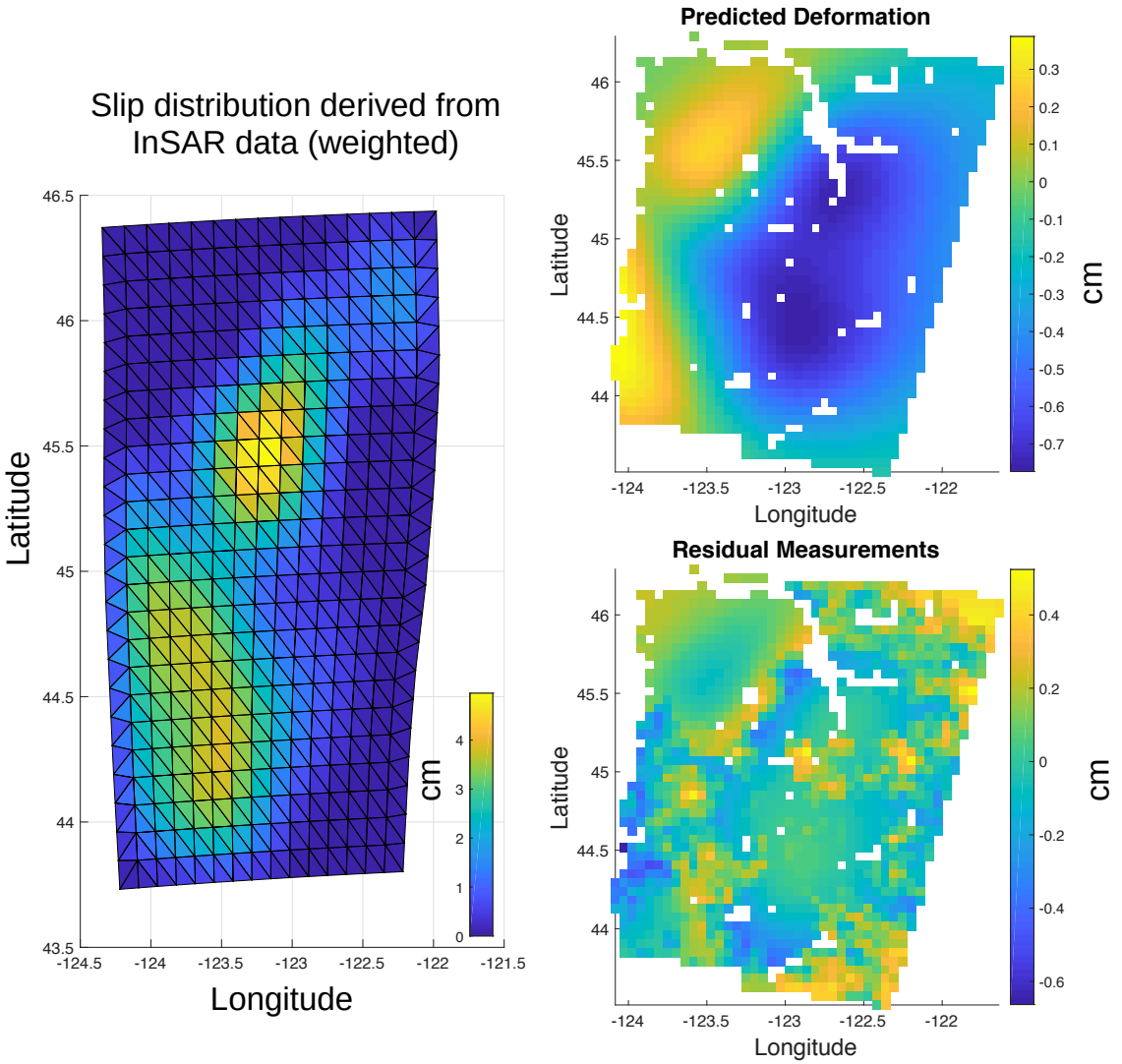

Figure 7.7: Inversion results accounting for data uncertainty. (Left) Slip distribution derived from InSAR data. (Right, top) Predicted LOS surface deformation. (Right, bottom) Residual InSAR observations. The same two slip patches can be identified, but are better resolved than those in Fig. 7.6. The same moment magnitudes of Mw 6.6 and Mw 6.7 are found for the two slip patches.

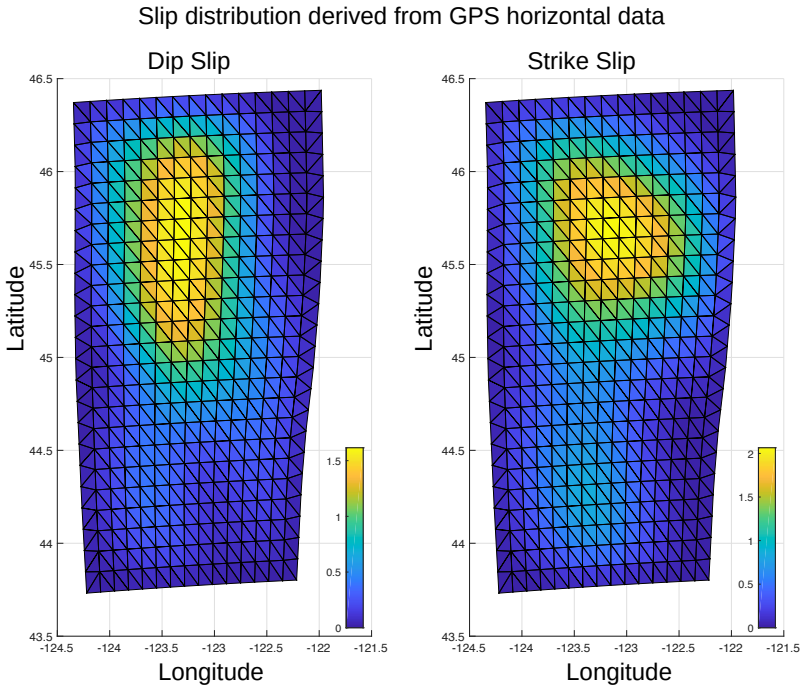

Figure 7.8: (Left) Dip slip distribution from GPS horizontal data. Only the northern slip patch (north of $45°N$) can be identified. Though the maximum slip is much smaller than in Fig. 7.7, the slip area is much more spread out than in Fig. 7.7, resulting in the same moment magnitude of Mw 6.6. (Right) Strike slip (southwards) distribution from GPS horizontal data.

As a further comparison, we use horizontal GPS data (See Fig. 6.9) to solve for slip distributions at depth. We invert for both dip slip component and strike slip component using only GPS horizontal measurements. Fig. 7.8 presents the resolved slip distributions. For the purpose of comparison, we focus only on the dip slip. Only a single slip patch that is north of $45°N$ can be identified from Fig. 7.8, left. The maximum slip is 1.6 cm, which is only about one third of the maximum slip estimated using weighted InSAR data (Fig. 7.7), but the slip area is roughly three times bigger. As a result, we estimate a similar moment magnitude of Mw 6.6.

Fig. 7.9 illustrates how predicted surface distributions compare with observed

displacements. Relatively good agreement between predictions can be found in the horizontal data, but poor matches for the area between $43.5°N$ and $45°N$ and west of $123°W$ in the vertical measurements can be clearly identified. The lack of east-west motion south of $45°N$ explains the absence of dip slip from GPS inversion results (Fig. 7.8), but it contradicts the uplift motion observed near the coast (the region around longitude $124°W$) in both GPS vertical and InSAR measurements. A possible explanation for the discrepancy is that slip occurs in much shallower patches (and closer to the coast) as compared to the slip patch north of 45° and hence results in very small horizontal displacements.

In conclusion, we find that InSAR measurements can resolve slip at depth much better than GPS measurements alone. Instead of $\sim$ 2 cm slip over a large slipping area as many previous GPS data based SSE studies have reported (e.g. *Szeliga et al.* (2008), *Michel et al.* (2018)), InSAR data suggests that slip is distributed in a much narrower zone with a higher slip magnitude.

Finally, we compare slip distributions resolved from weighted InSAR measurements with tremor locations. Fig. 7.10 shows that tremors correlate well spatially with slip distributions. Specifically, north of $45°N$, tremors concentrate between 35km and 45 km depth contours, which is also where most slip concentrates north of latitude $45°N$. South of $45°N$, tremors concentrate between 30 km and 35 km depth contours, which again correlates with slip distribution south of $45°N$. In addition, We find that the density of tremors correlate with the magnitude of slip – the larger slip magnitude, the denser the tremors.

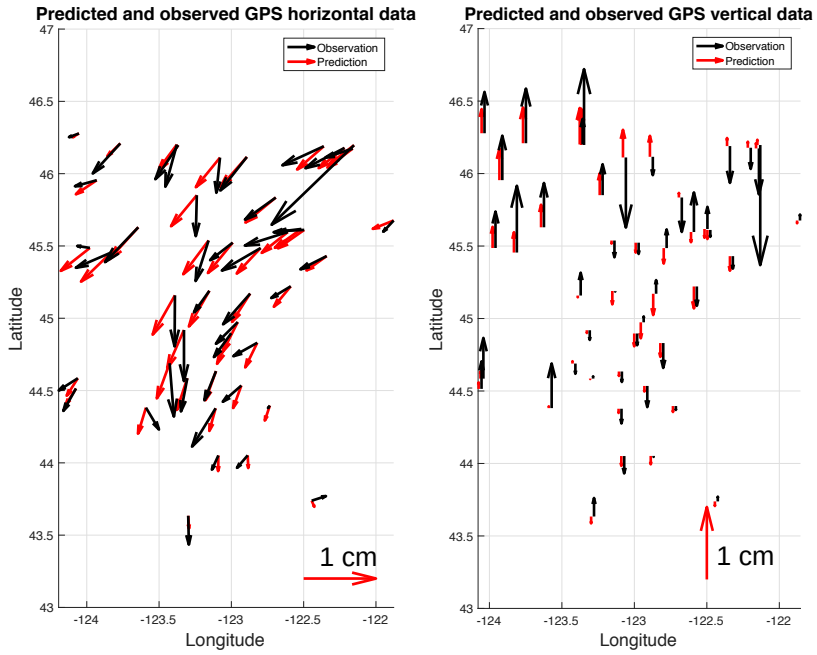

Figure 7.9: Comparisons between predicted GPS measurements with slip distribution in Fig. 7.8 and observed GPS measurements. (Left) Predicted and observed GPS horizontal measurements. (Right) Predicted and observed GPS vertical measurements.

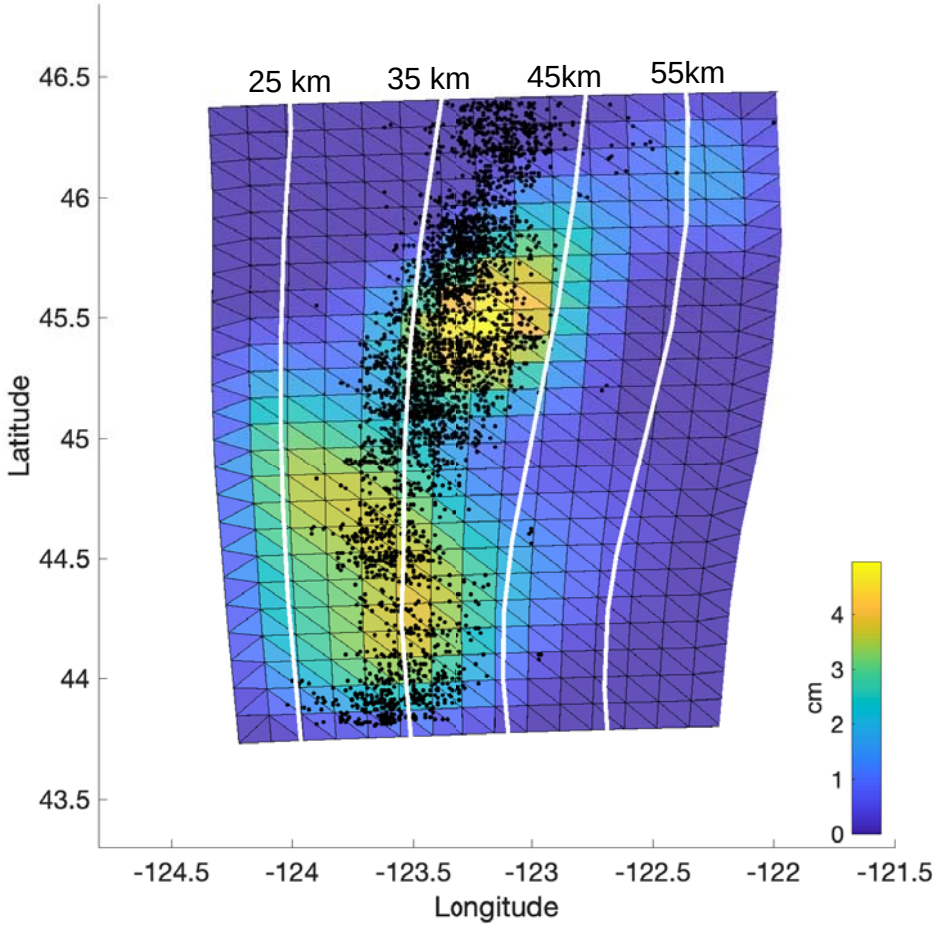

Figure 7.10: Good correlation between tremor locations and slip distributions inferred from weighted InSAR measurements. The white lines are depth contour lines. Tremor locations are plotted as black dots.

Chapter 8

Findings and Conclusions

The ability of Interferometric Synthetic Aperture Radar (InSAR) to observe small signals is often limited by decorrelation noise and atmospheric noise. Modern SAR satellites such as Sentinel-1 provide a large quantity of high-quality data thanks to its dense temporal sampling and superior orbital control. Given the stochastic nature of both atmospheric and decorrelation noise, modern InSAR datasets hence show promise in enabling sufficient noise reduction to observe very small signals.

Slow slip events (SSEs) are an integral part of the subduction zone seismic cycle. Current geodetic methods (e.g., GPS) to observe slow slip events lack the spatial density to resolve slip at depth. However, imaging surface deformation due to slow slip events (SSE) in Cascadia with InSAR is a challenging task due to (1) the small magnitude of the signal and (2) large measurement uncertainties caused by decorrelation and atmospheric noise. In this thesis, we describe how to best make use of modern InSAR datasets to reduce noise and retrieve slow slip event surface deformation. Specifically, we show that by incorporating redundant interferograms in the stack, we can significantly reduce decorrelation noise for rapidly decorrelating areas such as Cascadia. We also show that for a weighted stack, both the weights and the structure

of the atmospheric noise covariance matrix determines the residual atmospheric noise in the stack.

We show that InSAR measurements are most sensitive to up dip slip at depth and that InSAR observed deformation patterns correlate strongly with locations of slow sip zones at depth. Comparing with inversion results using only GPS horizontal data, slip distribution inverted from InSAR measurements show comparable moment magnitude, but with one third the dislocation area and three times as much slip magnitude.

Finally, modern large InSAR datasets also bring challenges in efficient processing. We have shown an algorithm that removes topography-related phase from SAR images and resamples SAR images from radar coordinates to the latitude-longitude grid. Our algorithm moves the need to be familiar with radar processing upstream from the end-user to the data-provider, hence making InSAR processing more friendly. Our algorithm also reduces the need to perform topography correction and geocoding on $N(N-1)/2$ interferograms to N SAR scenes. Given N is easily in the hundreds with modern InSAR datasets, the improvement in data processing efficiency is significant.

Bibliography

Agram, P., and M. Simons (2015), A noise model for insar time series, *Journal of Geophysical Research: Solid Earth*, *120*(4), 2752–2771.

Atwater, B. F. (1987), Evidence for great holocene earthquakes along the outer coast of washington state, *Science*, *236*(4804), 942–944.

Atwater, B. F., and E. Hemphill-Haley (1997), Recurrence intervals for great earthquakes of the past 3,500 years at northeastern willapa bay, washington, *Tech. rep.*, USGPO; Information Services [distributor],.

Bamler, R., and P. Hartl (1998), Synthetic aperture radar interferometry, *Inverse problems*, *14*(4), R1.

Bekaert, D., P. Segall, T. Wright, and A. Hooper (2016), A network inversion filter combining gnss and insar for tectonic slip modeling, *Journal of Geophysical Research: Solid Earth*, *121*(3), 2069–2086.

Bell, J. W., F. Amelung, A. Ferretti, M. Bianchi, and F. Novali (2008), Permanent scatterer insar reveals seasonal and long-term aquifer-system response to groundwater pumping and artificial recharge, *Water Resources Research*, *44*(2).

Berardino, P., G. Fornaro, R. Lanari, and E. Sansosti (2002), A new algorithm for surface deformation monitoring based on small baseline differential sar interferograms, *IEEE transactions on geoscience and remote sensing*, *40*(11), 2375–2383.

Brudzinski, M. R., and R. M. Allen (2007), Segmentation in episodic tremor and slip all along cascadia, *Geology*, *35*(10), 907–910.

Burgette, R. J., R. J. Weldon, and D. A. Schmidt (2009), Interseismic uplift rates for western oregon and along-strike variation in locking on the cascadia subduction zone, *Journal of Geophysical Research: Solid Earth*, *114*(B1).

Bürgmann, R., P. A. Rosen, and E. J. Fielding (2000), Synthetic aperture radar interferometry to measure earths surface topography and its deformation, *Annual review of earth and planetary sciences*, *28*(1), 169–209.

Chapman, J. S., and T. I. Melbourne (2009), Future cascadia megathrust rupture delineated by episodic tremor and slip, *Geophysical Research Letters*, *36*(22).

Chen, and H. A. Zebker (2001), Two-dimensional phase unwrapping with use of statistical models for cost functions in nonlinear optimization, *JOSA A*, *18*(2), 338–351.

Chen, J., H. A. Zebker, P. Segall, and A. Miklius (2014), The 2010 slow slip event and secular motion at kılauea, hawai i, inferred from terrasar-x insar data, *Journal of Geophysical Research: Solid Earth*, *119*(8), 6667–6683.

Clague, J. J. (1997), Evidence for large earthquakes at the cascadia subduction zone, *Reviews of Geophysics*, *35*(4), 439–460.

Cumming, and Bennett (1979), Digital processing of seasat sar data, in *ICASSP'79. IEEE International Conference on Acoustics, Speech, and Signal Processing*, vol. 4, pp. 710–718, IEEE.

Cumming, I. G., and F. H. Wong (2005), Digital processing of synthetic aperture radar data: Algorithms and implementation [with cdrom](artech house remote sensing library), *Artech House, Boston, Massachusetts*.

Curlander, J. C., and R. N. McDonough (1991), Synthetic aperture radar- systems and signal processing(book), *New York: John Wiley & Sons, Inc, 1991.*

Dragert, H., K. Wang, and T. S. James (2001), A silent slip event on the deeper cascadia subduction interface, *Science*, *292*(5521), 1525–1528.

Dragert, H., K. Wang, and G. Rogers (2004), Geodetic and seismic signatures of episodic tremor and slip in the northern cascadia subduction zone, *Earth, planets and space*, *56*(12), 1143–1150.

Emardson, T., M. Simons, and F. Webb (2003), Neutral atmospheric delay in interferometric synthetic aperture radar applications: Statistical description and mitigation, *Journal of Geophysical Research: Solid Earth*, *108*(B5).

Farrell, W. (1972), Deformation of the earth by surface loads, *Reviews of Geophysics*, *10*(3), 761–797.

Ferretti, A., C. Prati, and F. Rocca (2001), Permanent scatterers in sar interferometry, *IEEE Transactions on geoscience and remote sensing*, *39*(1), 8–20.

Flück, P., R. Hyndman, and K. Wang (1997), Three-dimensional dislocation model for great earthquakes of the cascadia subduction zone, *Journal of Geophysical Research: Solid Earth*, *102*(B9), 20,539–20,550.

Fu, Y., D. F. Argus, and F. W. Landerer (2015), Gps as an independent measurement to estimate terrestrial water storage variations in washington and oregon, *Journal of Geophysical Research: Solid Earth*, *120*(1), 552–566.

Galloway, D. L., and J. Hoffmann (2007), The application of satellite differential sar interferometry-derived ground displacements in hydrogeology, *Hydrogeology Journal*, *15*(1), 133–154.

Goldstein (1995), Atmospheric limitations to repeat-track radar interferometry, *Geophysical research letters*, *22*(18), 2517–2520.

Goldstein, R. M., H. A. Zebker, and C. L. Werner (1988), Satellite radar interferometry: Two-dimensional phase unwrapping, *Radio science*, *23*(4), 713–720.

Gomberg, J., C. 2007, and B. W. Group (2010), Slow-slip phenomena in cascadia from 2007 and beyond: A review, *Bulletin*, *122*(7-8), 963–978.

Graham, L. C. (1974), Synthetic interferometer radar for topographic mapping, *Proceedings of the IEEE*, *62*(6), 763–768.

Hanssen, R. F. (2001), *Radar interferometry: data interpretation and error analysis*, vol. 2, Springer Science & Business Media.

Hirose, H., K. Hirahara, F. Kimata, N. Fujii, and S. Miyazaki (1999), A slow thrust slip event following the two 1996 hyuganada earthquakes beneath the bungo channel, southwest japan, *Geophysical Research Letters*, *26*(21), 3237–3240.

Hooper, A., H. Zebker, P. Segall, and B. Kampes (2004), A new method for measuring deformation on volcanoes and other natural terrains using insar persistent scatterers, *Geophysical research letters*, *31*(23).

Hooper, A., P. Segall, and H. Zebker (2007), Persistent scatterer interferometric synthetic aperture radar for crustal deformation analysis, with application to volcán alcedo, galápagos, *Journal of Geophysical Research: Solid Earth*, *112*(B7).

Hooper, A., D. Bekaert, K. Spaans, and M. Arıkan (2012), Recent advances in sar interferometry time series analysis for measuring crustal deformation, *Tectonophysics*, *514*, 1–13.

Hyndman, R., and K. Wang (1995), The rupture zone of cascadia great earthquakes from current deformation and the thermal regime, *Journal of Geophysical Research: Solid Earth*, *100*(B11), 22,133–22,154.

Just, D., and R. Bamler (1994), Phase statistics of interferograms with applications to synthetic aperture radar, *Applied optics*, *33*(20), 4361–4368.

Kato, A., K. Obara, T. Igarashi, H. Tsuruoka, S. Nakagawa, and N. Hirata (2012), Propagation of slow slip leading up to the 2011 mw 9.0 tohoku-oki earthquake, *Science*, *335*(6069), 705–708.

Kostoglodov, V., S. K. Singh, J. A. Santiago, S. I. Franco, K. M. Larson, A. R. Lowry, and R. Bilham (2003), A large silent earthquake in the guerrero seismic gap, mexico, *Geophysical Research Letters*, *30*(15).

Linde, A. T., M. T. Gladwin, M. J. Johnston, R. L. Gwyther, and R. G. Bilham (1996), A slow earthquake sequence on the san andreas fault, *Nature*, *383*(6595), 65.

Lohman, R. B., and M. Simons (2005), Some thoughts on the use of insar data to constrain models of surface deformation: Noise structure and data downsampling, *Geochemistry, Geophysics, Geosystems*, *6*(1).

Lowry, A. R., K. M. Larson, V. Kostoglodov, and R. Bilham (2001), Transient fault slip in guerrero, southern mexico, *Geophysical Research Letters*, *28*(19), 3753–3756.

Maerten, F., P. Resor, D. Pollard, and L. Maerten (2005), Inverting for slip on three-dimensional fault surfaces using angular dislocations, *Bulletin of the Seismological Society of America*, *95*(5), 1654–1665.

Massonnet, D., and K. L. Feigl (1998), Radar interferometry and its application to changes in the earth's surface, *Reviews of geophysics*, *36*(4), 441–500.

McCaffrey, R., A. I. Qamar, R. W. King, R. Wells, G. Khazaradze, C. A. Williams, C. W. Stevens, J. J. Vollick, and P. C. Zwick (2007), Fault locking, block rotation and crustal deformation in the pacific northwest, *Geophysical Journal International*, *169*(3), 1315–1340.

McCrory, P. A., J. L. Blair, F. Waldhauser, and D. H. Oppenheimer (2012), Juan de fuca slab geometry and its relation to wadati-benioff zone seismicity, *Journal of Geophysical Research: Solid Earth*, *117*(B9).

Michel, S., A. Gualandi, and J.-P. Avouac (2018), Interseismic coupling and slow slip events on the cascadia megathrust, *Pure and Applied Geophysics*, pp. 1–25.

Miller, M. M., T. Melbourne, D. J. Johnson, and W. Q. Sumner (2002), Periodic slow earthquakes from the cascadia subduction zone, *Science*, *295*(5564), 2423–2423.

Miyazaki, S., P. Segall, J. J. McGuire, T. Kato, and Y. Hatanaka (2006), Spatial and temporal evolution of stress and slip rate during the 2000 tokai slow earthquake, *Journal of Geophysical Research: Solid Earth*, *111*(B3).

Murray, J., and P. Segall (2005), Spatiotemporal evolution of a transient slip event on the san andreas fault near parkfield, california, *Journal of Geophysical Research: Solid Earth*, *110*(B9).

Onn, F., and H. Zebker (2006), Correction for interferometric synthetic aperture radar

atmospheric phase artifacts using time series of zenith wet delay observations from a gps network, *Journal of Geophysical Research: Solid Earth*, *111*(B9).

Poland, M., A. Miklius, T. Orr, J. Sutton, C. Thornber, and D. Wilson (2008), New episodes of volcanism at kilauea volcano, hawaii, *Eos, Transactions American Geophysical Union*, *89*(5), 37–38.

Rodriguez, E., and J. Martin (1992), Theory and design of interferometric synthetic aperture radars, *IEE Proceedings F (Radar and Signal Processing)*, *139*(2), 147–159.

Rogers, G., and H. Dragert (2003), Episodic tremor and slip on the cascadia subduction zone: The chatter of silent slip, *Science*, *300*(5627), 1942–1943.

Rosen, P. A., S. Hensley, H. A. Zebker, F. H. Webb, and E. J. Fielding (1996), Surface deformation and coherence measurements of kilauea volcano, hawaii, from sir-c radar interferometry, *Journal of Geophysical Research: Planets*, *101*(E10), 23,109–23,125.

Rosen, P. A., S. Hensley, I. R. Joughin, F. Li, S. N. Madsen, E. Rodriguez, and R. M. Goldstein (1998), Synthetic aperture radar interferometry.

Rubinstein, J. L., D. R. Shelly, and W. L. Ellsworth (2009), Non-volcanic tremor: A window into the roots of fault zones, in *New Frontiers in Integrated Solid Earth Sciences*, pp. 287–314, Springer.

Satake, K., K. Shimazaki, Y. Tsuji, and K. Ueda (1996), Time and size of a giant earthquake in cascadia inferred from japanese tsunami records of january 1700, *Nature*, *379*(6562), 246.

Schmidt, D. A., and R. Bürgmann (2003), Time-dependent land uplift and subsidence

in the santa clara valley, california, from a large interferometric synthetic aperture radar data set, *Journal of Geophysical Research: Solid Earth*, *108*(B9).

Schmitt, M., and U. Stilla (2014), Maximum-likelihood-based approach for single-pass synthetic aperture radar tomography over urban areas, *IET Radar, Sonar & Navigation*, *8*(9), 1145–1153.

Segall, P. (2010), *Earthquake and volcano deformation*, Princeton University Press.

Segall, P., and A. M. Bradley (2012), Slow-slip evolves into megathrust earthquakes in 2d numerical simulations, *Geophysical Research Letters*, *39*(18).

Segall, P., and M. Matthews (1997), Time dependent inversion of geodetic data, *Journal of Geophysical Research: Solid Earth*, *102*(B10), 22,391–22,409.

Simons, M., and P. Rosen (2007), Interferometric synthetic aperture radar geodesy.

Szeliga, W., T. Melbourne, M. Santillan, and M. Miller (2008), Gps constraints on 34 slow slip events within the cascadia subduction zone, 1997–2005, *Journal of Geophysical Research: Solid Earth*, *113*(B4).

Treuhaft, R., and G. Lanyi (1987), The effect of the dynamic wet troposphere on radio interferometric measurements, *Radio Science*, *22*(02), 251–265.

Wech, A. G., and N. M. Bartlow (2014), Slip rate and tremor genesis in cascadia, *Geophysical Research Letters*, *41*(2), 392–398.

Wright, T., B. Parsons, and E. Fielding (2001), Measurement of interseismic strain accumulation across the north anatolian fault by satellite radar interferometry, *Geophysical Research Letters*, *28*(10), 2117–2120.

Zebker, H. A., and R. M. Goldstein (1986), Topographic mapping from interferometric synthetic aperture radar observations, *Journal of Geophysical Research: Solid Earth*, *91*(B5), 4993–4999.

Zebker, H. A., and J. Villasenor (1992), Decorrelation in interferometric radar echoes, *IEEE Transactions on geoscience and remote sensing*, *30*(5), 950–959.

Zebker, H. A., P. A. Rosen, R. M. Goldstein, A. Gabriel, and C. L. Werner (1994), On the derivation of coseismic displacement fields using differential radar interferometry: The landers earthquake, *Journal of Geophysical Research: Solid Earth*, *99*(B10), 19,617–19,634.

Zebker, H. A., P. A. Rosen, and S. Hensley (1997), Atmospheric effects in interferometric synthetic aperture radar surface deformation and topographic maps, *Journal of geophysical research: solid earth*, *102*(B4), 7547–7563.

Zebker, H. A., S. Hensley, P. Shanker, and C. Wortham (2010), Geodetically accurate insar data processor, *IEEE Transactions on Geoscience and Remote Sensing*, *48*(12), 4309–4321.

Zheng, Y., and H. A. Zebker (2017), Phase correction of single-look complex radar images for user-friendly efficient interferogram formation, *IEEE Journal of Selected Topics in Applied Earth Observations and Remote Sensing*, *10*(6), 2694–2701.